Stability-enhanced AP IMEX-LDG schemes for linear kinetic transport equations under a diffusive scaling

Zhichao Peng* Yingda Cheng† Jing-Mei Qiu‡ Fengyan Li§

April 29, 2020

Abstract

Transport equations arise in many applications such as rarefied gas dynamics, neutron transport, and radiative transfer. In this work, we consider some linear kinetic transport equations in a diffusive scaling and design high order asymptotic preserving (AP) methods within the discontinuous Galerkin method framework, with the main objective to achieve unconditional stability in the diffusive regime when the Knudsen number $\varepsilon \ll 1$, and to achieve high order accuracy when $\varepsilon = O(1)$ and when $\varepsilon \ll 1$. Initial layers are also taken into account. The ingredients to accomplish our goal include: model reformulations based on the micro-macro decomposition and the limiting diffusive equation, local discontinuous Galerkin (LDG) methods in space, globally stiffly accurate implicit-explicit (IMEX) Runge-Kutta methods in time, and strategies to handle non-well prepared initial data. Formal asymptotic analysis is carried out for the continuous model within the micro-macro decomposed framework to derive the initial layer as well as the interior problem with an asymptotically consistent initial condition as $\varepsilon \to 0$, and it is also conducted for numerical schemes to show the AP property and to understand the numerical initial treatments in the presence of initial layers. Fourier type stability analysis is performed, and it confirms the unconditional stability in the diffusive regime, and moreover it gives the stability condition in the kinetic regime when $\varepsilon = O(1)$. In the reformulation step, a weighted diffusive term is added and subtracted to remove the parabolic stiffness and enhance the numerical stability in the diffusive regime. Such idea is not new, yet our numerical stability and asymptotic analysis provide new mathematical understanding towards the desired properties of the weight function. Finally, numerical examples are presented to demonstrate the accuracy, stability, and asymptotic preserving property of the proposed methods, as well as the effectiveness of the proposed strategies in the presence of the initial layer.

1 Introduction

We consider a linear kinetic transport equation in a diffusive scaling,

$$\mathcal{P}^{\varepsilon}: \qquad \varepsilon f_t + v \partial_x f = \frac{1}{\varepsilon} \left(\langle f \rangle - f \right)$$
 (1.1)

with the initial condition and suitable boundary conditions. The function f = f(x, v, t) is the probability phase space density function of the particles, with $x \in \Omega_x \subset \mathbb{R}$, $v \in \Omega_v \subset \mathbb{R}$, and $t \geq 0$ being the spatial, velocity, and temporal variables, respectively. The operator $\mathcal{L}(f) = 0$

^{*}Department of Mathematical Sciences, Rensselaer Polytechnic Institute, Troy, NY 12180, U.S.A. pengz2@rpi.edu

†Department of Mathematics, Department of Computational Mathematics, Science and Engineering, Michigan
State University, East Lansing, MI 48824 U.S.A. ycheng@msu.edu. Research is supported by NSF grants DMS1453661, DMS-1720023, and the Simons Foundation under award number 558704.

[‡]Department of Mathematical Sciences, University of Delaware, Newark, DE 19716, U.S.A. jingqiu@udel.edu. Research is supported by NSF grants DMS-1522777, DMS-1818924, and AFOSR grant FA9550-18-1-0257.

[§]Department of Mathematical Sciences, Rensselaer Polytechnic Institute, Troy, NY 12180, U.S.A. lif@rpi.edu. Research is supported by NSF grants DMS-1719942, DMS-1913072.

 $\langle f \rangle - f$ defines a normalized scattering operator, where $\langle f \rangle := \int_{\Omega_v} f d\nu$ and ν is a measure of the velocity space. The parameter $\varepsilon > 0$ is the dimensionless Knudsen number that is the ratio of the mean free path of the particles over the characteristic length of the system. With the presence of ε in front of the time derivative of f, we focus on the long time behavior of the system under a diffusive scaling. As $\varepsilon \to 0$, the solution to this singular perturbation problem \mathcal{P}^ε converges to that of a macroscopic linear diffusive model \mathcal{P}^0 in (2.4) (at least away from the initial and boundary of the space-time domain). When $\varepsilon = O(1)$, the system balances the transport and the scattering processes. The linear kinetic transport equation (1.1) provides a prototype model for more realistic models in studying rarefied gas dynamics, neutron transport, radiative transfer, among many others.

In this work, we are concerned with the design and the mathematical understanding of high order numerical methods for (1.1), particularly under the discontinuous Galerkin (DG) framework and with the asymptotic preserving (AP) property. Numerical methods with the AP property are designed for the multi-scale model $\mathcal{P}^{\varepsilon}$, and they are consistent and stable for a wide range of values of ε . As $\varepsilon \to 0$, the limiting schemes are consistent discretizations of the limiting equation \mathcal{P}^0 when the discretization parameters (such as mesh and time step sizes) are fixed and under-resolved. AP methods have gone through active development in past few decades for various problems, see e.g. the review papers [16] for kinetic and hyperbolic equations and [11] for fluid models. Unlike domain decomposition methods for multi-scale problems, AP methods provide a natural transition between models at different scales when ε varies in space and/or in time.

DG methods are finite element methods that use discontinuous functions as approximations. They are chosen here as spatial discretizations due to their many attractive properties, such as the ease to be designed with arbitrary accuracy, flexibility in adaptive implementation, compactness and high parallel efficiency, and more importantly, the methods suit for many different types of differential equations, hence are a natural candidate for the design of AP schemes that can simultaneously capture the solutions in various regimes. DG methods have a long history for simulating transport problems. Indeed the first upwind DG method by Reed and Hill in 1973 [28] was for the linear stationary neutron transport equation. For the stationary radiative transfer equation in diffusive regimes, it was shown in one dimension [20] that the P^0 upwind DG method is not AP yet the P^1 upwind DG method is. The AP property was also examined in [21] for the P^1 upwind DG method in the presence of the boundary layer. This property was further investigated numerically [1] and analyzed [12] in high dimensions and/or for more general discrete spaces. And the understanding to the issue also led to the development of a new AP-DG method in [18] that uses the reduced upwind stabilization in the numerical flux.

The methods reviewed above involve DG discretizations based on the original form of the kinetic models. The resulting algebraic systems can be solved by (accelerated) source iterations with transport sweep techniques [2, 18]. We here will propose numerical methods that are based on a reformulated form of the underlying model. Particularly, our methods are based on the micro-macro reformulation (see (2.2), also [26]) of the model problem (1.1), and the implicit part to solve in our proposed methods is essentially a discrete Poisson equation. Within the micro-macro framework, in [23, 25] a first order finite difference AP method was formulated and analyzed for stability. Later a family of high order AP methods, based on DG spatial discretization and globally stiffly accurate implicit-explicit (IMEX) Runge Kutta (RK) temporal discretizations of type ARS (after Asher, Ruuth, and Spiteri [3, 5]), was proposed in [14] and analyzed in [15]. As $\varepsilon \to 0$, the limiting schemes of the methods in [14] are intrinsically explicit discretizations for the limiting heat equation. Therefore for the schemes with $\varepsilon \ll 1$ in the diffusive regime, numerical stability requires the time step to satisfy $\Delta t = O(h^2)$, where h denotes the characteristic spatial mesh size. Such parabolic time step condition is quite stringent for the computational efficiency. Similar issue also occurs to other AP schemes, including the finite difference methods based on the even-odd parity formulation [17, 19] or based on the micro-macro decomposition in [23, 25]. The primary objective of this work is to design new AP methods, improved from the methods in [14], that are unconditionally stable when the underlying problem is in its diffusive regime, and additionally we want to establish mathematical understanding of the proposed methods especially in the presence of the initial layers. One will see that our analysis also contributes to the understanding of some previous developments in the literature.

To enhance the stability, similar to [5, 4], we add and subtract a weighted diffusion term to further reformulate the micro-macro decomposed equation, aiming to remove the parabolic stiffness. The added term is chosen according to the limiting equation and involves a weight function ω . For this newly reformulated system, we design local DG (LDG) methods [10] in space, and globally stiffly accurate IMEX-RK method of type ARS in time [3, 5], equipped with a *suitably chosen* implicit-explicit strategy.

Numerically the proposed methods (with a properly chosen weight function ω) are observed to be unconditionally stable in the diffusive regime when ε/h is relatively small. Fourier type numerical stability further confirms this when it is applied to a discrete velocity model. Our stability analysis also reveals a scaling structure of the model, and this provides useful guidance to the choice of the weight function ω in terms of the model and discretization parameters $\varepsilon, h, \Delta t$. Using weight functions preserving this scaling structure in return will result in some invariant property of the numerical stability condition (see the existence of the function $\mathcal{F}_{p,\omega}$ in the stability condition in Section 4). Based on our analysis, the weight functions $\omega = \exp(-\varepsilon/h)$ and $\omega = \exp(-\varepsilon/h)$ will preserve the scaling structure of the model, while the choice $\omega = \exp(-\varepsilon^2/h)$ used in [5] will not. What we also look into is the stability property of the methods when they are applied to the kinetic regime with $\varepsilon = O(1)$ where the transport effect dominates.

Another important aspect is to examine the proposed methods being AP, with the limiting schemes as $\varepsilon \to 0$ not only being consistent to the limiting equations but also being high order accurate. This is investigated with the initial layers being taken into account. We first carry out formal asymptotic analysis for the continuous problem within the micro-macro framework when $\varepsilon \ll 1$ with the possible presence of the initial layer and when the boundary condition is periodic in x. On the numerical level, strategies are proposed to avoid order reduction or inaccuracy when the initial data is not well-prepared. For the resulting methods, formal asymptotic analysis is carried out to confirm the AP property of the proposed schemes, regardless the initial data being well-prepared or not. Moreover, the limiting schemes are of formally high order accuracy. The asymptotic analysis identifies more property of the weight function ω , see (5.13), to ensure the AP property of the methods.

The remaining of this paper is organized as follows. In Section 2, we reformulate the model equation, and carry out a formal asymptotic analysis with respect to the parameter $\varepsilon \ll 1$ and when the initial data may or may not be well-prepared. In Section 3, we present the proposed numerical methods, by first discretizing the problem in time then in space. Modification is proposed to the numerical methods during the first one or two time steps to address the accuracy reduction or loss in the presence of the initial layer. In Section 4, numerical stability is examined through Fourier analysis in both the diffusive and kinetic regimes. It also provides some guidance on choosing the weight function ω in the schemes. Formal asymptotic analysis is then performed for the proposed methods in Section 5, and it shows the methods are AP, with the limiting schemes as $\varepsilon \to 0$ being formally high order accurate. The performance of the proposed methods is demonstrated numerically in Section 6, which is followed by concluding remarks in Section 7.

2 Model equation

In this section, we will reformulate the model equation (1.1) and carry out a formal asymptotic analysis with respect to the parameter ε when it is small, i.e. $\varepsilon \ll 1$. It is assumed that the boundary condition is periodic in x. The readers can have two specific examples of (1.1) in mind. One is the one-group transport equation in slab geometry. Here $\Omega_v = [-1, 1]$ and

$$\langle f \rangle = \int_{\Omega_{v}} f d\nu = \frac{1}{2} \int_{\Omega_{v}} f(x, v, t) dv,$$

with dv as the standard Lebesgue measure. The other is the telegraph equation, involving two discrete velocities with $\Omega_v = \{-1, 1\}$, and

$$\langle f \rangle = \int_{\Omega_v} f d\nu = \frac{1}{2} \left(f(x, v = 1, t) + f(x, v = -1, t) \right).$$

In both cases, the scattering operator $\mathcal{L}(f) = \langle f \rangle - f$ in (1.1) only acts on the v variable and has one dimensional null space $\text{Null}(\mathcal{L}) = \{f : f = \langle f \rangle\} = \text{Span}\{1\}$.

2.1 Reformulation

Our proposed numerical methods are based on a reformulated form of the model equation (1.1), obtained in two steps.

As the first step, we reformulate (1.1) into its micro-macro decomposition, originated in [26] for PDE analysis and later used in [23, 15, 14] for numerical method design. Consider the square-integrable space $L^2(\Omega_v)$ in v, with an inner product $\langle f, g \rangle := \langle fg \rangle$. Let Π be the L^2 projection operator onto Null(\mathcal{L}), and let $\rho := \Pi f = \langle f \rangle$. Then f can be decomposed orthogonally into

$$f = \langle f \rangle + \varepsilon g = \rho + \varepsilon g, \tag{2.1}$$

where $\langle g \rangle = 0$. We now apply Π and its orthogonal complement $\mathbf{I} - \Pi$ to (1.1), and this leads to the micro-macro reformulation

$$\partial_t \rho + \partial_x \langle vg \rangle = 0, \tag{2.2a}$$

$$\partial_t g + \frac{1}{\varepsilon} (\mathbf{I} - \Pi)(v \partial_x g) + \frac{1}{\varepsilon^2} v \partial_x \rho = -\frac{1}{\varepsilon^2} g.$$
 (2.2b)

The operator **I** is the identity operator. As it will be shown in next subsection, as $\varepsilon \to 0$, the system (2.2) (at least away from the initial layer) becomes

$$\partial_t \rho + \partial_x \langle vg \rangle = 0, \tag{2.3a}$$

$$g = -v\partial_x \rho, \tag{2.3b}$$

which implies that the macroscopic part ρ satisfies a diffusive (indeed a heat) equation,

$$\partial_t \rho = \langle v^2 \rangle \partial_{xx} \rho \tag{2.4}$$

with an asymptotically consistent initial condition $\rho(x,0) = \lim_{\varepsilon \to 0} \langle f(x,\cdot,0) \rangle$. (The initial data of f for the model equation (1.1) may depend on ε .) The relation (2.3b) will be referred to as the local equilibrium, and it indicates g can be expressed in terms of ρ in the limiting model. Note that $\langle v^2 \rangle = 1$ for the telegraph equation and $\langle v^2 \rangle = 1/3$ for the one-group transport equation in slab geometry.

As the second step, we add a weighted diffusion term $\omega \langle v^2 \rangle \partial_{xx} \rho$ to the both sides of (2.2a), and get

$$\partial_t \rho + \partial_x \langle v(g + \omega v \partial_x \rho) \rangle = \omega \langle v^2 \rangle \partial_{xx} \rho,$$
 (2.5a)

$$\partial_t g + \frac{1}{\varepsilon} (\mathbf{I} - \Pi)(v \partial_x g) + \frac{1}{\varepsilon^2} v \partial_x \rho = -\frac{1}{\varepsilon^2} g.$$
 (2.5b)

The term $\langle v^2 \rangle \partial_{xx} \rho$ is closely related to the limiting equation (2.4), and a similar idea was used in [5]. The non-negative weight function ω depends on ε and it is bounded and independent of x, satisfying

$$\omega \to 1 \quad \text{as} \quad \varepsilon \to 0.$$
 (2.6)

Other properties desired for the weight function ω will be identified as we analyze the proposed numerical methods.

2.2 Formal asymptotic analysis with initial layers: the continuous problem

In this section, we will carry out a formal asymptotic analysis for the micro-macro reformulation (2.2) (hence (2.5)), assuming the smallness of the parameter ε . Particularly, we will consider the case with initial layers when the initial data is not well-prepared. One can refer to [27] for an analysis based on the original form of a kinetic transport equation. Note that the analysis here does not essentially depend on the dimension of the spatial space Ω_x and the velocity space

 Ω_v . Within this section, functions will be written with their explicit dependence on ε , such as $u(x,v,t;\varepsilon)$. Here and below, when the big-O notation $z=O(\Upsilon^n)$ is used, it means that there exists a constant C>0, $\Upsilon_0>0$, such that $|z|\leq C\Upsilon^n, \forall \Upsilon<\Upsilon_0$. Here Υ can be ε , h, or Δt , while C is independent of ε , h and Δt . Under the assumption that the boundary condition is periodic in x, boundary effects including boundary layers are not considered. The initial data $f(x,v,0;\varepsilon)=\rho(x,0;\varepsilon)+\varepsilon g(x,v,0;\varepsilon)$ is taken as

$$f(x, v, 0; \varepsilon) = \Lambda(x, v) + \varepsilon \Theta(x, v) + O(\varepsilon^{2}), \tag{2.7}$$

where Λ and Θ are integrable in v. This implies

$$\rho(x,0;\varepsilon) = \langle \Lambda \rangle + \varepsilon \langle \Theta \rangle + O(\varepsilon^2), \quad g(x,v,0;\varepsilon) = \frac{\Lambda - \langle \Lambda \rangle}{\varepsilon} + \Theta - \langle \Theta \rangle + O(\varepsilon). \tag{2.8}$$

The solution to (2.2) has the following decompositions

$$\rho = \rho^I + \rho^i, \quad g = g^I + g^i. \tag{2.9}$$

Here $\rho^I(x,t;\varepsilon)$ and $g^I(x,v,t;\varepsilon)$ correspond to the *interior* solution that is the entire solution away from the initial layer; while $\rho^i(x,t;\varepsilon)$, $g^i(x,v,t;\varepsilon)$ are from the *initial layer* solution, and they decay to zero when exiting from the initial layer. Next we will derive the leading terms in ρ and g for the interior problem and the initial layer up to O(1), and then summarize our main observations.

Interior problem: for the interior problem, we take the ansatz

$$\rho^{I} = \rho_0^{I}(x,t) + O(\varepsilon), \quad g^{I} = g_0^{I}(x,v,t) + O(\varepsilon), \tag{2.10}$$

and plug them into (2.2). (One can start with an $O(\varepsilon^{-1})$ term in g^I , and this term turns out to be zero.) After collecting the O(1) leading terms, we get

$$\partial_t \rho_0^I + \partial_x \langle v g_0^I \rangle = 0, \tag{2.11a}$$

$$g_0^I + v\partial_x \rho_0^I = 0, \tag{2.11b}$$

and this implies that the leading term ρ_0^I of the interior solution satisfies the heat equation

$$\partial_t \rho_0^I = \langle v^2 \rangle \partial_{xx} \rho_0^I. \tag{2.12}$$

And g_0^I itself is not an independent quantity, and it is determined by ρ_0^I via (2.11b).

Initial layer: for the initial layer problem, one can show the layer width is of $O(\varepsilon^2)$ following a standard dominant balance argument [13]. Let $\tau = t/\varepsilon^2$ be the scaled (or called stretched) time variable. The initial layer solution, still represented by $\rho^i(x, \tau; \varepsilon)$ and $g^i(x, v, \tau; \varepsilon)$, satisfies

$$\partial_{\tau}\rho^{i} + \varepsilon^{2}\partial_{x}\langle vg^{i}\rangle = 0, \tag{2.13a}$$

$$\partial_{\tau}g^{i} + \varepsilon(\mathbf{I} - \Pi)(v\partial_{x}g^{i}) + v\partial_{x}\rho^{i} = -g^{i}. \tag{2.13b}$$

We take the ansatz

$$\rho^i = \rho^i_0(x,\tau) + O(\varepsilon), \quad g^i = g^i_{-1}(x,v,\tau)\varepsilon^{-1} + g^i_0(x,v,\tau) + O(\varepsilon), \tag{2.14}$$

and collect $O(\varepsilon^{-1})$ and O(1) terms, respectively, and get

$$O(\varepsilon^{-1}): \quad \partial_{\tau} q_{-1}^{i} + q_{-1}^{i} = 0,$$
 (2.15a)

$$O(1): \qquad \partial_{\tau} \rho_0^i = 0, \tag{2.15b}$$

$$\partial_{\tau} g_0^i + (\mathbf{I} - \Pi)(v \partial_x g_{-1}^i) + v \partial_x \rho_0^i + g_0^i = 0. \tag{2.15c}$$

Now by matching the leading terms of ρ and q with the given initial data (2.8), we have

$$O(1): \qquad \rho_0^I(x,0) + \rho_0^i(x,0) = \langle \Lambda \rangle, \quad g_{-1}^i(x,v,0) = \Lambda - \langle \Lambda \rangle, \tag{2.16a}$$

$$O(\varepsilon): g_0^I(x, v, 0) + g_0^i(x, v, 0) = \Theta - \langle \Theta \rangle.$$
 (2.16b)

Based on (2.15b) and $\rho_0^i(x,\infty)=0$, we get

$$\rho_0^i(x,\tau) = 0, \ \forall \tau > 0.$$
 (2.17)

This, together with (2.16a), gives the asymptotically consistent initial condition for the interior heat equation (2.12):

$$\rho_0^I(x,0) = \langle \Lambda \rangle. \tag{2.18}$$

Moreover, from (2.16b), (2.11b) and (2.18), we get the initial data for g_0^i in the initial layer solution,

$$g_0^i(x, v, 0) = \Theta - \langle \Theta \rangle + v \partial_x \rho_0^I(x, 0) = \Theta - \langle \Theta \rangle + v \partial_x \langle \Lambda \rangle. \tag{2.19}$$

We next solve for g_{-1}^i from (2.15a) and (2.16a),

$$g_{-1}^{i}(x, v, \tau) = g_{-1}^{i}(x, v, 0) e^{-\tau} = (\Lambda - \langle \Lambda \rangle) e^{-\tau}.$$
 (2.20)

Finally we can solve for g_0^i based on (2.15c), (2.17), (2.19), (2.20):

$$g_0^i(x, v, \tau) = \left(g_0^i(x, v, 0) - \tau(\mathbf{I} - \Pi)\{v\partial_x(\Lambda - \langle \Lambda \rangle)\}\right)e^{-\tau}$$
$$= \left(\Theta - \langle \Theta \rangle + v\partial_x\langle \Lambda \rangle - \tau(\mathbf{I} - \Pi)\{v\partial_x(\Lambda - \langle \Lambda \rangle)\}\right)e^{-\tau}. \tag{2.21}$$

Summary and observations: In summary, when $\varepsilon \ll 1$, the solution to the micro-macro reformulated system (2.2) with the initial condition (2.7) has the following form

$$\begin{split} &\rho(x,t;\varepsilon) = \rho_0^I(x,t) + O(\varepsilon), \\ &g(x,v,t;\varepsilon) = g_0^I(x,v,t) + \frac{1}{\varepsilon}g_{-1}^i(x,v,t/\varepsilon^2) + g_0^i(x,v,t/\varepsilon^2) + O(\varepsilon). \end{split}$$

One can make the following observations:

- For the leading term (ρ_0^I, g_0^I) in the interior solution, ρ_0^I satisfies the heat equation (2.12) with the initial condition (2.18), and g_0^I is determined by ρ_0^I via (2.11b);
- The leading term (up to O(1)) in ρ does not contain an initial layer;
- When $\frac{1}{\varepsilon}g_{-1}^i + g_0^i = 0$, with g_{-1}^i, g_0^i given in (2.20)-(2.21), the leading term (up to O(1)) has no initial layer; otherwise the initial layer of $O(\varepsilon^2)$ -width is present.
- Based on the explicit formula in (2.20)-(2.21), the leading term of g is free of the initial layer if and only if

$$\frac{\Lambda - \langle \Lambda \rangle}{\varepsilon} + \Theta - \langle \Theta \rangle + v \partial_x \langle \Lambda \rangle - \tau (\mathbf{I} - \Pi) \{ v \partial_x (\Lambda - \langle \Lambda \rangle) \} = 0.$$
 (2.22)

That is,

$$\Lambda = \langle \Lambda \rangle, \quad \Theta - \langle \Theta \rangle + v \partial_x \langle \Lambda \rangle = 0.$$

This, under the assumption (2.7) and (2.8) on the initial data, is equivalent to

$$g(x, v, 0; \varepsilon) + v\partial_x \rho(x, 0; \varepsilon) = O(\varepsilon).$$
 (2.23)

Note that (2.23) indicates the initial data is within the $O(\varepsilon)$ -width neighborhood of the local equilibrium (2.11b) (see also (2.3b)). In this case, we say the initial data is well-prepared. The analysis above shows that the initial data being well-prepared or not determines the presence of the initial layer in the leading term of the solution.

Definition 2.1. The initial data $f(x, v, 0; \varepsilon) = \rho(x, 0; \varepsilon) + \varepsilon g(x, v, 0; \varepsilon)$ is said to be well-prepared if it satisfies the relation (2.23).

3 Numerical methods

In this section, we will present the proposed numerical methods. We will start with the temporal discretization, then discretize in space. The boundary condition in space is assumed to be periodic. Some more general boundary conditions will be considered in Section 6.2.

3.1 Temporal discretization

In time, we will apply IMEX-RK methods. We will begin with the first order method and explain our proposed implicit-explicit strategy, then discuss initial layer treatments to avoid accuracy loss or reduction, and finally we will present high order IMEX-RK methods.

First order temporal discretization. When the temporal accuracy is of first order, our scheme, denoted as *IMEX1*, is defined as follows. Given the numerical solution ρ^n , g^n at $t = t^n$, we look for ρ^{n+1} , g^{n+1} at $t^{n+1} = t^n + \Delta t$, satisfying

$$\frac{\rho^{n+1} - \rho^n}{\Delta t} + \partial_x \langle v(g^n + \omega v \partial_x \rho^n) \rangle = \omega \langle v^2 \rangle \partial_{xx} \rho^{n+1}, \tag{3.1a}$$

$$\frac{g^{n+1} - g^n}{\Delta t} + \frac{1}{\varepsilon} (\mathbf{I} - \Pi)(v\partial_x g^n) + \frac{1}{\varepsilon^2} v\partial_x \rho^{n+1} = -\frac{1}{\varepsilon^2} g^{n+1}. \tag{3.1b}$$

The implicit-explicit strategy we adopt here (and later for high order temporal discretizations) is to treat all the terms that are dominating when $\varepsilon \ll 1$ implicitly. This includes the most stiff terms on the scale $\frac{1}{\varepsilon^2}$ in (3.1b), and the diffusion term on the right side of (3.1a). Note that in the diffusive regime with $\varepsilon \ll 1$, the solution (at least away from the initial layer) is expected to stay close to the local equilibrium $g + v\partial_x \rho = 0$. Hence based on the property (2.6) of the weight function ω , namely, $\omega \to 1$ as $\varepsilon \to 0$, the term

$$\partial_x \langle v(g + wv\partial_x \rho) \rangle = \partial_x \langle v(g + v\partial_x \rho) \rangle + (\omega - 1) \langle v^2 \rangle \partial_{xx} \rho$$

is less dominating, and it is treated explicitly together with the transport term $(\mathbf{I} - \Pi)(v\partial_x q)$.

Treatment for initial layers. When the initial data is not well-prepared, the solution will contain an initial layer of $O(\varepsilon^2)$ -width in its leading term. In this case g can be of $O(\varepsilon^{-1})$ initially, yet after the first time step at $t = \Delta t \gg \varepsilon^2$, the solution exits from the initial layer, and both ρ and g should be of O(1). This feature, however, is not well respected at the discrete level by our implicit-explicit strategy above, mainly due to the explicit treatment of g in (3.1a). In fact in this case, the numerical scheme (3.1) may produce ρ^1, g^1 of size $O(\varepsilon^{-1})$ following (3.1a), hence becomes very inaccurate. To overcome this, one would want to treat the g term (hence the $g + \omega v \partial_x \rho$ term) in (3.1a) implicitly. With the consideration for an easy analysis, we propose to replace the scheme (3.1) at n = 0 by

$$\frac{\rho^1 - \rho^0}{\Delta t} + \partial_x \langle vg^1 \rangle = 0. \tag{3.2a}$$

$$\frac{g^1 - g^0}{\Delta t} + \frac{1}{\varepsilon} (\mathbf{I} - \Pi)(v\partial_x g^0) + \frac{1}{\varepsilon^2} v\partial_x \rho^0 = -\frac{1}{\varepsilon^2} g^1.$$
 (3.2b)

The resulting scheme with the modification, namely (3.1) for $n \geq 1$ and (3.2) for n = 0, is still referred to as the IMEX1 scheme. Using this slightly modified scheme, one will get $\rho^1, g^1 = O(1)$ even with $g^0 = O(\varepsilon^{-1})$. This will be explained more systematically in Section 5.1. Alternatively, we can address the accuracy issue around the non well-prepared initial data by replacing the scheme at n = 0 by (3.2a) coupled with (3.1b). In [7], an initial fixing strategy based on Richardson extrapolation was used to guarantee the designed second order accuracy in the presence of an initial layer.

Remark 3.1. The first order temporal discretization (3.2) was previously used in [23] for the same kinetic equation to define a first order finite difference AP scheme regardless of the initial data, and this scheme also has the parabolic time step restriction $\Delta t = O(h^2)$ as $\varepsilon \to 0$ just like our method in [14, 15]. Here, we use the discretization (3.2) only for the first time step to deal with the initial layer, and more specifically, to drive the numerical solution to be O(1) after the first step. Note that away from the initial layer, our implicit-explicit strategy in (3.1) drives the numerical solution to stay close to the local equilibrium, with $g^n + v\partial_x \rho^n = O(\varepsilon)$, $n \ge 2$, while a scheme with (3.2) for all $n \ge 0$ drives the solution to satisfy $g^{n+1} + v\partial_x \rho^n = O(\varepsilon)$, that is $g^n + v\partial_x \rho^n = O(\varepsilon) + O(\Delta t)$ with an extra $O(\Delta t)$ error. This shows that our implicit-explicit strategy (3.1) better keeps the computed solution close to the local equilibrium when $\varepsilon \ll 1$.

Higher order temporal discretization. To improve the temporal accuracy, higher order globally stiffly accurate IMEX-RK time integrators of type ARS will be applied. An r-stage IMEX-RK scheme we consider here can be represented with a double Butcher tableau

$$\begin{array}{c|cccc}
\tilde{c} & \tilde{\mathcal{A}} & c & \mathcal{A} \\
\hline
& \tilde{b}^T & b^T & \end{array},$$
(3.3)

where both $\tilde{A} = (\tilde{a}_{ij})$ and $A = (a_{ij})$ are lower triangular $r \times r$ matrices, with \tilde{A} having zero diagonal entries. For convenience, the index is taken as $i, j = 0, 1, \dots, s$, with s = r - 1. The components of $\tilde{c} = (\tilde{c}_i)$ and $c = (c_i)$ are related to \tilde{A} and A in the usual way, namely, $\tilde{c}_i = \sum_{j=0}^{i-1} \tilde{a}_{ij}, c_i = \sum_{j=0}^{i} a_{ij}, i = 0, \dots, s$ and vectors $\tilde{b} = (\tilde{b}_i)$ and $b = (b_i)$ provide the quadrature weights to combine the numerical approximations from inner stages. The IMEX-RK scheme is said to be *globally stiffly accurate* [5] if

$$c_s = \tilde{c}_s = 1$$
, and $a_{sj} = b_j, \tilde{a}_{sj} = \tilde{b}_j, \forall j = 0, \dots, s.$ (3.4)

Its being type ARS [5] refers to the following structure of the implicit part

$$\mathcal{A} = \begin{bmatrix} 0 & 0 \\ 0 & \hat{\mathcal{A}} \end{bmatrix}, \tag{3.5}$$

where \hat{A} is invertible. We want to particularly point out that the r-stage IMEX-RK method of type ARS effectively has s = r - 1 stages.

The first order time integrator in our scheme (3.1) is globally stiffly accurate and of type ARS. It is denoted as ARS(1,1,1) and represented by

$$\begin{array}{c|ccccc} 0 & 0 & 0 & & 0 & 0 & 0 \\ \hline 1 & 1 & 0 & & & 1 & 0 & 1 \\ \hline & 1 & 0 & & & & 0 & 1 \end{array} \; .$$

For second and third order accuracy, we use ARS(2,2,2) and ARS(4,4,3) proposed in [3] (also see the appendix in [5] for the formulas). Here ARS(s,s,p) stands for an IMEX-RK method of type ARS, that is p-th order accurate with effective s stages in both the explicit and implicit parts. In this work, the semi-discrete temporal schemes with ARS(1,1,1), ARS(2,2,2) and ARS(4,4,3) are referred to as the IMEXp scheme, with p=1,2,3, respectively.

When the initial data is not well-prepared, the IMEXp scheme may suffer from order reduction or poor accuracy. Based on the formal asymptotic analysis in Section 5 (also see Remark 3.3 and Remark 5.2), the following strategy is proposed. At n=0, we replace the IMEXp scheme by the first order scheme in (3.2). In addition, for the first two steps with n=0,1, we modify the time step size into $\Delta t_1 = \Delta t_2 = \Delta t^p$, where Δt is the time step used for later steps and predicted by stability analysis. Here and below, whenever needed, we will use Δt_n to represent the time step size from the n-th time step.

Remark 3.2. It is important for us to use globally stiffly accurate IMEX-RK methods in order for the proposed methods to be AP (also see discussion in [5]). Moreover, with our proposed implicit-explicit strategy, such time integrators also ensure that the numerical solutions from both inner stages and full RK steps will stay close to the local equilibrium when $\varepsilon \ll 1$, particularly with $g^n + v\partial_x \rho^n = O(\varepsilon)$, $n \geq 2$ (see Section 5). The implicit part \mathcal{A} being triangular will render a simple system to solve. We want to point out that the IMEX-RK methods being ARS is not essential for our analysis. Compared with the A-type IMEX-RK methods which are another viable type of globally stiffly accurate IMEX-RK for our objective, the ARS type has a relatively more manageable order conditions. For instance it was proved in [6] that there is no three stage A-type IMEX-RK method that is second order accurate and globally stiffly accurate.

Remark 3.3. In the presence of the initial layer, high order versions of the scheme (3.2) will still result in first order temporal accuracy, hence it is sufficient to apply the first order scheme (3.2) directly at n = 0 in the modified scheme.

Remark 3.4. Our goal is to design AP methods with high order accuracy for ε ranging from 0 to O(1). To this end, it seems important that the numerical solutions stay sufficiently close to the local equilibrium in the diffusive regime, namely, $g^n + v\partial_x \rho^n = O(\varepsilon)$. This property is guaranteed by our proposed implicit-explicit strategy (at least for $n \ge 2$, also see Section 5). To facilitate with the understanding, in Appendix A, we examine a family of AP methods, that are closely related to our proposed methods except using a different implicit-explicit strategy as in (3.2). Both our formal analysis and numerical tests show that an insufficient approximation of the local equilibrium at the numerical level can result in temporal accuracy reduction in g (at least) in the diffusive regime with $\varepsilon \ll 1$, and this reduction may further affect the accuracy in f. Surely a mathematically more rigorous analysis would be needed to fully understand how different implicit-explicit strategies may affect the accuracy of formally high order AP methods.

3.2 Spatial discretization

For the semi-discrete methods in Section 3.1, DG methods will be further applied in space. We will start with some notation. Let $\Omega_x = [x_L, x_R]$ be the computational domain in space, with a mesh defined by $x_L = x_{\frac{1}{2}} < x_{\frac{3}{2}} < \cdots < x_{N+\frac{1}{2}} = x_R$. Let $I_i = [x_{i-\frac{1}{2}}, x_{i+\frac{1}{2}}]$ be an element with its length $h_i = x_{i+\frac{1}{2}} - x_{i-\frac{1}{2}}$ and its midpoint x_i . We set $h = \max_i h_i$. With k be any nonnegative integer, we define a finite dimensional discrete space

$$U_h^k = \{ u \in L^2(\Omega_x) : u|_{I_i} \in P^k(I_i), \forall i = 1, \dots, N \},$$
(3.6)

where the local space $P^k(I)$ consists of polynomials of degree up to k on I. For any $u \in U_h^k$, we further define its jump at $x_{i+\frac{1}{2}}$ as $[u]_{i+\frac{1}{2}} = u(x_{i+\frac{1}{2}}^+) - u(x_{i+\frac{1}{2}}^-)$. Here, $u(x^\pm) = \lim_{\Delta x \to 0^\pm} u(x + \Delta x)$, and we also use $u_{i+\frac{1}{2}} = u(x_{i+\frac{1}{2}})$, $u_{i+\frac{1}{2}}^\pm = u(x_{i+\frac{1}{2}}^\pm)$, $\forall i$.

The spatial discretization will follow a standard derivation of DG methods, with the diffusive term discretized via a local DG method, which is based on the first order form of $\partial_{xx}\rho$ with $q=\partial_x\rho$ as an auxiliary unknown. The fully discrete scheme with a first order temporal accuracy is given as follows. Given ρ_h^n , q_h^n and $g_h^n(\cdot,v)\in U_h^k$ that approximate the solution ρ , $q=\partial_x\rho$ and g at $t=t^n$, we look for ρ_h^{n+1} , q_h^{n+1} , $g_h^{n+1}(\cdot,v)\in U_h^k$ at $t^{n+1}=t^n+\Delta t$, satisfying

$$(q_h^{n+1}, \varphi) + d_h(\rho_h^{n+1}, \varphi) = 0, \quad \forall \varphi \in U_h^k$$
(3.7a)

$$\left(\frac{\rho_h^{n+1} - \rho_h^n}{\Delta t}, \phi\right) + l_h(\langle v(g_h^n + \omega v q_h^n) \rangle, \phi) = \omega \langle v^2 \rangle l_h(q_h^{n+1}, \phi), \quad \forall \phi \in U_h^k$$
(3.7b)

$$\left(\frac{g_h^{n+1} - g_h^n}{\Delta t}, \psi\right) + \frac{1}{\varepsilon} b_{h,v}(g_h^n, \psi) - \frac{v}{\varepsilon^2} d_h(\rho_h^{n+1}, \psi) = -\frac{1}{\varepsilon^2} (g_h^{n+1}, \psi), \quad \forall \psi \in U_h^k.$$
 (3.7c)

The bilinear forms in the scheme are

$$d_{h}(\rho_{h}, \psi) = \sum_{i} \int_{I_{i}} \rho_{h} \partial_{x} \psi dx + \sum_{i} \breve{\rho}_{h, i - \frac{1}{2}} [\psi]_{i - \frac{1}{2}}, \tag{3.8a}$$

$$l_h(q_h, \phi) = -\sum_i \int_{I_i} q_h \partial_x \phi dx - \sum_i \widehat{q}_{h, i - \frac{1}{2}} [\phi]_{i - \frac{1}{2}},$$
 (3.8b)

$$b_{h,v}(g_h,\psi) = ((\mathbf{I} - \Pi)\mathcal{D}_h(g_h;v),\psi) = (\mathcal{D}_h(g_h;v) - \langle \mathcal{D}_h(g_h;v)\rangle,\psi). \tag{3.8c}$$

Here (\cdot, \cdot) is the standard inner product for the $L^2(\Omega_x)$ space. For any fixed $v \in \Omega_v$, the function $\mathcal{D}_h(g_h; v) \in U_h^k$ in (3.8c) is the upwind approximation of the transport term $v\partial_x g$ within the DG framework, namely,

$$(\mathcal{D}_h(g_h; v), \psi) = -\sum_i \left(\int_{I_i} v g_h \partial_x \psi dx \right) - \sum_i \widetilde{(v g_h)}_{i - \frac{1}{2}} [\psi]_{i - \frac{1}{2}}, \quad \forall \psi \in U_h^k, \tag{3.9}$$

with \widetilde{vq} being the upwind numerical flux consistent to vq,

$$\widetilde{vg} := \begin{cases} vg^-, & \text{if } v > 0 \\ vg^+, & \text{if } v < 0 \end{cases} . \tag{3.10}$$

The terms $\check{\rho}$ and \hat{q} in (3.8) are also consistent numerical fluxes, related to the discretization of a diffusive operator. In this paper, either of the following alternating flux pairs is considered.

right-left:
$$\check{\rho} = \rho^+, \; \hat{q} = q^-;$$
 left-right: $\check{\rho} = \rho^-, \; \hat{q} = q^+.$ (3.11)

These alternating fluxes are known to lead to stable and optimally accurate DG discretizations for the diffusive operator ∂_{xx} , see [10].

We further introduce two linear operators, \mathcal{D}_h^{ρ} , $\mathcal{D}_h^q:U_h^k\to U_h^k$, satisfying

$$(\mathcal{D}_h^{\rho}\phi,\psi) = -d_h(\phi,\psi), \quad (\mathcal{D}_h^q\psi,\phi) = l_h(\psi,\phi). \tag{3.12}$$

Both approximates the spatial derivative ∂_x . They are well-defined bounded operators following the Riesz representation, and are determined entirely by the discrete space U_h^k and the involved numerical fluxes. With these, the scheme (3.7) can be rewritten into its strong form,

$$q_h^{n+1} = \mathcal{D}_h^{\rho}(\rho_h^{n+1}),$$
 (3.13a)

$$\frac{\rho_h^{n+1} - \rho_h^n}{\Delta t} + \mathcal{D}_h^q(\langle v(g_h^n + \omega v q_h^n) \rangle) = \omega \langle v^2 \rangle \mathcal{D}_h^q(q_h^{n+1}), \tag{3.13b}$$

$$\frac{g_h^{n+1} - g_h^n}{\Delta t} + \frac{1}{\varepsilon} (\mathbf{I} - \Pi) \mathcal{D}_h(g_h^n; v) + \frac{v}{\varepsilon^2} \underbrace{\mathcal{D}_h^{\rho}(\rho_h^{n+1})}_{q_h^{n+1}} = -\frac{1}{\varepsilon^2} g_h^{n+1}. \tag{3.13c}$$

Once we realize the fully discrete scheme (3.13) is obtained by replacing the spatial derivative operator in (a first order form of) (3.1) by the discrete analogue, it is straightforward to write down the fully discrete schemes with the higher order globally stiffly accuracy IMEX-RK schemes of type ARS in time. These fully discrete schemes will be referred to as IMEX-LDG methods, or IMEXp-LDG if the p-th order accuracy in time is specified, or IMEXp-LDGk if U_h^{k-1} is used in the LDG spatial discretization, with p = 1, 2, 3 and $k = 1, 2, \cdots$.

The initialization will be done for ρ, g, q via the L^2 projection onto U_h^k . In actual implementation, for less smooth $\rho(\cdot, 0)$, such as in the Riemann problem in Section 6, we instead initialize $q_h^0 \in U_h^k$ as a discrete derivative of ρ_h^0 , namely, $q_h^0 = \mathcal{D}_h^{\rho} \rho_h^0$.

 $q_h^0 \in U_h^k$ as a discrete derivative of ρ_h^0 , namely, $q_h^0 = \mathcal{D}_h^{\rho} \rho_h^0$.

The choice of the numerical fluxes is important for the discrete derivative operators \mathcal{D}_h^{ρ} and \mathcal{D}_h^q (or equivalently, d_h and d_h) to preserve some key relation of the differential operators. This is summarized in next lemma, which can be verified directly. The superscript $^{\top}$ to an operator denotes its adjoint.

Lemma 3.5. With each pair of alternating fluxes (3.11), the following holds

$$d_h(\phi, \varphi) = l_h(\varphi, \phi), \quad \forall \varphi, \phi \in U_h^k, \quad \text{or equivalently} \quad \mathcal{D}_h^{\rho} = -(\mathcal{D}_h^q)^{\top}.$$
 (3.14)

Proposition 3.6. The proposed IMEX-LDG method is uniquely solvable for any $\varepsilon > 0$.

The proof of this proposition boils down to the unique solvability of the problem examined in next lemma. And the boundedness established in next lemma will also be used in the formal asymptotic analysis of the numerical methods.

Lemma 3.7. Given $S \in L^2(\Omega_x)$ and $\gamma > 0$. Consider the following problem: look for ρ_h , $q_h \in U_h^k$, such that

$$(q_h, \varphi) + d_h(\rho_h, \varphi) = 0, \quad \forall \varphi \in U_h^k, \qquad (\rho_h, \phi) - \gamma l_h(q_h, \phi) = (S, \phi), \quad \forall \phi \in U_h^k,$$
 (3.15)

or equivalently,

$$q_h = \mathcal{D}_h^{\rho} \rho_h, \qquad \rho_h = \gamma \mathcal{D}_h^q q_h + S_h.$$
 (3.16)

Here S_h denotes the L^2 projection of S onto U_h^k . Then ρ_h and q_h are uniquely solvable. In addition, $||\rho_h|| \leq ||S||$.

Proof. Take $\varphi = q_h, \phi = \rho_h$ in (3.15), and use the relation of l_h and d_h in Lemma 3.5, we get

$$||\rho_h||^2 + \gamma ||q_h||^2 = (S, \rho_h) \le ||S|| \, ||\rho_h||. \tag{3.17}$$

Particularly if S=0, then $\rho_h=q_h=0$. This, in combination with the linearity of the problem and U_h^k being finite dimensional, indicates the uniqueness hence the unique solvability of the solution $\rho_h, q_h \in U_h^k$. From (3.17), one also obtains $||\rho_h|| \leq ||S||$.

4 Numerical stability by Fourier analysis

In this section, Fourier analysis, also referred to as von Neumann analysis, is presented to study the numerical stability of the proposed IMEXp-LDGk methods when they are applied to the telegraph equation with the discrete velocity in different regimes. Numerical experiments show that such analysis also informs about the methods when they are applied to more general models, such as the one group transport equation in slab geometry. Furthermore, the analysis in this section provides some guidance to the choice of the weight function ω , particularly see Theorem 4.1 and Theorem 4.3. Note that our schemes with or without the modification during the first few steps to address the non well-prepared initial data share the same numerical stability.

4.1 Setup of the analysis

To carry out the Fourier analysis, we assume the mesh is uniform and the boundary condition in x is periodic. Consider the IMEXp-LDGk methods with $p = 1, 2, 3, k \ge 1$ and the left-right alternating flux pair in (3.11), applied to the telegraph equation where $\Omega_v = \{-1, 1\}$. Let the numerical solutions be

$$\rho_h^n(x) = \sum_{l=0}^{k-1} \rho_{ml}^n \phi_m^l(x), \quad q_h^n(x) = \sum_{l=0}^{k-1} q_{ml}^n \phi_m^l(x), \tag{4.1a}$$

$$g_h^n(x,1) = \sum_{l=0}^{k-1} g_{+,ml}^n \phi_m^l(x), \quad g_h^n(x,-1) = \sum_{l=0}^{k-1} g_{-,ml}^n \phi_m^l(x)$$
 (4.1b)

for any $x \in I_m$. Here $\phi_m^l(x) = \phi^l(X_m)$, with $X_m = \frac{x - x_m}{h_m/2}$ and ϕ^l being the *l*-th Legendre polynomial on [-1, 1].

Recall $\langle g_h^n \rangle = 0$, this implies $g_{+,ml}^n = -g_{-,ml}^n$, $\forall n,m,l$. Moreover, q_h can be locally eliminated. We now collect the independent unknowns into $\boldsymbol{\rho}_m^n = (\rho_{m0}^n, \dots, \rho_{m-k-1}^n)^T$, $\boldsymbol{g}_m^n = (g_{+,m0}^n, \dots, g_{+,m-k-1}^n)^T$, take the ansatz $\boldsymbol{\rho}_m^n = \widehat{\boldsymbol{\rho}}^n \exp(\mathcal{I}\kappa x_m)$ and $\boldsymbol{g}_m^n = \widehat{\boldsymbol{g}}^n \exp(\mathcal{I}\kappa x_m)$ with $\mathcal{I}^2 = -1$, then our IMEXp-LDGk scheme will render

$$\begin{pmatrix} \widehat{\boldsymbol{\rho}}^{n+1} \\ \widehat{\boldsymbol{g}}^{n+1} \end{pmatrix} = \boldsymbol{G}^{\omega}(\varepsilon, h, \Delta t; \xi) \begin{pmatrix} \widehat{\boldsymbol{\rho}}^{n} \\ \widehat{\boldsymbol{g}}^{n} \end{pmatrix}, \tag{4.2}$$

where $G^{\omega}(\varepsilon, h, \Delta t; \xi)$ is a $2k \times 2k$ amplification matrix dependent of the model parameter ε , mesh size h, time step size Δt , the discrete wave number $\xi = \kappa h \in [0, 2\pi]$, and also the weight function ω in the scheme (3.1). (More details about $G^{\omega}(\varepsilon, h, \Delta t; \xi)$ can be seen from the proof of Theorem 4.1.) The following principle will be used for us to study numerical stability.

Principle for Numerical Stability: For any given $\varepsilon, h, \Delta t$, let the eigenvalues of G^{ω} be $\lambda_i(\xi)$, $i = 1, \ldots, 2k$. Our scheme is "stable", if for all $\xi \in [0, 2\pi]$, it satisfies either

(*)
$$\max_{i=1,\dots,2k} \{ |\lambda_i(\xi)| \} < 1, \quad or$$
 (4.3)

(*)
$$\max_{i=1,\dots,2k} \{|\lambda_i(\xi)|\} = 1 \quad and \quad \mathbf{G}^{\omega} \quad is \ diagonalizable. \tag{4.4}$$

This principle is a necessary condition for the standard L^2 energy to be non-increasing, and the resulting analysis provides mathematical insight regarding the stability of the proposed schemes. For the rest of this section, we will use this principle to study the stability conditions. On the other hand, what we have learned here about numerical stability through Fourier analysis seems to be quite consistent with what we have observed numerically for the schemes.

4.2 Main findings

The next theorem reveals a structure of the amplification matrix G^{ω} in terms of its dependence on $\varepsilon, h, \Delta t$ when the weight function is taken to be $\omega = 1$.

Theorem 4.1. For any given $k \geq 1$ and p = 1, 2, 3, the amplification matrix $\mathbf{G}^{\omega}(\varepsilon, h, \Delta t; \xi)$ of the IMEXp-LDGk method with the weight function $\omega = 1$ is similar to some matrix $\widehat{\mathbf{G}}(\frac{\varepsilon}{h}, \frac{\Delta t}{\varepsilon h}; \xi)$. As a direct consequence, the eigenvalues of this $\mathbf{G}^{\omega}(\varepsilon, h, \Delta t; \xi)$ depends on $\varepsilon, h, \Delta t$ only in terms of $\frac{\varepsilon}{h}$ and $\frac{\Delta t}{\varepsilon h}$, or equivalently, only in terms of $\frac{\varepsilon}{h}$ and $\frac{\varepsilon^2}{\Delta t/(\varepsilon h)}$.

Proof. Throughout the proof, we write the amplification matrix $G^{\omega}(\varepsilon, h, \Delta t; \xi)$ with the weight function $\omega = 1$ as $G(\varepsilon, h, \Delta t; \xi)$. We first consider the IMEX1-LDGk scheme defined in (3.7) with $\omega = 1$. Let us start with examining how each term in (3.7) contributes to the amplification matrix. With the notation and expansion in (4.1), we have

$$\left(\mathcal{D}_{h}^{\rho}\rho_{h}^{n+1},\phi_{m}^{l}\right)_{I_{m}} = -\sum_{s=0}^{k-1}\rho_{ms}^{n+1}\int_{I_{m}}\phi_{m}^{s}(x)\partial_{x}\phi_{m}^{l}(x)dx + \sum_{s=0}^{k-1}\rho_{ms}^{n+1}\phi_{m}^{s}(x_{m+\frac{1}{2}})\phi_{m}^{l}(x_{m+\frac{1}{2}}) - \sum_{s=0}^{k-1}\rho_{m-1\ s}^{n+1}\phi_{m-1\ s}^{s}(x_{m-\frac{1}{2}})\phi_{m}^{l}(x_{m-\frac{1}{2}}). \tag{4.5}$$

Here $(\cdot,\cdot)_{I_m}$ is the standard L^2 inner product on I_m . Substitute into (4.5) the ansatz $\rho_{ms}^{n+1} = \widehat{\rho}_s^n \exp(\mathcal{I}\kappa x_m), \forall m, \forall s$, and use $\phi_m^s(x) = \phi^s(X_m)$ with $X_m = \frac{x - x_m}{h_m/2}$, we obtain

$$\left(\mathcal{D}_h^{\rho} \rho_h^{n+1}, \phi_m^l\right)_{I_m} = \exp(\mathcal{I}\kappa x_m) \sum_{s=0}^{k-1} D_{ls}(\xi) \widehat{\rho}_s^{n+1}, \tag{4.6}$$

where $D_{ls}(\xi) = -\int_{-1}^{1} \phi^s(x) \partial_x \phi^l(x) dx + \phi^s(1) \phi^l(1) - \exp(-\mathcal{I}\xi) \phi^s(1) \phi^l(-1)$. We write $D(\xi) = \left(D_{ls}(\xi)\right) \in \mathbb{R}^{k \times k}$, and it only depends on $\xi = \kappa h$ (surely also on k).

Similarly, there exist $S(\xi) = (S_{ls}(\xi)), L(\xi) = (L_{ls}(\xi)) \in \mathbb{R}^{k \times k}$, such that

$$\left(\left((\mathbf{I} - \Pi)\mathcal{D}_h g_h^n\right)(\cdot, v = 1), \phi_m^l\right)_{I_m} = \exp(\mathcal{I}\kappa x_m) \sum_{s=0}^{k-1} S_{ls}(\xi) \widehat{g}_s^n, \quad \left(\mathcal{D}_h^q \rho_h^n, \phi_m^l\right)_{I_m} = \exp(\mathcal{I}\kappa x_m) \sum_{s=0}^{k-1} L_{ls}(\xi) \widehat{\rho}_s^n.$$

Indeed $-L(\xi) = D^* := \overline{D(\xi)}^{\top}$, that is, $-L(\xi)$ is the conjugate transpose of $D(\xi)$. We also define $M = (M_{ls}) \in \mathbb{R}^{k \times k}$, with $M_{ls} = \frac{1}{2} \int_{-1}^{1} \phi^s(x) \phi^l(x) dx$.

Based on the derivation above, the Fourier analysis for the IMEX1-LDGk method will lead to

$$\begin{pmatrix}
hM + \langle v^2 \rangle \frac{\Delta t}{h} D^* M^{-1} D & 0 \\
\Delta t D & (\varepsilon^2 + \Delta t) hM
\end{pmatrix}
\begin{pmatrix}
\widehat{\boldsymbol{\rho}}^{n+1} \\
\widehat{\boldsymbol{g}}^{n+1}
\end{pmatrix}$$

$$= \begin{pmatrix}
hM + \langle v^2 \rangle \frac{\Delta t}{h} D^* M^{-1} D & \Delta t D^* \\
0 & \varepsilon^2 hM - \varepsilon \Delta t S
\end{pmatrix}
\begin{pmatrix}
\widehat{\boldsymbol{\rho}}^n \\
\widehat{\boldsymbol{g}}^n
\end{pmatrix}.$$
(4.7)

Here $\widehat{\boldsymbol{\rho}}^n = [\widehat{\rho}_0^n, \cdots, \widehat{\rho}_{k-1}^n]^{\top}$, and $\widehat{\boldsymbol{g}}^n = [\widehat{g}_0^n, \cdots, \widehat{g}_{k-1}^n]^{\top}$. We further left-multiply $\begin{pmatrix} \frac{1}{\varepsilon}I & 0\\ 0 & \frac{1}{\varepsilon h^2}I \end{pmatrix}$ to both sides of (4.7), and get

$$\underbrace{\begin{pmatrix} \frac{h}{\varepsilon}M + \langle v^2 \rangle \frac{\Delta t}{\varepsilon h} D^* M^{-1} D & 0 \\ \frac{\Delta t}{\varepsilon h^2} D & (\frac{\varepsilon}{h} + \frac{\Delta t}{\varepsilon h}) M \end{pmatrix}}_{G_L} \left(\widehat{\boldsymbol{\rho}}^{n+1} \right) \\
= \underbrace{\begin{pmatrix} \frac{h}{\varepsilon}M + \langle v^2 \rangle \frac{\Delta t}{\varepsilon h} D^* M^{-1} D & \frac{\Delta t}{\varepsilon} D^* \\ 0 & \frac{\varepsilon}{h} M - \frac{\Delta t}{\varepsilon h} \cdot \frac{\varepsilon}{h} S \end{pmatrix}}_{G_R} \left(\widehat{\boldsymbol{\rho}}^n \right), \tag{4.8}$$

and hence the amplification matrix $G(\varepsilon, h, \Delta t; \xi) = G_L^{-1}G_R$. One can verify that this matrix G is similar to $\widehat{G}(\frac{\varepsilon}{h}, \frac{\Delta t}{\varepsilon h}; \xi)$, more specifically,

$$\begin{pmatrix} hI & 0 \\ 0 & I \end{pmatrix}^{-1} \boldsymbol{G}(\varepsilon, h, \Delta t; \xi) \begin{pmatrix} hI & 0 \\ 0 & I \end{pmatrix} = \widehat{\boldsymbol{G}}(\frac{\varepsilon}{h}, \frac{\Delta t}{\varepsilon h}; \xi),$$

where $\widehat{\boldsymbol{G}}(\frac{\varepsilon}{h}, \frac{\Delta t}{\varepsilon h}; \xi) =$

$$\begin{pmatrix} \frac{h}{\varepsilon}M + \langle v^2 \rangle \frac{\Delta t}{\varepsilon h}D^\star M^{-1}D & 0 \\ \frac{\Delta t}{\varepsilon h}D & (\frac{\varepsilon}{h} + \frac{\Delta t}{\varepsilon h})M \end{pmatrix}^{-1} \begin{pmatrix} \frac{h}{\varepsilon}M + \langle v^2 \rangle \frac{\Delta t}{\varepsilon h}D^\star M^{-1}D & \frac{\Delta t}{\varepsilon h}D^\star \\ 0 & \frac{\varepsilon}{h}M - \frac{\Delta t}{\varepsilon h} \cdot \frac{\varepsilon}{h}S \end{pmatrix}.$$

For the general IMEXp-LDGk method with p = 2, 3, we can carry out a similar analysis as above. Particularly, for the l-th inner stage, we have

$$\begin{pmatrix} \widehat{\boldsymbol{\rho}}^{n,(l)} \\ \widehat{\boldsymbol{g}}^{n,(l)} \end{pmatrix} = \boldsymbol{G}_l(\varepsilon, h, \Delta t; \xi) \begin{pmatrix} \widehat{\boldsymbol{\rho}}^n \\ \widehat{\boldsymbol{g}}^n \end{pmatrix},$$

one can then show

$$\left(\begin{array}{cc} hI & 0 \\ 0 & I \end{array}\right)^{-1} \boldsymbol{G}_l(\varepsilon,h,\Delta t;\xi) \left(\begin{array}{cc} hI & 0 \\ 0 & I \end{array}\right) = \widehat{\boldsymbol{G}}_l(\frac{\varepsilon}{h},\frac{\Delta t}{\varepsilon h};\xi)$$

for some $\widehat{G}_l(\frac{\varepsilon}{h}, \frac{\Delta t}{\varepsilon h}, \xi)$. With the identical similarity transformation for *all* inner stages, the theorem will hold for p = 2, 3.

Remark 4.2. The structure of the amplification matrix G^{ω} with $\omega = 1$ shown in Theorem 4.1 is essentially due to the diffusive scaling of the model.

The result in Theorem 4.1 shows that numerical stability of the proposed schemes with the weight function $\omega=1$ depends on $\varepsilon,h,\Delta t$ only in terms of ε/h and $\varepsilon^2/\Delta t$. In order for this intrinsic structure not affected by the weight function ω , one should choose ω as a function of ε/h and $\varepsilon^2/\Delta t$ only. By taking into account the property in (2.6), some suitable weight functions include $\omega=\exp(-\varepsilon/h)$ and $\omega=\exp(-\varepsilon^2/\Delta t)$. On the other hand, the weight $\exp(-\varepsilon^2/h)$ used in [5] does not keep such scaling structure of the amplification matrix, while the piecewise constant weight $\omega=\chi_{\{\varepsilon< h\}}$ in [4] does (here χ_E is an indicator function associated with the set E). The discussion above leads to the next theorem, which can be established just as for Theorem 4.1.

Theorem 4.3. The result in Theorem 4.1 holds as long as the weight ω in the scheme is a function of $\frac{\varepsilon}{h}$ and $\frac{\Delta t}{\varepsilon h}$, or equivalently, it is a function of $\frac{\varepsilon}{h}$ and $\frac{\varepsilon^2}{\Delta t}$.

4.3 Numerical results

We are now ready to present the results from the stability analysis. Motivated by Theorem 4.1 and Theorem 4.3, and based on the stability principle, we plot stability regions in terms of $\sigma = \log_{10}(\varepsilon/h)$ and $\eta = \log_{10}(\Delta t/(\varepsilon h))$ in Figure 4.1 for $\omega = 1$, and in Figure 4.2 for $\omega = \exp(-\varepsilon/h)$ and $\omega = \exp(-\varepsilon/h)$. What we also plot are the results for the methods with the weight function $\omega = 0$ in Figure 4.3, and in this case, our methods recover the DG*p*-IMEX*p* methods proposed in [15]. The white region in each plot represents the stable region. Both σ and η are sampled with a spacing 1/40, and the discrete wave number ξ is uniformly taken from $[0, 2\pi]$ with 100 samples. As the horizontal axis $\sigma = \log_{10}(\varepsilon/h)$ goes from the left to right, the spatial mesh starts from being under-resolved to being resolved with respect to the ε -scale of the model, hence the model goes from its diffusive regime to its kinetic (or transport) regime. Our observations are summarized below.

1. When the weight function is $\omega = 1, \exp(-\varepsilon/h)$, or $\omega = \exp(-\varepsilon^2/\Delta t)$, the IMEX*p*-LDG*p* scheme (with p = 1, 2, 3) is unconditionally stable with no restriction on the time step size Δt when $\sigma < \sigma_{p,\omega}$, or equivalently when $\varepsilon/h < R_{p,\omega}$. Here $\sigma_{p,\omega}$ and $R_{p,\omega}$ are some constants. This confirms the proposed schemes are unconditionally stable in the diffusive regime, measured by sufficiently small ε/h . In this regime, $\exp(-\varepsilon/h) \approx 1$ and $\exp(-\varepsilon^2/\Delta t) \approx 1$, and the proposed method with all three weights are very "close" and hence with comparable $\sigma_{p,\omega}$ for a given p.

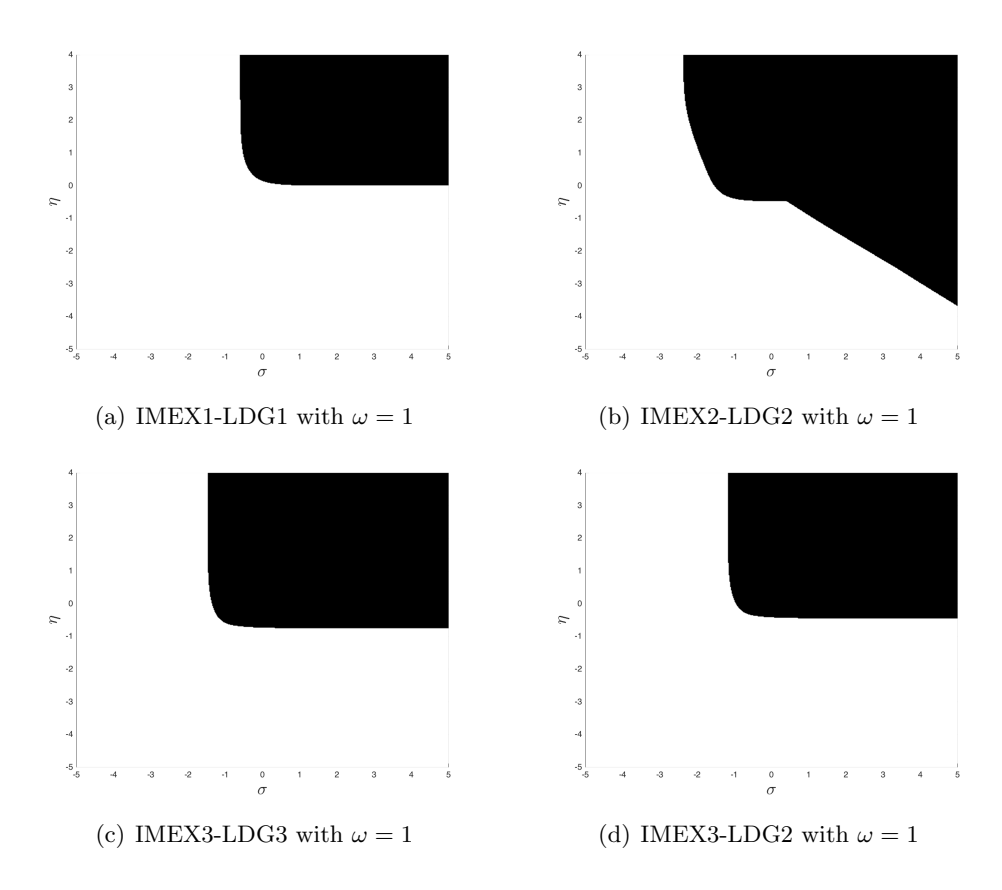


Figure 4.1: Stability regions of the IMEX*p*-LDG*k* methods with the weight function $\omega=1$. White: stable; black: unstable.

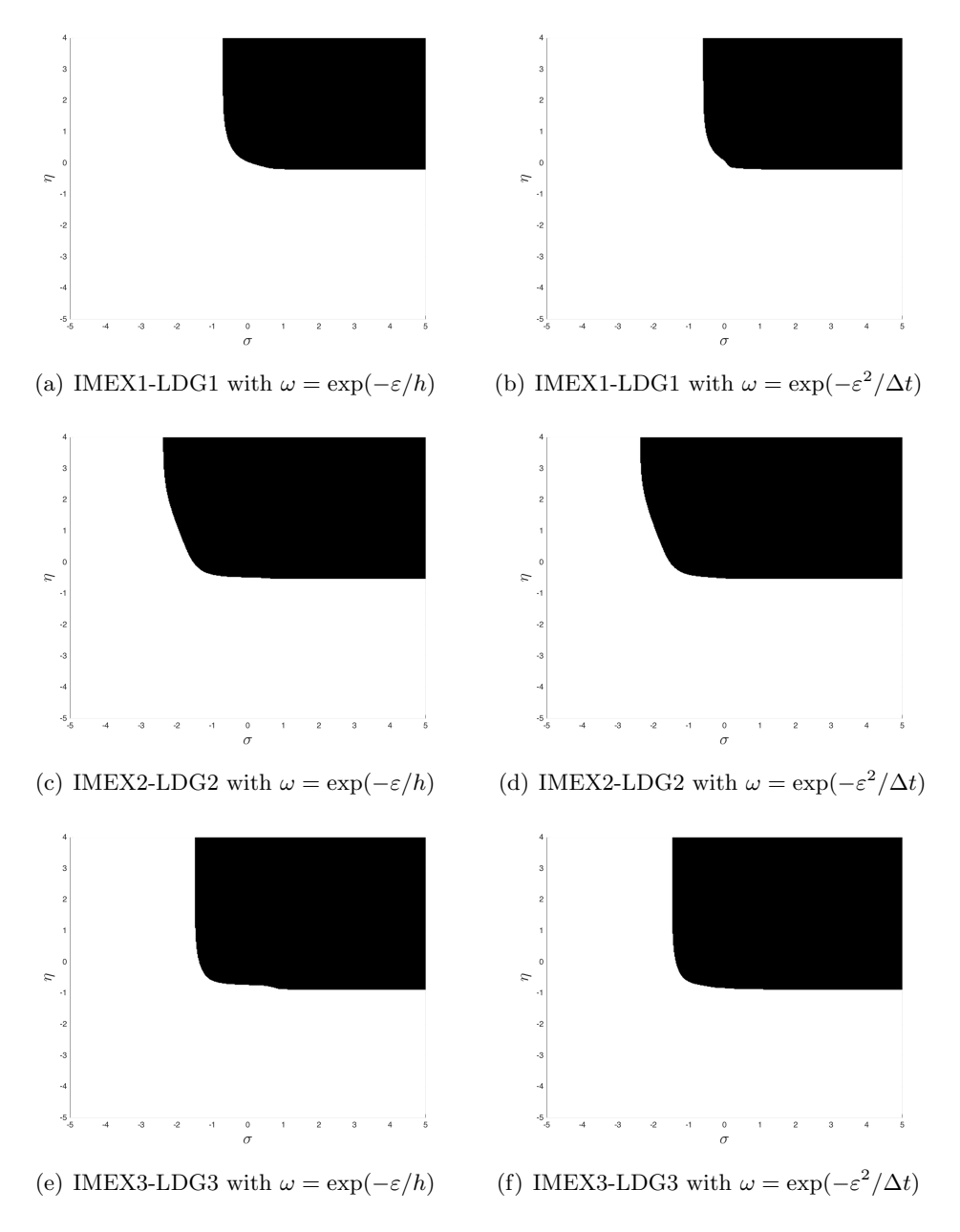


Figure 4.2: Stability regions of the IMEX*p*-LDG*k* methods with the weight function $\omega = \exp(-\varepsilon/h)$ and $\omega = \exp(-\varepsilon^2/\Delta t)$. White: stable; black: unstable.

- 2. When the weight function is $\omega = 1, \exp(-\varepsilon/h)$, or $\omega = \exp(-\varepsilon^2/\Delta t)$, and under the condition $\sigma \geq \sigma_{p,\omega}$, the IMEX*p*-LDG*p* scheme (with p = 1, 2, 3) is conditionally stable. And the boundary of the conditionally stable region is determined by a function $\mathcal{F}_{p,\omega}$, that is, the scheme is stable when $\eta \leq \mathcal{F}_{p,\omega}(\sigma)$.
 - 2.a) With the scale- and mesh-dependent weight function $\omega = \exp(-\varepsilon/h)$ and $\exp(-\varepsilon^2/\Delta t)$, it is observed that the function $\mathcal{F}_{p,\omega}(\sigma) \approx C_{p,\omega}$ when $\sigma \gg 1$ for p = 1, 2, 3. Here $C_{p,\omega}$ is some constant. This implies that when the regime is relatively kinetic (or transport) with $h \ll \varepsilon$, the conditional stability requires approximately

$$\log_{10}(\frac{\Delta t}{\varepsilon h}) \le C_{p,\omega},$$

corresponding to a hyperbolic type time step condition $\Delta t = O(\varepsilon h)$. This is highly desirable numerically. With the constant weight function $\omega = 1$, similar observation can be made when p = 1, 3, not when p = 2.

2.b) For the scheme with the constant weight function $\omega = 1$ and p = 2, the boundary of the stability region becomes a straight line with a slope approximately -1 for large σ . That is, the function $\mathcal{F}_{p,\omega}(\sigma) \approx -\sigma + C_{p,\omega}$ when $\sigma \gg 1$, with $C_{p,\omega}$ being some constant. This implies in the kinetic regime with $h \ll \varepsilon$, the conditional stability of the method requires approximately

$$\log_{10}(\frac{\Delta t}{\varepsilon h}) \le -\log_{10}(\frac{\varepsilon}{h}) + C_{p,\omega}.$$

This corresponds to $\Delta t = O(h^2)$, a parabolic time step restriction for stability in this regime. Such time step restriction, though not desirable, is also confirmed numerically. With the same spatial discretization (namely the LDG2 method and $\omega = 1$), if we apply a more costly temporal discretization, the third order ARS(4,4,3) scheme in time, the resulting IMEX3-LDG2 method will display the desired stability property in both the diffusive and kinetic regimes, namely the unconditional stability in the diffusive regime and the hyperbolic time step condition in the kinetic regime, see the final plot in Figure 4.1.

3. When the weight function is $\omega=0$, our proposed IMEXp-LDGp methods (p=1,2,3) are exactly the DGp-IMEXp methods previously designed and studied in [15]. Note that this zero weight does not satisfy the property in (2.6), and the unconditional stability is not expected in the diffusive regime. From Figure 4.3, one can observe that in the kinetic regime, the methods require hyperbolic time step condition. This is expected as the IMEX-LDG methods with the weight $\omega=\exp(-\varepsilon/h), \exp(-\varepsilon^2/\Delta t)$ and $\omega=0$ are very "close" when $\varepsilon\gg h$. In the diffusive regime when $\varepsilon\ll h$, the DGp-IMEXp methods requires a parabolic time step condition $\Delta t=O(h^2)$. Recall this is one motivation for the present work.

5 Formal asymptotic analysis with initial layers: numerical methods

In this section, we assume $\varepsilon \ll 1$ and perform a formal asymptotic analysis for the proposed schemes with the small ε while the mesh parameters h and Δt are fixed. The main objective is to show the schemes are asymptotic preserving (AP), namely, the limiting schemes as $\varepsilon \to 0$ are consistent discretizations of the limiting equation. In the presence of the initial layer, the limiting equation is referred to as the interior heat equation (2.11) ((2.12)) with the asymptotically consistent initial data (2.18). In addition, we will show the limiting schemes are of formally high order accuracy. The initial data $f(x,v,0;\varepsilon) = \rho(x,0;\varepsilon) + \varepsilon g(x,v,0;\varepsilon)$ is taken as (2.7) (also see (2.8)). With this, $\rho(x,0;\varepsilon) = O(1)$, yet $g(x,v,0;\varepsilon) = O(\varepsilon^{-1})$ in general, unless other property is specified for the initial data (e.g. being well-prepared). The following assumptions are further made for the initial data.

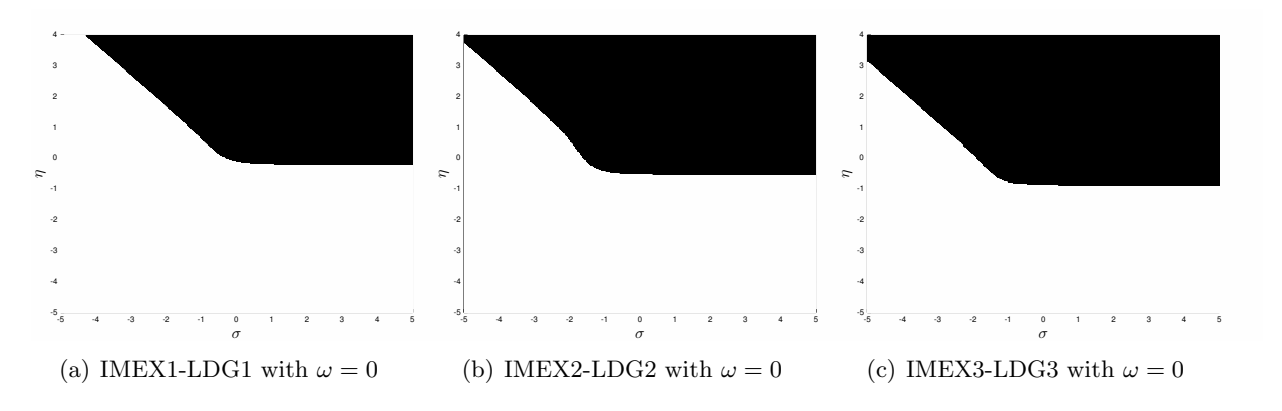


Figure 4.3: Stability regions of the IMEX*p*-LDG*p* methods with $\omega = 0$ (the methods are also the DG*p*-IMEX*p* methods in [15]). White: stable; black: unstable.

Assumption: All spatial derivatives of ρ at t=0, namely $||\partial_x^{(m)}\rho(\cdot,0;\varepsilon)||$ with $m=1,2,\cdots$, have comparable scales as $||\rho(\cdot,0;\varepsilon)||$ with respect to ε . Similarly all spatial derivatives of g at t=0, namely $||\partial_x^{(m)}g(\cdot,v,0;\varepsilon)||$ with $m=1,2,\cdots$, have comparable scales as $||g(\cdot,v,0;\varepsilon)||$ with respect to ε . For instance, they can all be O(1), or all be $O(\varepsilon^{-1})$.

Under this assumption, it is reasonable to state that, at the discrete level, the discrete spatial derivatives of ρ (resp. q, g) of all orders, such as $\mathcal{D}_h^{\rho}\mathcal{D}_h^{q}$, $\mathcal{D}_h^{q}\mathcal{D}_h^{\rho}$, $\mathcal{D}_h^{\rho}\mathcal{D}_h^{\rho}$ that are defined based on one or more from \mathcal{D}_h^{ρ} , \mathcal{D}_h^{q} , \mathcal{D}_h , have comparable scales as ρ (resp. q, g) respect to ε . As for the small parameters ε , h, and Δt , it is assumed that $\varepsilon^2 \ll \Delta t$. That is, the exact solution exits from the initial layer (if it exists) by the time $t = \Delta t$, and the temporal mesh is under-resolved with respect to the initial layer feature. In addition, we assume $\varepsilon \leq \Delta t \leq 1$, $\Delta t/h = O(1)$ to avoid explicit dependence on Δt , h of the hidden constant in the big-O notation. For instance, under this assumption, $\varepsilon/(\varepsilon^2 + \Delta t) \leq 1$ holds.

This section is organized as follows. In Section 5.1, the formal asymptotic analysis is carried out for the first order semi-discrete temporal scheme, IMEX1, for both the well-prepared and non well-prepared initial data. In Section 5.2, the analysis will be done for the fully discrete IMEX1-LDG methods, to illustrate the role of the spatial discretization. Finally in Section 5.3, we analyze the method involving higher order IMEX-RK temporal discretizations, to see how the structures of the adopted IMEX-RK methods, namely being globally stiffly accurate and being type ARS, work for the proposed methods to achieve the AP property. For the clarity of the presentation, we will focus on the analysis for the schemes with the weight function $\omega=1$. More general weight functions will be discussed in Section 5.2.

5.1 Semi-discrete temporal scheme: IMEX1

In this section, we consider the semi-discrete temporal IMEX1 scheme in Section 3.1 with the weight function $\omega = 1$. Let $R^n = g^n + v\partial_x \rho^n$, then the IMEX1 scheme in (3.1) leads to the following updates for ρ^{n+1} , g^{n+1} , and R^{n+1} ,

$$\rho^{n+1} = \rho^n + \Delta t \langle v^2 \rangle \partial_{xx} \rho^{n+1} - \Delta t \partial_x \langle v R^n \rangle, \tag{5.1a}$$

$$g^{n+1} = \frac{\varepsilon^2}{\varepsilon^2 + \Delta t} g^n - \frac{\varepsilon \Delta t}{\varepsilon^2 + \Delta t} (\mathbf{I} - \Pi) (v \partial_x g^n) - \frac{\Delta t}{\varepsilon^2 + \Delta t} (v \partial_x \rho^{n+1}), \tag{5.1b}$$

$$R^{n+1} = \frac{\varepsilon^2}{\varepsilon^2 + \Delta t} (g^n + v \partial_x \rho^{n+1}) - \frac{\varepsilon \Delta t}{\varepsilon^2 + \Delta t} (\mathbf{I} - \Pi) (v \partial_x g^n).$$
 (5.1c)

Based on the classical PDE theory for the well-posedness of second order elliptic equations, one can get the unique solvability of ρ^{n+1} from (5.1a), and additionally $||\rho^{n+1}|| \leq C(||\rho^n|| + ||\partial_x \langle vR^n \rangle||)$ for some generic constant C.

When there is an initial layer, the proposed modification (3.2) to the first time step with

n=0 leads to a different set of updates,

$$g^{1} = \frac{\varepsilon^{2}}{\varepsilon^{2} + \Delta t} g^{0} - \frac{\varepsilon \Delta t}{\varepsilon^{2} + \Delta t} \left(\mathbf{I} - \Pi \right) \left(v \partial_{x} g^{0} \right) - \frac{\Delta t}{\varepsilon^{2} + \Delta t} v \partial_{x} \rho^{0}, \tag{5.2a}$$

$$\rho^{1} = \rho^{0} + \Delta t \langle v^{2} \rangle \partial_{xx} \rho^{0} - \Delta t \left(\frac{\varepsilon^{2}}{\varepsilon^{2} + \Delta t} \langle vR^{0} \rangle - \frac{\varepsilon \Delta t}{\varepsilon^{2} + \Delta t} \langle v^{2} \partial_{xx} g^{0} \rangle \right), \tag{5.2b}$$

$$R^{1} = \frac{\varepsilon^{2}}{\varepsilon^{2} + \Delta t} R^{0} - \frac{\varepsilon \Delta t}{\varepsilon^{2} + \Delta t} (\mathbf{I} - \Pi) \left(v \partial_{x} g^{0} \right)$$

$$+ v\Delta t \langle v^2 \rangle \partial_{xxx} \rho^n - v\Delta t \left(\frac{\varepsilon^2}{\varepsilon^2 + \Delta t} \partial_x \langle vR^0 \rangle - \frac{\varepsilon \Delta t}{\varepsilon^2 + \Delta t} \langle v^2 \partial_{xxx} g^0 \rangle \right). \tag{5.2c}$$

The initial data being well-prepared corresponds to $R^0 = O(\varepsilon)$. Under the assumption of the initial data (2.7), the more general data would lead to $R^0 = O(\varepsilon^{-1})$. Accordingly, we examine two cases to understand the behavior of the schemes when $\varepsilon \ll 1$.

Case 1: the initial is well-prepared with $R^0 = O(\varepsilon)$. In this case, following mathematical induction in n, one can show that the updates in (5.1) with $\varepsilon \ll 1$ lead to

- $\rho^n, g^n = O(1), \, \partial_x \rho^n, \partial_x g^n = O(1), \, \forall n \ge 0;$
- $R^n = g^n + v\partial_x \rho^n = O(\varepsilon), \forall n \geq 0$; that is, the numerical solution stays within the $O(\varepsilon)$ -width neighborhood of the local equilibrium. In addition, $\partial_x \langle vR^n \rangle = O(\varepsilon), \forall n \geq 0$;
- ρ^n satisfies

$$\frac{\rho^{n+1} - \rho^n}{\Delta t} = \langle v^2 \rangle \partial_{xx} \rho^{n+1} + O(\varepsilon), \quad \forall n \ge 0.$$
 (5.3)

Here the estimates for the spatial derivatives of $\rho^n, g^n, \langle vR^n \rangle$ are obtained similarly as for ρ^n, g^n, R^n after one differentiates each equation in (5.2) with respect to x and uses the assumption on the initial data and the spatial derivatives. In this case with the well-prepared initial, the limiting scheme as $\varepsilon \to 0$ is a consistent scheme of the first order temporal accuracy for the limiting heat equation, and more specifically, the scheme involves a backward Euler method in time with the consistent initial data. And the computed ρ and g satisfies the local equilibrium property. This shows the IMEX1 scheme is AP.

Case 2: the initial is not well-prepared with $R^0 = O(\varepsilon^{-1})$. In this case and with $\varepsilon \ll 1$, the updates in (5.1) for $n \geq 1$ and in (5.2) for n = 0 lead to

- $\rho^n, g^n = O(1), \ \partial_x \rho^n, \partial_x g^n = O(1), \ \forall n \geq 1$, even though $\rho^0, \partial_x \rho^0 = O(1)$ and $g^0, \partial_x g^0 = O(\varepsilon^{-1})$.
- $R^n = g^n + v\partial_x \rho^n = O(\varepsilon)$, $\partial_x \langle vR^n \rangle = O(\varepsilon)$, $\forall n \geq 2$, while $R^0, \partial_x \langle vR^0 \rangle = O(\varepsilon^{-1})$ and $R^1, \partial_x \langle vR^1 \rangle = O(1)$.
- ρ^n satisfies

$$\frac{\rho^{n+1} - \rho^n}{\Delta t} = \langle v^2 \rangle \partial_{xx} \rho^{n+1} + O(\varepsilon), \quad \forall n \ge 2,$$
 (5.4)

while at n = 0, 1, it satisfies

$$\rho^{1} = \rho^{0} + \Delta t \langle v^{2} \rangle \partial_{xx} \rho^{0} + O(\Delta t), \qquad \rho^{2} = \rho^{1} + \Delta t \langle v^{2} \rangle \partial_{xx} \rho^{2} + O(\Delta t). \tag{5.5}$$

In Case 2, even though the local truncation errors at the first two steps are O(1), the local errors in ρ^1 and ρ^2 are of first order in Δt , hence the limiting scheme as $\varepsilon \to 0$ of the IMEX1 scheme is still a first order consistent discretization of the limiting interior heat equation with the asymptotically consistent initial condition. Particularly, the limiting scheme involves a perturbed forward Euler method of the first order accuracy during the first time step, a perturbed backward Euler method of the first order accuracy during the second time step, and a standard backward Euler method afterward. The solution of the limiting scheme satisfies the local equilibrium property when $n \geq 2$ (after the first two steps and away from the initial layer). Hence the proposed IMEX1 scheme with the modified first step treatment is still AP.

Remark 5.1. The analysis above can be improved based on more refined classification of the initial data. For example, there is an intermediate case with $R^0 = O(1)$. Moreover, a close examination shows that the initial quantity R^0 comes into play in (5.1a) via its first moment in v, namely $\langle vR^0 \rangle$, instead of R^0 itself. And $\langle vR^0 \rangle$ could be much smaller than R^0 with respect to ε . In Table 5.1, we summarize the accuracy of the semi-discrete temporal scheme IMEX1 (and indeed IMEXp, with p = 1, 2, 3) when it is applied to cases with various size of the initial data $\langle vR^0 \rangle$ with respect to ε and when the scheme is *not* modified during the initial steps to address the possible accuracy loss or reduction. From the table, one can see that with p = 1, only the worst case, namely $\langle vR^0 \rangle = O(\varepsilon^{-1})$, requires a modified version of the IMEX1 scheme to achieve the first order temporal accuracy. In practice, the initial data is often given as $f|_{t=0} = f_0$, and R^0 and $\langle vR^0 \rangle$ can be expressed in terms of f_0 as follows

$$R^{0} = \frac{f_{0} - \langle f_{0} \rangle}{\varepsilon} + v \partial_{x} \langle f_{0} \rangle, \quad \langle vR^{0} \rangle = \langle v^{2} \rangle \partial_{x} \langle f_{0} \rangle + \frac{1}{\varepsilon} \langle vf_{0} \rangle.$$
 (5.6)

Table 5.1: The relation between the initial data and the accuracy of the semi-discrete temporal IMEXp scheme without any special modification during the initial steps to address the potential accuracy loss and reduction for $\varepsilon \ll 1$. The IMEXp scheme here refers to the scheme in (3.1) for p = 1 and scheme in (5.14)-(5.15) for general p, with $n \ge 0$. Here $R^0 = g^0 + v \partial_x \rho^0$.

initial being well-prepared?	R^0	IMEXp
yes, with $R^0 = O(\varepsilon)$	$R^0 = O(\varepsilon)$	$O(\Delta t^p)$
no, with $R^0 = O(1)$	$\langle vR^0\rangle = O(\varepsilon)$	$O(\Delta t^p)$
mo, with $m = O(1)$	$\langle vR^0\rangle = O(1)$	$O(\Delta t_1)$
no, with $R^0 = O(\varepsilon^{-1})$	$\langle vR^0\rangle = O(\varepsilon)$	$O(\Delta t_1) + O(\Delta t_2)$
mo , with $m = O(\varepsilon)$	$\langle vR^0\rangle = O(1)$	$O(\Delta t_1) + O(\Delta t_2)$
	$\langle vR^0\rangle = O(\varepsilon^{-1})$	$O(\varepsilon^{-1})$

5.2 Fully discrete scheme: IMEX1-LDG

In this section, we will consider the fully discrete scheme in Section 3.2, the IMEX1-LDG method with the first order accuracy in time. The focus will be on understanding the role of the spatial discretization. We start with the schemes with the weight function $\omega = 1$, and then discuss the cases with more general weight functions.

The analysis can be based on the numerical scheme either of its integral form (3.7), or its equivalent strong form (3.13). We will follow the latter for a more clear presentation. Based on (3.13), one gets the following updates for $\rho_h^{n+1}, q_h^{n+1}, g_h^{n+1}$, as well as for $R_h^{n+1} := g_h^{n+1} + v q_h^{n+1}$,

$$q_h^{n+1} - \mathcal{D}_h^{\rho}(\rho_h^{n+1}) = 0,$$
 (5.7a)

$$\rho_h^{n+1} - \Delta t \langle v^2 \rangle \mathcal{D}_h^q(q_h^{n+1}) = \rho_h^n - \Delta t \mathcal{D}_h^q(\langle vR_h^n) \rangle), \tag{5.7b}$$

$$g_h^{n+1} = \frac{\varepsilon^2}{\varepsilon^2 + \Delta t} g_h^n - \frac{\varepsilon \Delta t}{\varepsilon^2 + \Delta t} (\mathbf{I} - \Pi) (\mathcal{D}_h(g_h^n; v)) - \frac{\Delta t}{\varepsilon^2 + \Delta t} v q_h^{n+1}, \tag{5.7c}$$

$$R_h^{n+1} = \frac{\varepsilon^2}{\varepsilon^2 + \Delta t} (g_h^n + v q_h^{n+1}) - \frac{\varepsilon \Delta t}{\varepsilon^2 + \Delta t} (\mathbf{I} - \Pi) (\mathcal{D}_h(g_h^n; v)).$$
 (5.7d)

The unique solvability of q_h^{n+1} and ρ_h^{n+1} from (5.7a)-(5.7b) is guaranteed by Lemma 3.7, and additionally, $||\rho_h^{n+1}|| = C(||\rho_h^n|| + \Delta t||\mathcal{D}_h^{\rho}\langle vR_h^n\rangle||)$, with some generic constant C. From this, (5.7) and the assumption on the initial data (especially its discrete analogue), one can conclude that with the well-prepared initial data satisfying $R_h^0 = O(\varepsilon)$,

•
$$\rho_h^n, q_h^n, g_h^n = O(1), \mathcal{D}_h(g_h^n; v) = O(1), \forall n \ge 0;$$

•
$$R_h^n = g_h^n + vq_h^n = O(\varepsilon), \ \mathcal{D}_h^q(\langle vR_h^n \rangle) = O(\varepsilon), \ \forall n \ge 0;$$

• ρ_h^n and q_h^n satisfy

$$q_h^{n+1} = \mathcal{D}_h^{\rho}(\rho_h^{n+1}), \quad \frac{\rho_h^{n+1} - \rho_h^n}{\Delta t} = \langle v^2 \rangle \mathcal{D}_h^q(q_h^{n+1}) + O(\varepsilon), \quad \forall n \ge 0.$$
 (5.8)

Here the estimate for q_h^n is obtained similarly as for the semi-discrete case, namely, by applying \mathcal{D}_h^q to (5.7a) and \mathcal{D}_h^ρ to (5.7b) and utilizing that Lemma 3.7 holds if one switch \mathcal{D}_h^q and \mathcal{D}_h^ρ in (3.16). Now with the fixed h and Δt , the limiting scheme as $\varepsilon \to 0$ is a consistent scheme for the limiting heat equation, and it involves the first order backward Euler method in time, and a local DG method in space with the discrete space U_h^k , together with the consistent initial data. And the computed g, q satisfies the local equilibrium property. This shows the IMEX1-LDG scheme is AP. Note that the analysis shares great similarity as that for the semi-discrete IMEX1 scheme, due to the property of Lemma 3.5. When the initial condition is not well-prepared, the formal asymptotic analysis can be done similarly as for the IMEX1 scheme with the modification during the first time step, and similar conclusions can be obtained as in Table 5.1, except that the accuracy in Table 5.1 is only for temporal accuracy, and in space, the scheme has the designed formal (high order) spatial accuracy of the local DG method.

For the limiting scheme, one can also write down its integral form when the initial data is well-prepared: look for $\rho_h^{n+1}, q_h^{n+1}, g_h^{n+1}(\cdot, v) \in U_h^k$, such that

$$(q_h^{n+1}, \varphi) = -d_h(\rho_h^{n+1}, \varphi), \quad \forall \varphi \in U_h^k, \tag{5.9a}$$

$$\left(\frac{\rho_{h}^{n+1} - \rho_{h}^{n}}{\Delta t}, \phi\right) = \langle v^{2} \rangle l_{h}(q_{h}^{n+1}, \phi), \quad \forall \phi \in U_{h}^{k},
(g_{h}^{n+1}, \psi) = v d_{h}(\rho_{h}^{n+1}, \psi) = -(v q_{h}^{n+1}, \psi), \quad \forall \psi \in U_{h}^{k},$$
(5.9b)

$$(g_h^{n+1}, \psi) = v d_h(\rho_h^{n+1}, \psi) = -(v q_h^{n+1}, \psi), \quad \forall \psi \in U_h^k,$$
 (5.9c)

for $n \ge 0$. In fact, (5.9c) implies $g_h^{n+1} = -vq_h^{n+1}$.

Finally in this section, we want to take a look at the schemes with a more general weight function ω , which satisfies (2.6). All the updates in (5.7) stay the same except for the second equation (5.7b) to be replaced by

$$\rho_h^{n+1} - \omega \Delta t \langle v^2 \rangle \mathcal{D}_h^q(q_h^{n+1}) = \rho_h^n - \Delta t \mathcal{D}_h^q(\langle v R_h^n \rangle) - (\omega - 1) \Delta t \langle v^2 \rangle \mathcal{D}_h^q(q_h^n). \tag{5.10}$$

Similar as for the case when $\omega = 1$, with $\varepsilon \ll 1$ and the well-prepared initial data, one can get $\rho_h^n, q_h^n, g_h^n, \mathcal{D}_h(g_h^n; v) = O(1), R_h^n = g_h^n + vq_h^n = O(\varepsilon), \mathcal{D}_h^q(\langle vR_h^n \rangle) = O(\varepsilon), \forall n \geq 0.$ Moreover, $\mathcal{D}_h^q(q_h^{n+1} - q_h^n)/\Delta t = O(1).$ Now the solution ρ_h^n and q_h^n satisfy, $\forall n \geq 0$,

$$q_h^{n+1} = \mathcal{D}_h^{\rho}(\rho_h^{n+1})$$

and

$$\frac{\rho_h^{n+1} - \rho_h^n}{\Delta t} = \langle v^2 \rangle \mathcal{D}_h^q(q_h^{n+1}) - \underbrace{\mathcal{D}_h^q(\langle vR_h^n \rangle)}_{O(\varepsilon)} + (\omega - 1)\langle v^2 \rangle \underbrace{\mathcal{D}_h^q(q_h^{n+1} - q_h^n)}_{O(\Delta t)}$$
(5.11)

$$= \langle v^2 \rangle \mathcal{D}_h^q(q_h^{n+1}) - O(\varepsilon) + (\omega - 1)O(\Delta t). \tag{5.12}$$

One can see that as long as

$$(\omega - 1)O(\Delta t) = O(\varepsilon), \tag{5.13}$$

the limiting scheme will be a consistent implicit discretization of the limiting heat equation, hence the proposed methods are AP. The two scale- and mesh-dependent choices, $\omega = \exp(-\varepsilon/h)$ and $\omega = \exp(-\varepsilon^2/\Delta t)$, suggested by the numerical stability analysis, satisfy the property (5.13) under our assumption $\Delta t/h = O(1)$.

5.3 Higher order temporal discretizations: IMEXp

What remained is to understand the semi- and fully-discrete schemes with higher order temporal discretizations. Since the spatial discretization does not essentially affect the analysis (just as for the first order case in Sections 5.1-5.2), we here only focus on the semi-discrete temporal IMEXp scheme in this section. Such analysis also informs us the asymptotic behavior of the fully-discrete IMEXp-LDGk scheme.

In our IMEXp scheme, globally stiffly accurate IMEX-RK methods of type ARS, denoted as ARS(s,s,p), are applied. These are one-step p-th order method with effective s stages (see Section 3.1 for the specific form of the schemes for p=1,2,3). Based on the definitions, the time integrators being globally stiffly accurate ensures that the numerical solution at t^{n+1} is the same as that from the last inner stage of the RK step; and with the type ARS structure, the solutions from the first inner stage are the same as that from the previous RK step. Using these features, and following the same implicit-explicit strategy used in the IMEX1 scheme, the IMEXp scheme is: given the numerical solution p^n, g^n at $t=t^n$, we look for p^{n+1}, g^{n+1} at $t^{n+1}=t^n+\Delta t$, such that

$$\rho^{n+1} = \rho^{n,(s)}, \quad g^{n+1} = g^{n,(s)},$$
(5.14)

where $\rho^{n,(l)}, g^{n,(l)}, l = 0, \dots, s$, are from inner stages, satisfying

$$\rho^{n,(0)} = \rho^n, \quad g^{n,(0)} = g^n,$$
(5.15a)

$$\rho^{n,(l)} = \rho^n - \Delta t \sum_{j=0}^{l-1} \tilde{a}_{lj} \left(\partial_x \langle v(g^{n,(j)} + v \partial_x \rho^{n,(j)}) \rangle \right) + \Delta t \sum_{j=1}^{l} a_{lj} \left(\langle v^2 \rangle \partial_{xx} \rho^{n,(j)} \right), \ l = 1, \dots, s,$$
(5.15b)

$$g^{n,(l)} = g^{n} - \frac{\Delta t}{\varepsilon} \sum_{j=0}^{l-1} \tilde{a}_{lj} \left(\mathbf{I} - \Pi \right) \left(v \partial_{x} g^{n,(j)} \right) - \frac{\Delta t}{\varepsilon^{2}} \sum_{j=1}^{l} a_{lj} \left(g^{n,(j)} + v \partial_{x} \rho^{n,(j)} \right), \ l = 1, \cdots, s.$$

$$(5.15c)$$

Note that the summation in the implicit part is from j = 1 instead of j = 0. It implies that the update in the inner stages, related to the implicit part of the IMEX-RK methods, does not explicitly depend on the solution from the previous RK step. This is due to the ARS structure and plays an important role in the presence of the initial layer.

When the initial data is not well-prepared, a modification is proposed to the first two steps in Section 3.1. To examine the asymptotic behavior of the methods, two cases will be considered next. We will write $R^n = g^n + v\partial_x \rho^n$, and $R^{n,(l)} = g^{n,(l)} + v\partial_x \rho^{n,(l)}$.

Case 1: the initial is well-prepared with $R^0 = O(\varepsilon)$. The IMEXp scheme will lead to the updates of $\rho^{n+1}, g^{n+1}, R^{n+1}$, together with $\rho^{n,(l)}, g^{n,(l)}, R^{n,(l)}$ as follows.

$$\rho^{n+1} = \rho^{n,(s)}, \quad g^{n+1} = g^{n,(s)}, \quad R^{n+1} = R^{n,(s)},$$
(5.16)

where the inner stages are updated according to

$$\rho^{n,(0)} = \rho^n, \quad g^{n,(0)} = g^n, \quad R^{n,(0)} = R^n,$$
(5.17a)

$$\rho^{n,(l)} = \rho^{n} + \Delta t a_{ll} \left(\langle v^{2} \rangle \partial_{xx} \rho^{n,(l)} \right) - \Delta t \sum_{j=0}^{l-1} \tilde{a}_{lj} \partial_{x} \langle v R^{n,(j)} \rangle + \Delta t \sum_{j=1}^{l-1} a_{lj} \left(\langle v^{2} \rangle \partial_{xx} \rho^{n,(j)} \right), \quad l = 1, \cdots, s,$$

$$(5.17b)$$

$$g^{n,(l)} = \frac{\varepsilon^2 g^n - \Delta t a_{ll} v \partial_x \rho^{n,(l)}}{\varepsilon^2 + a_{ll} \Delta t} - \frac{\varepsilon \Delta t}{\varepsilon^2 + a_{ll} \Delta t} \sum_{i=0}^{l-1} \tilde{a}_{lj} \left(\mathbf{I} - \Pi \right) \left(v \partial_x g^{n,(j)} \right)$$

$$-\frac{\Delta t}{\varepsilon^2 + a_{ll}\Delta t} \sum_{j=1}^{l-1} a_{lj} R^{n,(j)}, \quad l = 1, \dots, s,$$
(5.17c)

$$R^{n,(l)} = \frac{\varepsilon^2}{\varepsilon^2 + a_{ll}\Delta t} \left(g^n + v\partial_x \rho^{n,(l)} \right) - \frac{\varepsilon \Delta t}{\varepsilon^2 + a_{ll}\Delta t} \sum_{j=0}^{l-1} \tilde{a}_{lj} \left(\mathbf{I} - \Pi \right) \left(v\partial_x g^{n,(j)} \right) - \frac{\Delta t}{\varepsilon^2 + a_{ll}\Delta t} \sum_{j=1}^{l-1} a_{lj} R^{n,(j)}, \quad l = 1, \dots, s.$$

$$(5.17d)$$

With $\varepsilon \ll 1$, we have

- $\rho^{n,(l)}, g^{n,(l)} = O(1), \partial_x \rho^{n,(l)}, \partial_{xx} \rho^{n,(l)}, \partial_x g^{n,(l)} = O(1), l = 0, \dots, s, \forall n \ge 0.$
- $R^n = O(\varepsilon)$, $R^{n,(l)} = O(\varepsilon)$, $\partial_x \langle vR^{n,(l)} \rangle = O(\varepsilon)$, $\forall n \geq 0, l = 0, \dots, s$. That is, the numerical solutions from both inner stages and full RK steps stay within the $O(\varepsilon)$ -width neighborhood of the local equilibrium.
- ρ^n satisfies

$$\rho^{n+1} = \rho^{n,(s)}, \quad \text{where} \quad \rho^{n,(l)} = \rho^n + \Delta t \sum_{j=1}^l a_{lj} \left(\langle v^2 \rangle \partial_{xx} \rho^{n,(j)} \right) + O(\varepsilon), \quad l = 1, \dots, s, \quad \forall n \ge 0.$$

Hence the limiting scheme for ρ^n as $\varepsilon \to 0$ is a consistent scheme of p-th order temporal accuracy for the limiting heat equation, and more specifically, the scheme involves the implicit part of ARS(s,s,p) in time with the asymptotically consistent initial data. Additionally, the computed solution satisfies the local equilibrium property at the full RK steps and at all inner stages. This shows the IMEXp scheme is AP.

Case 2: the initial is not well-prepared with $R^0 = O(\varepsilon^{-1})$. The IMEXp scheme will lead to the updates of ρ^{n+1} , g^{n+1} , R^{n+1} as well as $\rho^{n,(l)}$, $g^{n,(l)}$, $R^{n,(l)}$, $\forall n \geq 2$, just as in (5.16)-(5.17) except that in step 1 with n = 0, the update in (3.2) is used with the time step $\Delta t_1 = \Delta t^p$, and in step 2 with n = 1, the update (5.16)-(5.17) is used with the time step $\Delta t_2 = \Delta t^p$. Then with $\varepsilon \ll 1$, the modified scheme leads to

- $\rho^n, g^n, \rho^{n,(l)}, g^{n,(l)} = O(1), \ \partial_x \rho^{n,(l)}, \partial_{xx} \rho^{n,(l)}, \partial_x g^{n,(l)} = O(1), \ \forall n \geq 1, l = 0, \dots, s, \text{ even though } \rho^0 = O(1), q^0 = O(\varepsilon^{-1}).$
- $R^n = O(\varepsilon), R^{n,(l)} = O(\varepsilon), \partial_x \langle vR^{n,(l)} \rangle = O(\varepsilon), \forall n \geq 2, l = 0, \dots, s$, while $R^0 = O(\varepsilon^{-1}), R^1 = R^{1,(0)} = O(1), \partial_x \langle vR^1 \rangle = O(1)$, and $R^{1,(l)} = O(\varepsilon), \partial_x \langle vR^{1,(l)} \rangle = O(\varepsilon), l = 1, \dots, s$.
- ρ^n satisfies

$$\rho^{n+1} = \rho^{n,(s)}, \quad \text{where} \quad \rho^{n,(l)} = \rho^n + \Delta t \sum_{j=1}^l a_{lj} \left(\langle v^2 \rangle \partial_{xx} \rho^{n,(j)} \right) + O(\varepsilon), \quad l = 1, \dots, s, \quad \forall n \ge 2,$$

while at n = 0,

$$\rho^{1} = \rho^{0} + \Delta t_{1} \langle v^{2} \rangle \partial_{xx} \rho^{0} + O(\Delta t_{1}), \quad \text{with } \Delta t_{1} = \Delta t^{p}.$$
 (5.18)

And at n=1, $\rho^2=\rho^{1,(s)}$ where

$$\rho^{1,(l)} = \rho^{1} + \Delta t_{2} \sum_{j=1}^{l} a_{lj} \left(\langle v^{2} \rangle \partial_{xx} \rho^{n,(j)} \right) - \Delta t_{2} \tilde{a}_{l0} \partial_{x} \langle vR^{1} \rangle + O(\varepsilon)$$

$$= \rho^{1} + \Delta t_{2} \sum_{j=1}^{l} a_{lj} \left(\langle v^{2} \rangle \partial_{xx} \rho^{n,(j)} \right) + O(\Delta t_{2}) + O(\varepsilon), \ l = 1, \dots, s, \text{ with } \Delta t_{2} = \Delta t^{p}.$$

$$(5.19)$$

In the limit of $\varepsilon \to 0$, the local error to ρ^1 in Case 2 is of first order in $\Delta t_1 = \Delta t^p$ hence of p-th order in Δt . In the second step to computer ρ^2 , the scheme can be regarded as a perturbed method to an otherwise p-th order temporal discretization. Given that each inner stage solution $\rho^{1,(l)}$ is perturbed by an error proportional to Δt_2 , ρ^2 will be of first order in Δt_2 , hence the choice of the step size $\Delta t_2 = \Delta t^p$ ensures that ρ^2 is a p-th order approximation. When $n \ge 2$, the scheme has similar behavior as in Case 1. Therefore we can conclude when $\varepsilon \to 0$, the limiting scheme is a consistent scheme with the p-th order accuracy. This shows the IMEXp scheme is AP even in the presence of the initial layer.

Remark 5.2. Consider the diffusive regime with $\varepsilon \ll 1$. When the initial data is not well-prepared with the presence of the initial layer, the modification for n=0 based on (3.2) will drive the numerical solution to be bounded with respect to ε after the first step, yet the solution by then is only within the O(1)-width neighborhood of the local equilibrium. The second

step based on (5.16)-(5.17) further drives the numerical solution to fall into the $O(\varepsilon)$ -width neighborhood of the local equilibrium. Our scheme in each of the first two time steps will lead to a first order error to the solution at the full RK steps. Such first order error is with respect to the time step size, and it can be reduced to the desired accuracy by taking $\Delta t_1 = \Delta t_2 = \Delta t^p$, where Δt is the time step size for later steps, predicted by stability analysis.

Remark 5.3. Similar to Remark 5.1, a more refined analysis can be carried out for the accuracy of the IMEXp scheme, which is summarized in Table 5.1. From this table, one can see that only for the worst scenario, namely when R^0 , $\langle vR^0 \rangle = O(\varepsilon^{-1})$, the proposed modification is needed to gain full accuracy. For other moderate cases, such as when $R^0 = O(\varepsilon^{-1})$ with $\langle vR^0 \rangle = O(\varepsilon)$, O(1), or when $R^0 = O(1)$ with $\langle vR^0 \rangle = O(1)$, one can gain the full temporal accuracy by using the base IMEXp scheme with a modified step size in the initial one or two steps, without the need for the scheme (3.2).

Remark 5.4. In Case 2, the property that $R^{1,(0)} = O(1)$ while $R^{1,(l)} = O(\varepsilon)$, $l = 1, \dots, s$ is due to that the update in (5.17d) does not depend on $R^{n,(0)}$. This feature is due to the IMEX-RK method being of type ARS.

Remark 5.5. In actual simulation, it is possible that $\varepsilon^2 \ll \Delta t$, yet the modified step size $\Delta t_1, \Delta t_2 \ (= \Delta t^p)$ is smaller than the initial layer width. In this case, more than one modified time step would be needed for the solution to exit the initial layer to ensure full accuracy.

6 Numerical examples

In this section, we will present a set of numerical examples to illustrate the performance of the proposed schemes in terms of their accuracy and robustness, when the underlying models involve different values of ε in different regimes with smooth or non-smooth solutions. When the initial data is not well-prepared, we also demonstrate the effectiveness of the proposed strategies to avoid the order reduction and inaccuracy of the numerical solutions. Two weight functions will be considered, and they are $\omega=1$ and $\omega=\exp(-\varepsilon/h)$. The schemes with $\omega=1$ are referred to as the IMEXp-LDGp methods, while the schemes with $\omega=\exp(-\varepsilon/h)$ are referred to as IMEXp-LDGp- $\mathcal M$ methods. Recall that in IMEXp-LDGp and IMEXp-LDGp- $\mathcal M$ methods, the discrete space U_h^{p-1} is used in space. The numerical results by the schemes with $\omega=\exp(-\varepsilon^2/\Delta t)$ are qualitatively similar to those by the schemes with $\omega=\exp(-\varepsilon/h)$, and they are not presented here.

Based on the stability analysis in Section 4, we observe that the methods, when applied to the model equation (1.1), are unconditionally stable when $\varepsilon/h \leq R_{p,\omega}$ for some constant $R_{p,\omega} > 0$; when $\varepsilon/h > R_{p,\omega}$, the methods are stable under the condition

$$\frac{\Delta t}{\varepsilon h} \le \mathcal{G}_{p,\omega}(\frac{\varepsilon}{h}) \tag{6.1}$$

for some function $\mathcal{G}_{p,\omega}$. In an ongoing project, we also carry out an energy-type stability analysis for the IMEX1-LDG1 scheme, and the analysis suggests a specific form of $\mathcal{G}_{p,\omega}(s)$, namely, $\mathcal{G}_{p,\omega}(s) = \frac{\alpha_p s}{\beta_p s-1}$. This form of $\mathcal{G}_{p,\omega}(s)$ seems to also fit what we numerically observed through Fourier-type stability analysis for other IMEXp-LDG $p(-\mathcal{M})$ methods. Motivated by this, for our numerical experiments in this section, we take $\mathcal{G}_{p,\omega}(s) = \frac{\alpha_p s}{\beta_p s-1}$, with the parameters α_p and β_p chosen based on the stability plots in Section 4. Particularly when the boundary conditions are periodic, the time step size is set as $\Delta t = \Delta t_{CFLp}$ for IMEXp-LDGp and $\Delta t = \Delta t_{CFLp\mathcal{M}}$ for IMEXp-LDGp- \mathcal{M} , where

IMEX1-LDG1:
$$\Delta t_{CFL1} = \begin{cases} 0.25h, & \varepsilon \le h/4, \\ \min(0.25h, \frac{4\varepsilon^2 h}{4s-h}), & \varepsilon > h/4, \end{cases}$$
 (6.2a)

IMEX1-LDG1:
$$\Delta t_{CFL1} = \begin{cases} 0.25h, & \varepsilon \le h/4, \\ \min(0.25h, \frac{4\varepsilon^2 h}{4\varepsilon - h}), & \varepsilon > h/4, \end{cases}$$
 (6.2a)

IMEX2-LDG2: $\Delta t_{CFL2} = \begin{cases} 0.25h, & \varepsilon \le h/251, \\ \min(0.25h, \frac{62.75\varepsilon^2 h}{251\varepsilon - h}), & h/251 < \varepsilon < 5h/2, \\ 0.625h^2, & \varepsilon \ge 5h/2 \end{cases}$

IMEX3-LDG3: $\Delta t_{CFL3} = \begin{cases} 0.25h, & \varepsilon \le h/30, \\ \min(0.25h, \frac{4.5\varepsilon^2 h}{30\varepsilon - h}), & \varepsilon > h/30. \end{cases}$ (6.2c)

IMEX3-LDG3:
$$\Delta t_{CFL3} = \begin{cases} 0.25h, & \varepsilon \le h/30, \\ \min(0.25h, \frac{4.5\varepsilon^2 h}{30\varepsilon - h}), & \varepsilon > h/30. \end{cases}$$
 (6.2c)

IMEX1-LDG1-
$$\mathcal{M}$$
: $\Delta t_{CFL1\mathcal{M}} = \begin{cases} 0.25h, & \varepsilon \le h/4, \\ \min(0.25h, \frac{3\varepsilon^2 h}{6\varepsilon - h}), & \varepsilon > h/4, \end{cases}$ (6.2d)

IMEX2-LDG2-
$$\mathcal{M}$$
: $\Delta t_{CFL2\mathcal{M}} = \begin{cases} 0.25h, & \varepsilon \leq h/251, \\ \min(0.25h, \frac{62.75\varepsilon^2 h}{251\varepsilon - h}), & \varepsilon > h/251, \end{cases}$

$$IMEX3-LDG3-\mathcal{M}: \Delta t_{CFL3\mathcal{M}} = \begin{cases} 0.25h, & \varepsilon \leq h/35, \\ \min(0.25h, \frac{4.375\varepsilon^2 h}{35\varepsilon - h}), & \varepsilon > h/35. \end{cases}$$

$$(6.2e)$$

IMEX3-LDG3-
$$\mathcal{M}$$
: $\Delta t_{CFL3\mathcal{M}} = \begin{cases} 0.25h, & \varepsilon \le h/35, \\ \min(0.25h, \frac{4.375\varepsilon^2 h}{35\varepsilon - h}), & \varepsilon > h/35. \end{cases}$ (6.2f)

Note that an O(h) upper bound is imposed to the time step size to ensure reasonable resolution of the numerical solutions. As implied by the stability analysis in Section 4, a parabolic time step condition is needed for the IMEX2-LDG2 method in the kinetic regime. When the boundary conditions are not periodic, time step sizes may need to be adjusted due to the numerical boundary treatments. This will be specified when we come to those examples. In all figures in this section, the reference solutions are always plotted in solid lines.

With the IMEX temporal discretization, linear systems need to be solved for each time step. Fortunately, the implicit part of our schemes with the global nature comes from the discretization of a Poisson operator, the corresponding linear system is hence symmetric and positive definite when the boundary conditions are periodic. For such examples, Conjugate Gradient method is used as the linear solver. In the case of Dirichlet boundary conditions (see Section 6.2 and Remark 6.1), symmetry will be broken, and Conjugate Gradient Squared method will be applied instead. Even though not explored in this work, one can apply standard fast solver techniques for elliptic equations, such as multigrid methods, to efficiently solve the linear systems resulting from the proposed methods.

6.1Telegraph equation

Two examples will be presented for the telegraph equation which involves discrete velocity. The meshes are uniform. We use the left-right flux pair alternating flux (3.11).

6.1.1Smooth solution with periodic boundary conditions

First, we consider an example with the following exact solution

$$\begin{cases} \rho(x,t) &= \frac{1}{\gamma} \exp(\gamma t) \sin(x), \qquad \gamma = \frac{-2}{1+\sqrt{1-4\varepsilon^2}}, \\ g(x,v=\pm 1,t) &= \pm \exp(\gamma t) \cos(x) \end{cases}$$

on the domain $\Omega_x = [-\pi, \pi]$ with periodic boundary conditions. We carry out the convergence study for the IMEXp-LDGp and IMEXp-LDGp- \mathcal{M} methods (with p=1,2,3) in different regimes with $\varepsilon = 0.5, 10^{-2}$ and 10^{-6} . The errors in the normalized L^1 norm (namely, normalized with respect to the domain size) and convergence orders for $\rho(x,t)$ and $j(x,t)=\langle vg\rangle=\frac{1}{2}(g(x,v))$ 1,t)-g(x,v=-1,t)) are shown in Tables 6.2-6.4 at time T=1.0. For both ρ and j, we observe the optimal p-th order convergence for all three schemes in all regimes, implying an optimal accuracy with respect to the approximation property of the discrete space U_h^{p-1} . As expected, the error obtained with two different weights differ in the kinetic regime and have the same leading digits in the diffusive regime. In the intermediate regime, the IMEX1-LDG1 and IMEX1-LDG1- \mathcal{M} methods give quite different errors, while for p=2,3, the errors obtained by IMEXp-LDGp and IMEXp-LDGp- \mathcal{M} methods have the same leading digits.

Table 6.2: L^1 errors and orders for the example in Section 6.1.1, IMEX1-LDG1(- \mathcal{M})

ε	N		IMEX1	-LDG1	I	IMEX1-LDG1- \mathcal{M}				
-	1 V	L^1 error of ρ	order	L^1 error of j	order	L^1 error of ρ	order	L^1 error of j	order	
	10	3.781E-02	-	4.824E-02	-	3.629E-02	-	5.128E-02	-	
	20	1.763E-02	1.10	2.585E-02	0.90	1.623E-02	1.16	2.732E-02	0.91	
0.5	40	7.956E-03	1.15	1.334E-02	0.95	7.507E-03	1.11	1.392E-02	0.97	
	80	3.699E-03	1.11	6.742 E-03	0.98	3.617E-03	1.05	6.988E-03	0.99	
	160	1.773 E-03	1.06	3.380E-03	1.00	1.778E-03	1.02	3.496E-03	1.00	
	320	8.664E-04	1.03	1.691E-03	1.00	8.817E-04	1.01	1.748E-03	1.00	
	10	7.001E-02	-	9.516E-02	-	4.472E-02	-	7.900E-02	-	
	20	3.875 E-02	0.85	5.187E-02	0.88	2.169E-02	1.04	3.885E-02	1.02	
10^{-2}	40	2.011E-02	0.95	2.640E-02	0.97	1.057E-02	1.04	1.929E-02	1.01	
	80	1.036E-02	0.96	1.342E-02	0.98	5.113E-03	1.05	9.537E-03	1.02	
	160	3.588E-03	1.53	5.461E-03	1.30	2.196E-03	1.22	4.599E-03	1.05	
	320	1.108E-03	1.70	2.300E- 03	1.25	1.094E-03	1.00	2.299E-03	1.04	
	10	4.460E-02	-	7.907E-02	-	4.460E-02	-	7.907E-02	-	
	20	2.180E-02	1.03	3.895E-02	1.02	2.180E-02	1.03	3.895E-02	1.02	
10^{-6}	40	1.078E-02	1.02	1.946E-02	1.00	1.078E-02	1.02	1.946E-02	1.00	
	80	5.356E-03	1.01	9.702 E-03	1.00	5.356E-03	1.01	9.702E-03	1.00	
	160	2.668E-03	1.01	4.843E-03	1.00	2.668E-03	1.01	4.843E-03	1.00	
	320	1.331E-03	1.00	2.419E-03	1.00	1.331E-03	1.00	2.419E-03	1.00	

Table 6.3: L^1 errors and orders for the example in Section 6.1.1, IMEX2-LDG2(- \mathcal{M})

ε	N		IMEX2	2-LDG2	IMEX2-LDG2- $\mathcal M$				
8	1 V	L^1 error of ρ	order	L^1 error of j	order	L^1 error of ρ	order	L^1 error of j	order
	10	1.944E-03	-	9.887E-004	-	1.965E-003	-	9.223E-04	-
	20	4.667E-04	2.06	2.185E-04	2.18	4.567E-04	2.11	1.850E-04	2.32
0.5	40	1.155E-04	2.01	4.831E-05	2.18	1.128E-04	2.02	4.162E-05	2.15
	80	2.821E-05	2.03	1.046E-05	2.21	2.789E-05	2.02	9.751E-06	2.09
	160	6.974 E-06	2.02	2.451E-06	2.09	6.928E-06	2.01	2.396E-06	2.02
	320	1.733E-06	2.01	5.941E-07	2.04	1.730E-06	2.00	5.984E-07	2.00
	10	6.524E-03	-	1.861E-03	-	6.524E-03	-	1.861E-03	-
	20	1.616E-03	2.01	4.376E-04	2.09	1.616E-03	2.01	4.376E-04	2.09
10^{-2}	40	4.031E-04	2.03	1.047E-04	2.06	4.031E-04	2.00	1.047E-04	2.06
	80	1.007E-04	2.00	2.561E-05	2.03	1.007E-04	2.00	2.561E-05	2.03
	160	2.518E-05	2.00	6.336E-06	2.02	2.518E-05	2.00	6.336E-06	2.02
	320	6.294E-06	2.00	1.576E-06	2.01	6.294E-06	2.00	1.576E-06	2.01
	10	6.605E-03	-	1.860E-03	-	6.605E-03	-	1.860E-03	-
	20	1.630E-03	2.02	4.417E-04	2.07	1.630E-03	2.02	4.417E-04	2.07
10^{-6}	40	4.065E-04	2.00	1.069E-04	2.05	4.065E-04	2.00	1.069E-04	2.05
	80	1.016E-04	2.00	2.642 E-05	2.02	1.016E-04	2.00	2.642E-05	2.02
	160	2.539E-05	2.00	6.582 E-06	2.01	2.539E-05	2.00	6.582E-06	2.01
	320	6.346E-06	2.00	1.644E-06	2.00	6.346E-06	2.00	1.644E-06	2.00

Table 6.4: L^1 errors and orders for the example in Section 6.1.1, IMEX3-LDG3(- \mathcal{M})

ε	N		IMEX3	3-LDG3	Ι	MEX3-I	$\overline{\mathrm{DG3-}\mathcal{M}}$		
٤ ا	1 V	L^1 error of ρ	order	L^1 error of j	order	L^1 error of ρ	order	L^1 error of j	order
	10	6.780E-05	-	1.125E-04	-	6.223E-05	-	9.885E-05	-
	20	9.617E-06	2.82	8.386E-06	3.75	8.831E-06	2.82	1.918E-05	2.37
0.5	40	1.183E-06	3.02	4.172 E-06	1.01	8.901E-07	3.32	1.960E-06	3.29
	80	1.177E-07	3.33	6.258 E-07	2.74	1.552 E-07	2.52	5.958E-07	1.72
	160	1.413E-08	3.06	7.121E-08	3.14	2.339E-08	2.73	1.815E-08	5.04
	320	1.929E-09	2.87	1.067E-08	2.74	1.844E-09	3.67	6.854E-09	1.41
	640	2.258E-10	3.09	1.881E-09	2.50	2.998E-10	2.69	3.904E-10	4.13
	10	2.491E-04	-	2.473E-04	-	2.491E-04	-	2.473E-04	-
	20	3.139E-05	2.99	3.127E-05	2.98	3.139E-05	2.99	3.127E-05	2.98
10^{-2}	40	3.901E-06	3.01	3.902 E-06	3.00	3.901E-06	3.01	3.902 E-06	3.00
	80	4.873E-07	3.00	4.874E-07	3.00	4.873E-07	3.00	4.874E-07	3.00
	160	6.090E-08	3.00	6.091E- 08	3.00	6.090E-08	3.00	6.091E-08	3.00
	320	7.613E-09	3.00	7.613E-09	3.00	7.613E-09	3.00	7.613E-09	3.00
	10	2.485E-04	-	2.546E-04	-	2.485E-04	-	2.546E-04	-
	20	3.139E-05	2.99	3.139E-05	3.02	3.139E-05	2.99	3.139E-05	3.02
10^{-6}	40	3.910E-06	3.00	3.911E-06	3.01	3.910E-06	3.00	3.911E-06	3.01
	80	4.892E-07	3.00	4.892 E-07	3.00	4.892 E-07	3.00	4.892E-07	3.00
	160	6.114E-08	3.00	6.114E-08	3.00	6.114E-08	3.00	6.114E-08	3.00
	320	7.641E-09	3.00	7.641E-09	3.00	7.641E-09	3.00	7.641E-09	3.00

6.1.2 Riemann problem

The second example for the telegraph equation is a Riemann problem, with the initial conditions

$$\begin{cases} \rho(x,0) = \rho_L = 2.0, & g(x,v,0) = g_L = 0, & \text{for } x \le 0, \\ \rho(x,0) = \rho_R = 1.0, & g(x,v,0) = g_R = 0, & \text{for } x > 0, \end{cases}$$
(6.3)

and $\varepsilon=0.7,\,10^{-6}.$ Without loss of generality, we use a mesh satisfying $x_{k_0+\frac{1}{2}}=0$, for some $k_0\in\mathbb{N}.$

When $\varepsilon=0.7$, the computational domain is taken as $\Omega_x=[-1,1]$ with the final time T=0.15. In Figure 6.4, we present the numerical results by IMEXp-LDGp- \mathcal{M} methods with h=0.025 and p=1,2,3. No nonlinear limiter is applied. The results by the lowest order IMEX1-LDG1- \mathcal{M} method are most dissipative, while the results by IMEXp-LDGp- \mathcal{M} methods with p=2,3 are much sharper. As no limiter is applied, some mild oscillations are observed around discontinuities in the results by the IMEXp-LDGp- \mathcal{M} methods with p=2,3.

In Figure 6.5, we present the numerical results of the IMEXp-LDGp methods with h=0.025 and p=1,2,3. In order to control numerical oscillations, the TVB-minmod limiter in [9] with M=1 is applied to ρ , g and q for the IMEXp-LDGp methods with p=2,3, and the time step size is also adjusted to be smaller. More specifically, we take $0.025\Delta t_{CFL1}$ for the IMEX1-LDG1 method, $0.5\Delta t_{CFL2}$ for the IMEX2-LDG2 method, and $0.125\Delta t_{CFL3}$ for the IMEX3-LDG3 method. One can see the IMEXp-LDGp methods with p=2,3 outperform the IMEX1-LDG1 method. The results by the IMEX2-LDG2 method match the reference solutions the best (note that the time step size of this method is $O(h^2)$ for this example). The use of nonlinear limiter still leave visible oscillations to the results by the IMEXp-LDGp (p=2,3) methods.

Even though the IMEXp-LDGp- \mathcal{M} methods use larger time step sizes without a nonlinear limiter, they overall perform better than the IMEXp-LDGp schemes for this Riemann problem when $\varepsilon = 0.7$. We attribute this to the auxiliary unknown, $q = \partial_x \rho$, that contains a Dirac- δ singularity in this Riemann problem. The singularity in q imposes challenge to the IMEX-LDG

methods with the weight function $\omega = 1$ in the kinetic regime. For the IMEX-LDG- \mathcal{M} methods, the weight function $w = \exp(-\varepsilon/h)|_{\varepsilon=0.7, h=0.025} \approx 10^{-13}$, and it significantly reduces the impact of the singularity in q. Actually, in this regime, the IMEX-LDG- \mathcal{M} schemes are very close to the DG-IMEX schemes in [15] (which are also the proposed methods here with the weight $\omega = 0$).

When $\varepsilon = 10^{-6}$, the computational domain is taken as $\Omega_x = [-2, 2]$ with the final time T = 0.15. The solutions are smooth around this time, and no limiter is needed. Still with h = 0.025, the numerical solutions are shown in Figure 6.6. The results obtained by the IMEXp-LDGp schemes and IMEXp-LDGp- \mathcal{M} schemes have no visible difference. Hence, only the results of the IMEXp-LDGp- \mathcal{M} schemes are presented with p = 1, 2, 3. All methods capture the solutions well, and higher order methods show better resolution.

6.2 One group transport equation in slab geometry

In this section, we will consider the one-group transport equation in slab geometry in a more general form [23], namely,

$$\varepsilon \partial_t f + v \partial_x f = \frac{\sigma_s}{\varepsilon} (\langle f \rangle - f) - \varepsilon \sigma_A f + \varepsilon G$$
(6.4)

on $\Omega_x = [x_L, x_R]$ and with a continuous velocity space $\Omega_v = [-1, 1]$. The parameter $\sigma_s = \sigma_s(x)$ is the scattering coefficient, which is assumed to be positive, the non-negative $\sigma_A = \sigma_A(x)$ is the absorption coefficient, and G = G(x) is the source term. Following the derivation in Section 2, one can get the micro-macro reformulation

$$\partial_t \rho + \partial_x \langle vg \rangle = -\sigma_A \rho + G,$$

$$\partial_t g + \frac{1}{\varepsilon} (\mathbf{I} - \Pi) (v \partial_x g) + \frac{1}{\varepsilon^2} v \partial_x \rho = -\frac{\sigma_s}{\varepsilon^2} g - \sigma_A g.$$
(6.5)

When $\varepsilon \to 0$, the limiting equation (at least away from the initial and boundary) is

$$g = -v\partial_x \rho/\sigma_s, \quad \partial_t \rho = \langle v^2 \rangle \partial_x (\partial_x \rho/\sigma_s) - \sigma_A \rho + G.$$
 (6.6)

The proposed IMEX-LDG methods can be extended directly to (6.4) based on the following reformulated form of the model:

$$\partial_t \rho + \partial_x \langle v(g + \omega vq/\sigma_s) \rangle = \omega \langle v^2 \rangle \partial_x (q/\sigma_s) - \sigma_A \rho + G, \qquad q = \partial_x \rho,$$
 (6.7a)

$$\partial_t g + \frac{1}{\varepsilon} (\mathbf{I} - \Pi)(v \partial_x g) + \frac{1}{\varepsilon^2} v \partial_x \rho = -\frac{\sigma_s}{\varepsilon^2} g - \sigma_A g.$$
 (6.7b)

In addition to periodic boundary conditions, some numerical examples in this section involve Dirichlet boundary conditions, that are given at the inflow boundaries of the domain $\Omega_x = [x_L, x_R]$, in the form of

$$f(x_L, v, t) = f_L(v, t), \quad v > 0,$$
 and $f(x_R, v, t) = f_R(v, t), \quad v < 0.$

They are insufficient to define $\rho = \langle f \rangle$ (resp. g and q) at the boundary within the micro-macro decomposition framework. In this case, numerical boundary treatments are needed to complete the proposed methods. Next we will present two strategies, which will be described when $\sigma_s = 1$ and $\sigma_A = 0$, and can be easily given to the cases with more general σ_s and σ_A . We will first present assumptions for boundary conditions and then impose boundary conditions through numerical fluxes.

1.) Limiting boundary condition. The first boundary treatment is based on the limiting equation as $\varepsilon \to 0$. Similar strategy was used in [5, 17] within an even-odd decomposition framework. As $\varepsilon \to 0$, the limiting equation gives

$$g = -v\partial_x \rho = -vq$$
, with $q = \partial_x \rho$. (6.8)

We assume this relation at the boundary, then the given boundary conditions become

$$\rho_L(t) - \varepsilon v q_L(t) = f_L(v, t), \quad v \ge 0$$
 and $\rho_R(t) - \varepsilon v q_R(t) = f_R(v, t), \quad v \le 0.$

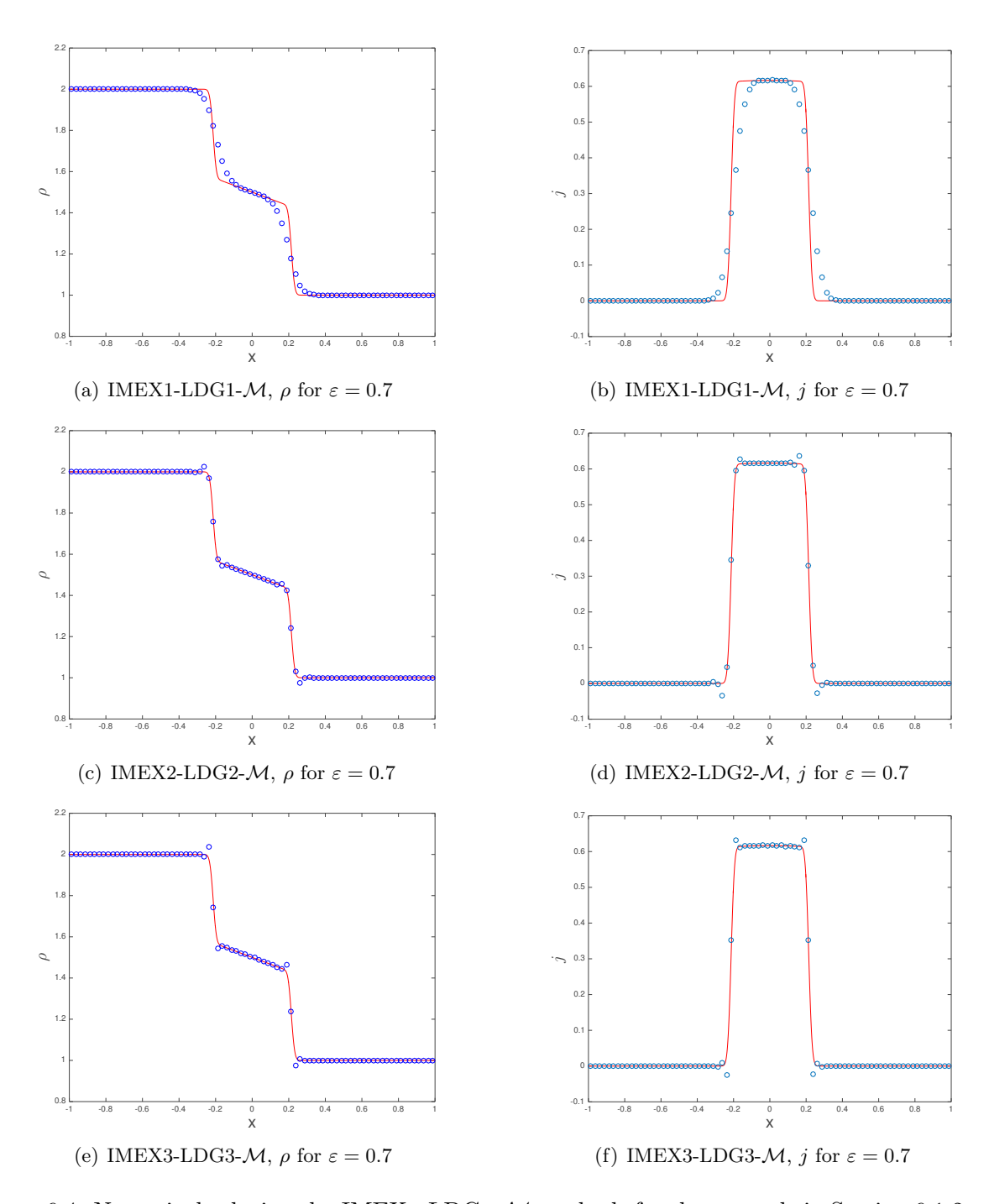


Figure 6.4: Numerical solutions by IMEX*p*-LDG*p*- \mathcal{M} methods for the example in Section 6.1.2 with $\varepsilon=0.7$ at T=0.15. The reference solution is obtained by the first order forward Euler upwind finite difference scheme, with $h=10^{-3}$ and $\Delta t=7\times 10^{-4}$. No limiter is applied.

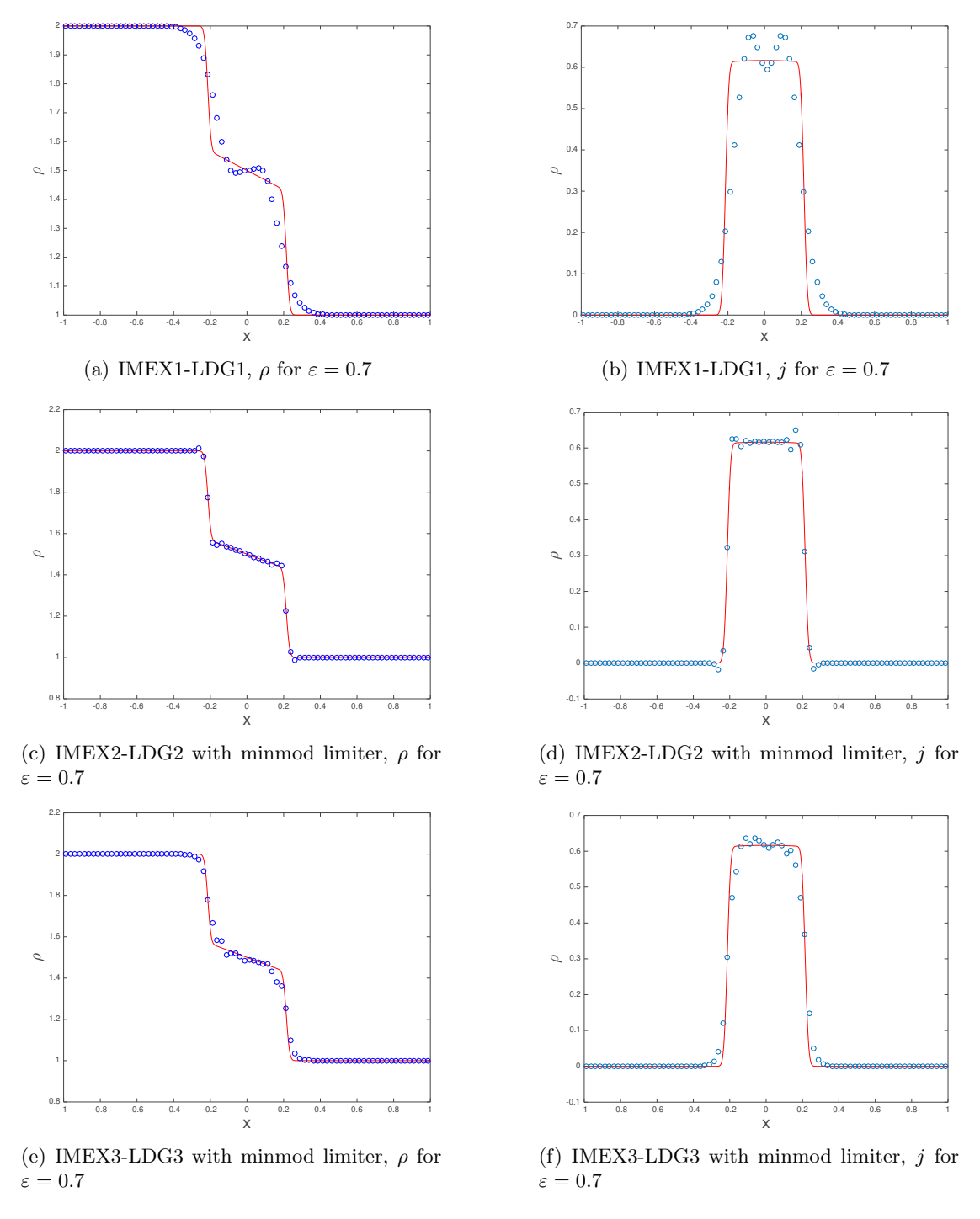


Figure 6.5: Numerical solutions by IMEX*p*-LDG*p* methods for the example in Section 6.1.2 with $\varepsilon = 0.7$ at T = 0.15. The reference solution is obtained by the first order forward Euler upwind finite difference scheme, with $h = 10^{-3}$ and $\Delta t = 7 \times 10^{-4}$. The minmod limiter with M = 1 is used when p = 2, 3.

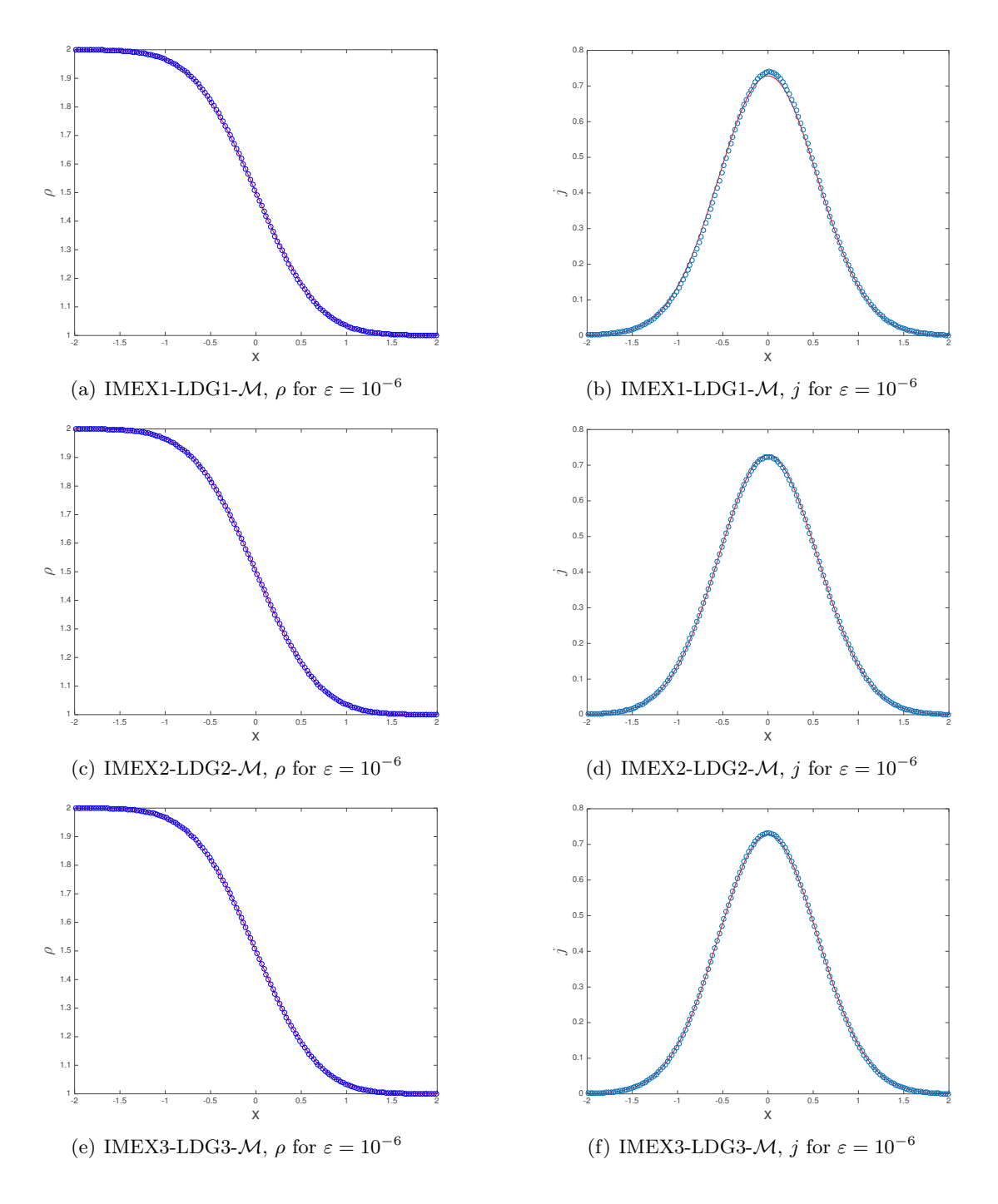


Figure 6.6: Numerical solutions by IMEX*p*-LDG*p*- \mathcal{M} methods for the example in Section 6.1.2 with $\varepsilon=10^{-6}$ at T=0.15. The reference solution is obtained by solving the limiting diffusion equation using the forward Euler with second order central difference scheme, with $h=10^{-3}$ and $\Delta t=2.5\times 10^{-7}$.

We further integrate the first equality in v from 0 to 1 at the left boundary, and integrate the second equality in v from -1 to 0 at the right boundary. This gives

$$\rho_L(t) - \varepsilon \frac{1}{2} q_L(t) = \int_0^1 f_L(v, t) dv, \qquad \rho_R(t) + \varepsilon \frac{1}{2} q_R(t) = \int_{-1}^0 f_R(v, t) dv. \tag{6.9}$$

Motivated by this, the following numerical boundary treatment is proposed.

• We specify numerical fluxes $\check{\rho}$ and \widetilde{vg} at both boundaries:

$$\check{\rho}_{\frac{1}{2}}^{n} = \int_{0}^{1} f_{L}(v, t_{n}) dv + \frac{1}{2} \varepsilon q^{n}(x_{\frac{1}{2}}^{+}) : \triangleq \rho_{L}^{n}, \quad (\widetilde{vg^{n}})_{\frac{1}{2}} = vg^{n}(x_{\frac{1}{2}}^{+}),
\check{\rho}_{N+\frac{1}{2}}^{n} = \int_{0}^{1} f_{R}(v, t_{n}) dv - \frac{1}{2} \varepsilon q^{n}(x_{N+\frac{1}{2}}^{-}) : \triangleq \rho_{R}^{n}, \quad (\widetilde{vg^{n}})_{N+\frac{1}{2}} = vg^{n}(x_{N+\frac{1}{2}}^{-}).$$
(6.10)

• We modify the equation (3.7b) into the following

$$\left(\frac{\rho_h^{n+1} - \rho_h^n}{\Delta t}, \phi\right) + l_h^{\dagger}(\langle vg_h^n \rangle, \phi) + \omega \langle v^2 \rangle l_h(q_h^n, \phi) = \omega \langle v^2 \rangle l_h(q_h^{n+1}, \phi), \quad \forall \phi \in U_h^k$$
 (6.11)

where $l_h(\cdot,\cdot)$ is just as before in (3.8b), with the numerical flux modified at the boundary, namely.

$$\widehat{q}_{\frac{1}{2}}^{n} = q^{n}(x_{\frac{1}{2}}^{+}) + c_{L} \left(\rho^{n}(x_{\frac{1}{2}}^{+}) - \rho_{L}^{n}\right), \quad \widehat{q}_{N+\frac{1}{2}}^{n} = q^{n}(x_{N+\frac{1}{2}}^{-}) - c_{R} \left(\rho_{R}^{n} - \rho^{n}(x_{N+\frac{1}{2}}^{-})\right);$$

while

$$l_h^{\dagger}(\langle vg_h^n\rangle,\phi) = -\sum_i \int_{I_i} \langle vg_h^n\rangle \partial_x \phi dx - \sum_i \widehat{\langle vg_h^n\rangle}_{i-\frac{1}{2}} [\phi]_{i-\frac{1}{2}}, \tag{6.12}$$

and $\widehat{\langle vg_h^n\rangle}_{i-\frac{1}{2}}=\widehat{\langle vg_h^n\rangle}_{i-\frac{1}{2}}, \forall i=2,3,\cdots,N-1$ for interior nodes, and

$$\widehat{\overline{\langle vg^n\rangle}_{\frac{1}{2}}} = \langle vg^n\rangle(x_{\frac{1}{2}}^+), \quad \widehat{\overline{\langle vg^n\rangle}_{N+\frac{1}{2}}} = \langle vg^n\rangle(x_{N+\frac{1}{2}}^-)$$

at boundaries.

One can see that the numerical boundary treatments are essentially imposed through numerical fluxes. The two parameters c_L and c_R are non-negative, and they are used to facilitate the inclusion of some jump terms c_L ($\rho^n(x_{\frac{1}{2}}^+) - \rho_L^n$) and c_R ($\rho_R^n - \rho^n(x_{N+\frac{1}{2}}^-)$) at the domain boundary to ensure the full accuracy of the overall algorithm when alternating fluxes are used at the interior nodes. More specifically, when the right-left alternating flux in (3.11) is used in our scheme, we take $c_L = 1$ and $c_R = 0$, while with the left-right alternating flux, we take $c_L = 0$ and $c_R = 1$. One can refer to [8, 24] to better understand the role of these jump terms in relation to the accuracy of the schemes.

2.) Inflow-outflow close-loop boundary condition. Using the solution inside the domain to provide the outflow boundary data, we get a close-loop strategy similar to that in [15]. For the left boundary, we require the following relations:

$$\rho_L(t) + \varepsilon g_L(v, t) = f_L(v, t), \quad v \ge 0 \quad \text{(inflow)}, \tag{6.13a}$$

$$\rho_L(t) + \varepsilon g_L(v, t) = \rho_h(x_{\underline{1}}^+, t) + \varepsilon g_h(x_{\underline{1}}^+, v, t), \quad v \le 0 \quad \text{(outflow)},$$
(6.13b)

$$\langle q_L(v,t)\rangle = 0.$$
 (6.13c)

We integrate (6.13a) in v from 0 to 1, and integrate (6.13b) in v from -1 to 0. Summing up the resulting equations and with (6.13c), one can express the boundary data ρ_L in terms of the known f_L and the unknown interior solution, and further get g_L from (6.13a)-(6.13b), hence $\langle vg_L(v,t)\rangle$. This leads to, at $t=t^n$,

$$\rho_L^n : \triangleq \rho_L(t^n) = \frac{1}{2} \left(\int_0^1 f_L(v, t^n) dv + \rho_h^n(x_{\frac{1}{2}}^+) + \varepsilon \int_{-1}^0 g_h^n(x_{\frac{1}{2}}^+, v) dv \right), \tag{6.14a}$$

$$g_L^n(v) : \triangleq g_L(v, t^n) = \begin{cases} \frac{1}{\varepsilon} \left(f_L(v, t^n) - \rho_L(t^n) \right), & v > 0, \\ \frac{1}{\varepsilon} \left(\rho_h^n(x_{\frac{1}{2}}^+) + \varepsilon g_h^n(x_{\frac{1}{2}}^+, v) - \rho_L(t^n) \right), & v \le 0. \end{cases}$$
(6.14b)

Similarly, for the right boundary we can get

$$\rho_R^n : \triangleq \rho_R(t^n) = \frac{1}{2} \left(\int_{-1}^0 f_R(v, t^n) dv + \rho_h^n(x_{N+\frac{1}{2}}^-) + \varepsilon \int_0^1 g_h^n(x_{N+\frac{1}{2}}^-, v) dv \right), \tag{6.15a}$$

$$g_R^n(v) : \triangleq g_R(v, t^n) = \begin{cases} \frac{1}{\varepsilon} \left(\rho_h^n(x_{N + \frac{1}{2}}^-) + \varepsilon g_h^n(x_{N + \frac{1}{2}}^-, v) - \rho_R(t^n) \right), \ v \ge 0, \\ \frac{1}{\varepsilon} \left(f_R(v, t^n) - \rho_R(t^n) \right), \ v < 0. \end{cases}$$
(6.15b)

Based on the relations above, we propose a numerical treatment for boundary conditions, again by working with the modified equation (6.11) and l_h^{\dagger} in (6.12) and specifying the numerical fluxes on the domain boundary as follows,

$$\tilde{\rho}_{\frac{1}{2}}^{n} = \rho_{L}^{n}, \quad \widehat{q}_{\frac{1}{2}}^{n} = q^{n}(x_{\frac{1}{2}}^{+}) + c_{L} \left(\rho^{n}(x_{\frac{1}{2}}^{+}) - \rho_{L}^{n}\right), \quad \widehat{\langle vg^{n} \rangle}_{\frac{1}{2}} = \langle vg_{L}^{n}(v) \rangle, \tag{6.16a}$$

$$\widetilde{\rho}_{N+\frac{1}{2}}^{n} = \rho_{R}^{n}, \quad \widehat{q}_{N+\frac{1}{2}}^{n} = q^{n}(x_{N+\frac{1}{2}}^{-}) + c_{R}\left(\rho_{R}^{n} - \rho^{n}(x_{N+\frac{1}{2}}^{-}), \widehat{\langle vg^{n}\rangle}_{N+\frac{1}{2}} = \langle vg_{R}^{n}(v)\rangle, \qquad (6.16b)$$

and

$$\widetilde{(vg^n)}_{\frac{1}{2}} = \begin{cases} vg_L^n(v), & \text{if } v > 0, \\ vg_h^n(x_{\frac{1}{2}}^+, v), & \text{if } v \le 0, \end{cases} \qquad \widetilde{(vg^n)}_{N+\frac{1}{2}} = \begin{cases} vg_h^n(x_{N+\frac{1}{2}}^-, v), & \text{if } v \ge 0, \\ vg_R^n(v), & \text{if } v < 0. \end{cases}$$
(6.17)

The jump terms for q in (6.16) are for the same accuracy consideration as in the limiting boundary condition strategy, with the constants c_L and c_R taken similarly as well.

Remark 6.1. In our numerical experiments, we use the limiting boundary conditions for the diffusive regime, and the inflow-outflow close-loop boundary conditions for the kinetic regime. For the diffusive regime, it is observed that using the inflow-outflow close-loop boundary conditions may require a stringent time step condition, namely, $\Delta t = O(h^2)$, for numerical stability, while using the limiting boundary conditions will keep the unconditional stability of the proposed scheme. For the intermediate regime, the choice will be example-dependent. With either numerical boundary treatment above, the symmetry of the resulting linear system to update ρ_h^{n+1} will no longer hold.

Remark 6.2. For those examples in Section 6 with Dirichlet boundary conditions, we only consider the isotropic ones, that is, when f_L and f_R are independent of v. When f_L and f_R are anisotropic and depend on v, the solutions can develop boundary layers. Such cases however can not be handled effectively by our proposed boundary treatments. In [22], the boundary layer issue was addressed for a finite difference scheme, which is based on a different micro-macro decomposition of the governing equation, together with the use of some extra unknown variable near domain boundary.

In our simulations, the velocity space Ω_v is discretized using 16-point Gaussian quadrature, and the operator $\langle \cdot \rangle$ is replaced by its numerical analogue. The results are obtained with the left-right flux pair alternating flux (3.11). And the meshes are uniform unless otherwise specified.

6.2.1 Smooth example with periodic boundary conditions

With $\sigma_A = G = 0$, $\sigma_s = 1$, we consider a smooth example with the initial conditions

$$\rho(x,0) = \sin(x), \qquad g(x,v,0) = -v\cos(x)$$

on the domain $\Omega_x = [-\pi, \pi]$ with periodic boundary conditions. We carry out the numerical simulations for different regimes with $\varepsilon = 0.5$, 10^{-2} and 10^{-6} . The final time is T = 1.0. The convergence order of the schemes is calculated by Richardson extrapolation:

order =
$$RE_N = \log_2 (||u_h - u_{h/2}||_{L_1(\Omega_x)} / ||u_{h/2} - u_{h/4}||_{L_1(\Omega_x)})$$
.

Here u_h is the numerical solution computed with a mesh size $\frac{h}{2} = \frac{x_R - x_L}{N}$. And the numerical error is computed as $R_N = ||u_h - u_{h/2}||_{L_1(\Omega_x)}/|\Omega_x|$.

The numerical errors and convergence orders of ρ and $j = \langle vg \rangle$ are shown in Tables 6.5-6.7 for the IMEXp-LDGp and IMEXp-LDGp- \mathcal{M} schemes with p = 1, 2, 3. The optimal p-th order of convergence is observed for all the schemes in all regimes. When p = 2, 3, the schemes with the two different weights do not lead to much difference in numerical errors in all regimes.

					_			`	,
ε	N		IMEX1	-LDG1		IMEX1-LDG1- <i>M</i>			
٤	1 V	R_N for ρ	order	R_N for j	order	R_N for ρ	order	R_N for j	order
	10	1.454E-01	-	9.771E-03	-	6.466E-02	-	1.036E-02	-
	20	3.367E-02	1.09	5.434E-03	0.85	3.154E-02	1.04	5.613E-03	0.88
0.5	40	1.661E-02	1.02	2.809E-03	0.95	1.588E-02	0.99	2.859E-03	0.97
	80	8.233E-03	1.01	1.423E-03	0.98	8.013E-03	0.99	1.439E-03	0.99
	160	4.101E-03	1.01	7.159E-04	0.99	4.024E-03	0.99	7.212E-04	1.00
	10	7.092E-02	-	1.053E-02	-	7.085E-02	-	1.053E-02	-
	20	3.600E-02	0.98	5.340E-03	0.98	3.597E-02	0.98	5.341E-03	0.98
10^{-2}	40	1.795E-02	1.00	2.677E-03	1.00	1.793E-02	1.00	2.677E-03	1.00
	80	8.969E-03	1.00	1.339E-03	1.00	8.953E-03	1.00	1.339E-03	1.00
	160	4.513E-03	0.99	6.703E-04	1.00	4.478E-03	1.00	6.689E-04	1.00
	10	7.084E-02	-	1.055E-02	-	7.084E-02	-	1.055E-02	-
	20	3.600E-02	0.98	5.344E-03	0.98	3.600E-02	0.98	5.344E-03	0.98
10^{-6}	40	1.795E-02	1.00	2.678E-03	1.00	1.795E-02	1.00	2.678E-03	1.00
	80	8.963E-03	1.00	1.339E-03	1.00	8.963E-03	1.00	1.339E-03	1.00
1	1	l .	1	I .	1	1	1	I .	I .

Table 6.5: L^1 errors and orders for the example in Section 6.2.1, IMEX1-LDG1(- \mathcal{M})

6.2.2 Diffusive and kinetic regimes with isotropic boundary conditions

6.692E-04

4.482E-03

1.00

We here consider an example from [5, 23] with isotropic Dirichlet boundary conditions together with zero initial condition, namely

1.00

4.482E-03

1.00

6.692E-04

1.00

$$f_L(v,t) = 1, \quad f_R(v,t) = 0; \quad f(x,v,0) = 0, \quad x \in \Omega_x;$$

 $\sigma_s = 1, \quad \sigma_A = 0, \quad G = 0.$

The computational domain is $\Omega_x = [0,1]$, with $\varepsilon = 10^{-4}$ for the diffusive regime and $\varepsilon = 1$ for the kinetic regime. For the numerical boundary treatments, we apply the inflow-outflow close-loop boundary conditions for $\varepsilon = 1$ and the limiting boundary conditions for $\varepsilon = 10^{-4}$. The spatial meshsize is taken to be h = 1/40.

Note that the initial and boundary data on the left boundary are not compatible, and this will lead to a Dirac- δ type singularity in $q = \partial_x \rho$. In the kinetic regime with $\varepsilon = 1$, this example will impose similar numerical challenge to the methods with $\omega = 1$ as the Riemann problem in Section 6.1.2. Related to this, when $\varepsilon = 1$, $0.25\Delta t_{CFL1}$ is used for the IMEX1-LDG1 scheme while $0.125\Delta t_{CFL3}$ is used for the IMEX3-LDG3 scheme, in order to get reasonable numerical solutions.

In Figure 6.7, we plot the computed density ρ . More specifically, the top two rows are for the kinetic regime with $\varepsilon=1$ by the IMEXp-LDGp (in the first row) and IMEXp-LDGp- \mathcal{M} (in the second row) methods, with p=1,2,3. In each plot, the computed ρ at times T=0.1, 0.4, 1.0, 1.6 and 4.0 are presented. It is observed that higher order methods capture more details, and additionally, the IMEXp-LDGp- \mathcal{M} scheme outperforms the respective IMEXp-LDGp scheme when p=1,3. Even though $q=\partial_x\rho$ contains singularity due to the incompatible initial and boundary data, with the weight $\omega=\exp(-\varepsilon/h)|_{\varepsilon=1,h=1/40}\approx 10^{-18}$, the ωq term has negligible contribution to the IMEXp-LDGp schemes. In this regime, the IMEX-LDG schemes are very

Table 6.6: L^1 errors and orders for the example in Section 6.2.1, IMEX2-LDG2(- \mathcal{M})

ε	N		IMEX2	2-LDG2		IMEX2-LDG2- ${\cal M}$			
2	1 V	R_N for ρ	order	R_N for j	order	R_N for ρ	order	R_N for j	order
	10	2.270E-02	-	1.482E-02	-	2.269E-02	-	1.479E-02	-
	20	5.677E-03	2.00	3.822E-03	1.96	5.676E-03	2.00	3.806E-03	1.96
0.5	40	1.403E-03	2.00	9.524E-04	2.00	1.404E-03	2.02	9.476E-04	2.01
	80	3.484E-04	2.01	2.377E-04	2.00	3.483E-04	2.01	2.367E-04	2.00
	160	8.678E-05	2.01	5.937E-05	2.00	8.677E-05	2.01	5.915E-05	2.00
	10	2.265E-02	-	1.462E-02	-	2.265E-02	-	1.462E-02	-
	20	5.637E-03	2.01	3.773E-03	1.95	5.637E-03	2.01	3.773E-03	1.95
10^{-2}	40	1.408E-03	2.00	9.393E-04	2.01	1.408E-03	2.00	9.393E-04	2.01
	80	3.518E-04	2.00	2.346E-04	2.00	3.518E-04	2.00	2.346E-04	2.00
	160	8.794E-05	2.00	5.863E-05	2.00	8.794E-05	2.00	5.863E-05	2.00
	10	2.262E-02	-	1.467E-02	-	2.262E-02	-	1.467E-02	-
	20	5.624E-03	2.01	3.765E-03	1.95	5.624E-03	2.01	3.765E-03	1.95
10^{-6}	40	1.404E-03	2.00	9.372E-04	2.01	1.404E-03	2.00	9.372E-04	2.01
	80	3.510E-04	2.00	2.340E-04	2.00	3.510E-04	2.00	2.340E-04	2.00
	160	8.774E-05	2.00	5.849E-05	2.00	8.774E-05	2.00	5.849E-05	2.00

Table 6.7: L^1 errors and orders for the example in Section 6.2.1, IMEX3-LDG3(- \mathcal{M})

ε	$\mid_{N}\mid$		IMEX3	-LDG3		IMEX3-LDG3- \mathcal{M}			
٤	1 V	R_N for ρ	order	R_N for j	order	R_N for ρ	order	R_N for j	order
	10	1.670E-03	-	1.449E-04	-	1.674E-03	-	1.448E-04	-
	20	2.069E-04	3.01	1.805E-05	3.01	2.065E-04	3.02	1.797E-05	3.01
0.5	40	2.560E-05	3.01	2.258E-06	3.00	2.561E-05	3.01	2.250E-06	3.00
	80	3.206E-06	3.00	2.845E-07	2.99	3.206E-06	3.00	2.834E-07	2.99
	160	4.014E-07	3.00	3.580E-08	2.99	4.013E-07	3.00	3.566E-08	2.99
	10	1.621E-03	-	1.253E-04	-	1.621E-03	-	1.253E-04	-
	20	2.071E-04	2.97	1.558E-05	3.01	2.071E-04	2.97	1.558E-05	3.01
10^{-2}	40	2.581E-05	3.00	1.958E-06	2.99	2.581E-05	3.00	1.958E-06	2.99
	80	3.223E-06	3.00	2.487E-07	2.98	3.223E-06	3.00	2.487E-07	2.98
	160	4.029E-07	3.00	3.183E-08	2.97	4.029E-07	3.00	3.183E-08	2.97
	10	1.619E-03	-	1.248E-04	-	1.619E-03	-	1.248E-04	-
	20	2.070E-04	2.97	1.545E-05	3.01	2.070E-04	2.97	1.545E-05	3.01
10^{-6}	40	2.581E-05	3.00	1.927E-06	3.00	2.581E-05	3.00	1.927E-06	3.00
	80	3.224E-06	3.00	2.407E-07	3.00	3.224E-06	3.00	2.407E-07	3.00
	160	4.029E-07	3.00	3.009E-08	3.00	4.029E-07	3.00	3.009E-08	3.00

closed to the DG-IMEX schemes in [15]. For p=2, the methods with two weights produce comparable results. Again recall that the parabolic type time step condition $\Delta t = O(h^2)$ is used for the IMEX2-LDG2 scheme.

When $\varepsilon = 10^{-4}$, the problem is in its diffusive regime and numerical results by the methods with the two weights have no visible difference. In the third row of Figure 6.7, we plot the computed ρ by the IMEXp-LDGp schemes (with p=1,2,3) at T=0.05,0.15 and 2.0. It is observed that higher order methods have better resolution. We want to mention that if the inflow-outflow close-loop boundary condition is applied, the IMEXp-LDGp method is unconditionally stable with p=1,2, while the IMEX3-LDG3 requires $\Delta t = O(h^2)$ for stability (see Remark 6.1).

6.2.3 Intermediate regime with isotropic boundary conditions, varying scattering frequency, and source term

Here we consider an example with isotropic Dirichlet boundary conditions and a constant source, and the scattering coefficient $\sigma_s(x)$ is spatially varying [23]:

$$f_L(v,t) = 0$$
, $f_R(v,t) = 0$, $f(x,v,0) = 0$, $\sigma_s(x) = 1 + (10x)^2$, $\sigma_A = 0$, $G = 1$

on $\Omega_x = [0,1]$ and $\varepsilon = 10^{-2}$. The effective Knudsen number is $\frac{\varepsilon}{\sigma_s(x)}$ at the spatial location x. We want to use this example to demonstrate how our methods work in the presence of spatially varying scales.

For the IMEXp-LDGp- \mathcal{M} schemes, the weight function is taken to be

$$\omega = \exp(-\frac{\varepsilon}{h\bar{\sigma}_s}),$$

where $\bar{\sigma}_s$ is the average of $\sigma_s(x)$ over the spatial domain, namely, $\bar{\sigma}_s = \frac{1}{|\Omega_x|} \int_{\Omega_x} \sigma_s(x) dx$. When the schemes are conditionally stable, the time step conditions are adjusted. Particularly, we use $0.7\Delta t_{CFL3}$ for the IMEX3-LDG3 scheme and $0.75\Delta t_{CFL3\mathcal{M}}$ for the IMEX3-LDG3- \mathcal{M} . No adjustment is needed for other schemes. To impose the boundary conditions numerically, we apply the limiting boundary conditions.

In Figure 6.8, the numerical solutions for ρ are plotted at T=0.4 with h=0.025. Since the two weights do not lead to visible difference, we only present the results by the IMEXp-LDGp- \mathcal{M} methods with p=1,2,3. Due to the spatial variation of the scattering coefficient, there is a sharp feature near the right boundary in space. Overall high order schemes with p=2,3 have better resolution.

6.2.4 Two-material problem

The example we will consider here involve two different materials [23, 15],

$$\begin{split} &\sigma_s = 0, \quad \sigma_A = 1, \quad G = 0, \quad \text{for} \quad x \in \Omega_{x,L} = [0,1], \\ &\sigma_s = 100, \quad \sigma_A = 0, \quad G = 0, \quad \text{for} \quad x \in \Omega_{x,R} = [1,11], \\ &f_L(v,t) = 5, \quad f_R(v,t) = 0; \quad f(x,v,0) = 0, \quad x \in \Omega_x, \end{split}$$

with $\Omega_x = \Omega_{x,L} \cup \Omega_{x,R}$. Following [21, 23], the parameter ε is set to be 1, meaning that the dimensional variables are used here. And the system consists of a purely absorbing slab region $\Omega_{x,L}$ of one mean-free path length, connected to a purely scattering slab region $\Omega_{x,R}$ of a thousand mean-free path length that is more diffusive over long time observation. We want to use this example to demonstrate our proposed methods applied to such problems in the presence of multiple scales. An isotropic configuration of f is introduced to the purely absorbing region $\Omega_{x,L}$ from the left boundary, and it will attenuate and become anisotropic (that is, v dependent) before entering the purely scattering region $\Omega_{x,R}$. An interior layer will arise between the absorbing and scattering regions. In our simulation, a non-uniform mesh is used, with the mesh size h = 0.05 in $\Omega_{x,L}$ and h = 0.5 in $\Omega_{x,R}$. We apply the inflow-outflow close-loop numerical boundary conditions, and the left-right numerical fluxes in (3.11) are used for the interior points.

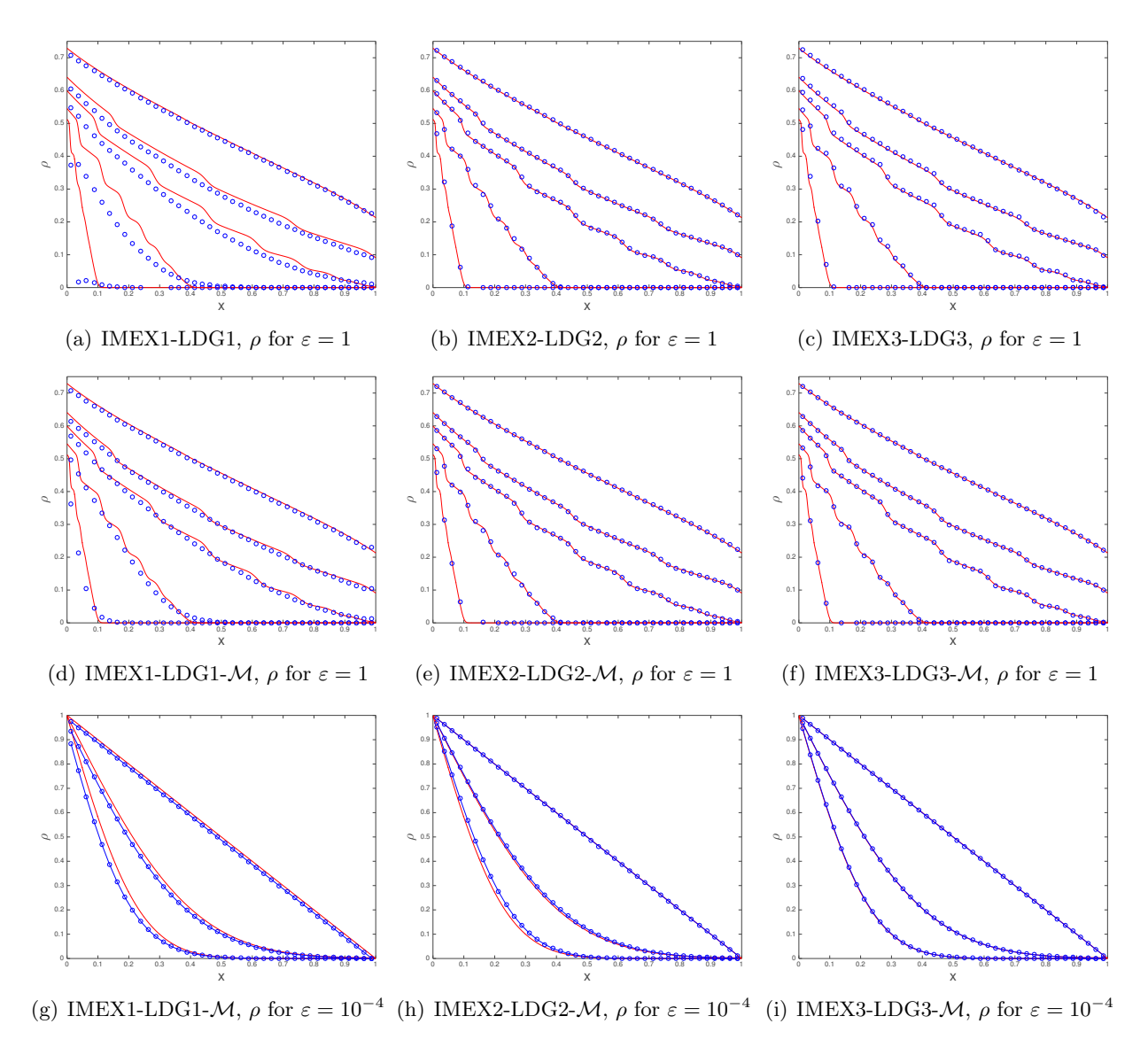


Figure 6.7: The numerical density ρ for the problem in Section 6.2.2. Top row: the results of IMEXp-LDGp schemes in the kinetic regime with $\varepsilon = 1$ at T = 0.1, 0.4, 1.0, 1.6 and 4.0. Middle row: the results of IMEXp-LDGp- \mathcal{M} schemes in the kinetic regime with $\varepsilon = 1$ at T = 0.1, 0.4, 1.0, 1.6 and 4.0. The reference solutions for the first two rows are obtained by the first order forward Euler upwind finite difference scheme, with $h = 5 \times 10^{-4}$ and $\Delta t = 2.5 \times 10^{-5}$. Bottom row: the results of IMEXp-LDGp- \mathcal{M} schemes in the diffusive regime with $\varepsilon = 10^{-4}$ at T = 0.05, 0.15, and 2.0. The reference solution for the bottom row is computed by the DG1-IMEX1 scheme in [14], with $h = 10^{-3}$ and $\Delta t = 10^{-6}$. From left to right: p = 1, 2, 3.

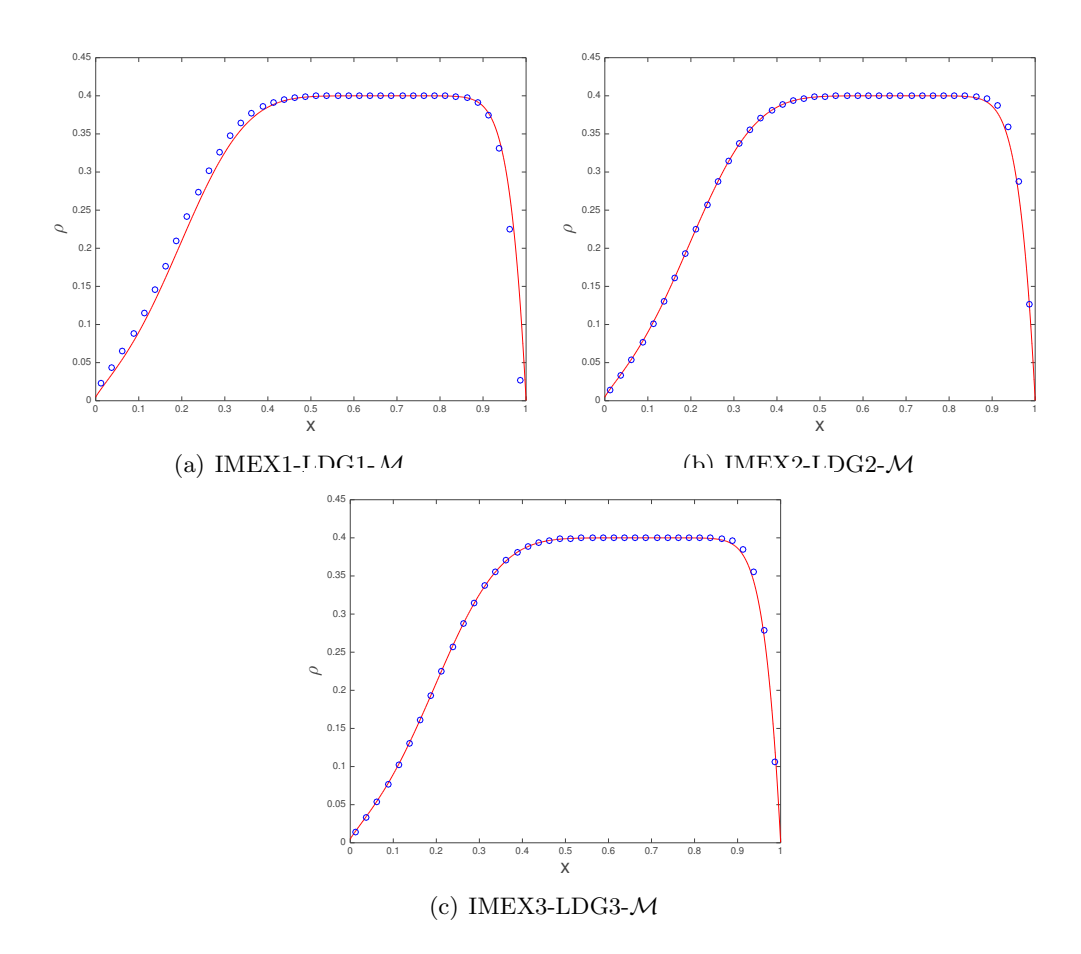


Figure 6.8: The numerical density ρ for the problem in Section 6.2.3 at T=0.4. The reference solution is obtained by the first order forward Euler upwind finite difference scheme, with $h=5\times 10^{-5}$ and $\Delta t=1.25\times 10^{-7}$ for $\varepsilon=10^{-2}$.

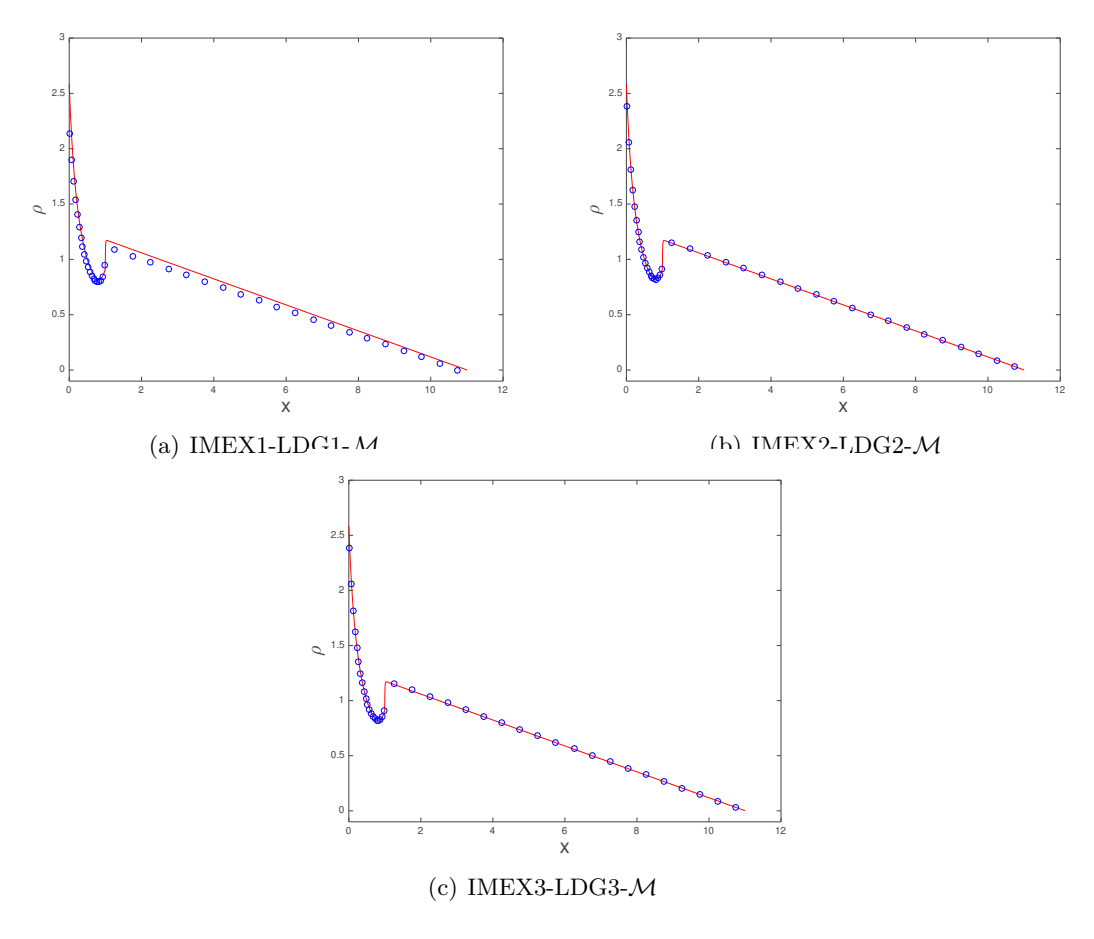


Figure 6.9: The computed steady-state density ρ for the problem in Section 6.2.4 at T=20000. The reference solution is obtained by the first order forward Euler upwind finite difference scheme, with $h=5.5\times 10^{-3}$ and $\Delta t=10^{-4}$.

For this example, even though there is a purely absorbing subregion $\Omega_{x,L}$, we choose to use the weight function $\omega = \exp(-\varepsilon/(100h))$ for the IMEXp-LDGp- \mathcal{M} schemes. This choice is based on the scattering coefficient $\sigma_s = 100$ in the purely scattering subregion $\Omega_{x,R}$. We examine the steady state solution by running the simulation over a long time, and the computed solutions for density ρ are presented in Figure 6.9 at T = 20000. Visually, the results of IMEXp-LDGp and IMEXp-LDGp- \mathcal{M} coincide with each other. Only the results of IMEXp-LDGp- \mathcal{M} are shown with p = 1, 2, 3. All the schemes match the reference solution well. The higher order the scheme is, the better resolution it has.

6.3 Examples with non well-prepared initial data

Finally we consider two examples with non well-prepared initial data in order to demonstrate the effectiveness of the proposed initial fixing strategies for accuracy in the presence of the initial layer. Example 1 starts with $f(x, v, 0) = (1 + (v - 0.5)^2)(1 + 0.05\cos(x))$, while Example 2 has $f(x, v, 0) = (1 + \varepsilon(v - 0.5)^2)(1 + 0.05\cos(x))$. They both have $\rho(x, 0) = 1 + 0.05\cos(x)$ and $g(x, v, 0) = O(\varepsilon^{-1})$. The computational domain is $\Omega_x = [0, 2\pi]$ with periodic boundary conditions. The final time is T = 1.0 and $\varepsilon = 10^{-6}$.

Note that $\langle vf(x,v,0)\rangle = 0$ for Example 1, implying $\langle vR^0\rangle = O(1)$, and $\langle vf(x,v,0)\rangle \neq 0$ for Example 2, implying $\langle vR^0\rangle = O(\varepsilon^{-1})$ according to (5.6). As predicted by the asymptotic analysis (also see Table 5.1), without any initial treatment, the IMEX*p*-LDG*p*(- \mathcal{M}) scheme will be first order accurate for Example 1 and inaccurate for Example 2. And with the initial fixing strategies we have proposed, the full accuracy of order *p* will be achieved. This is confirmed by the results in Table 6.8 and Figure 6.10 before the fix, and by the full order of accuracy in Table

6.9 after the fixing strategies are applied. Since the weight function $\omega = \exp(-\varepsilon/h)$ is very close to 1, the leading digits of the errors obtained by IMEX*p*-LDG*p* and IMEX*p*-LDG*p*- \mathcal{M} are the same. Only the results of the IMEX*p*-LDG*p*- \mathcal{M} methods (with p=1,2,3) are shown in error tables. Given that the errors and orders are computed based on Richardson extrapolation, we also plot the numerical solutions with the fixing strategies and the reference solutions in Figure 6.10 for Example 2 to make sure the correct solutions are captured numerically.

Table 6.8: L^1 errors and orders by the IMEX*p*-LDG*p*- \mathcal{M} schemes for Example 1 in Section 6.3, $\varepsilon = 10^{-6}$, T = 1, without any initial fixing strategy

scheme	N	R_N for ρ	order	R_N for j	order
	10	4.264E-03	-	5.049E-04	-
	20	2.115E-03	1.01	2.519E-04	1.00
p = 1	40	1.064E-04	0.99	1.245E-04	1.02
	80	5.309E-04	1.00	6.199E-05	1.01
	160	2.652E-04	1.00	3.091E-05	1.00
	10	8.290E-04	-	9.376E-04	-
	20	4.768E-04	0.80	3.629E-04	1.37
p=2	40	2.641E-04	0.85	1.815E-05	1.00
	80	1.402E-04	0.91	9.410E-05	0.95
	160	7.232E-05	0.96	4.829E-05	0.96
	10	1.745E-04	-	1.883E-04	-
	20	9.763E-05	0.84	7.476E-05	1.33
p=3	40	5.138E-05	0.93	3.546E-05	1.08
_	80	2.614E-05	0.97	1.758E-05	1.01
	160	1.315E-05	0.99	8.783E-05	1.00

7 Conclusions

In this paper, we design and analyze high order methods based on discontinuous Galerkin spatial discretizations and implicit-explicit Runge-Kutta temporal discretizations for linear kinetic transport equations in a diffusive scaling. With Fourier type stability analysis, the methods are shown to be unconditionally stable in the diffusive regime $\varepsilon \ll 1$, and can have hyperbolic type stability condition $\Delta t = O(\varepsilon h)$ in the kinetic regime $\varepsilon = O(1)$. The design of the methods takes into account the initial layer which may be present in the solutions, and in particular when the initial data is not well-prepared, initial fixing strategies are proposed in the first one or two time steps to overcome the possible accuracy reduction or loss for $\varepsilon \ll 1$. The overall schemes are shown to be asymptotically preserving, namely the methods in the limit of the $\varepsilon \to 0$ are consistent and high order discretizations for the limiting diffusive equation with the asymptotically consistent initial condition. In an ongoing project, an energy-based numerical stability will be performed, together with the error estimates as well as a rigorous asymptotic analysis.

The proposed methods are based on a reformulated form of the underlying model, by adding and subtracting a weighted diffusion term. Even though such idea is not new, our analysis provides mathematical understanding about the desired properties (not all known previously) of the weight function. One can refer to Theorem 4.1 and Theorem 4.3 that suggest how the weight function depends on the model and discretization parameters $\varepsilon, h, \Delta t$, and one can also see equations (2.6) and (5.13) for the desired properties on the magnitude of the weight function to ensure the AP property. On the algebraic level, the implicit part that needs to be solved globally comes from a discrete Poisson operator. The methods in this work can be combined with fast computation techniques for scattering operators to simulate physically more relevant kinetic transport models involving multiple scales. Some other issues that are not addressed here include positivity preserving technique and boundary layer treatments.

Table 6.9: L^1 errors and orders by the IMEXp-LDGp- \mathcal{M} schemes for Examples 1 and 2 in Section 6.3, $\varepsilon = 10^{-6}$, T = 1.0 with initial fixing strategy

			Exan	ple 1		Example 2				
scheme	N	R_N for ρ	order	R_N for j	order	R_N for ρ	order	R_N for j	order	
	10					2.587E-03	-	5.760E-04	-	
	20	Full accu	racy is	achieved with	hout	1.583E-03	0.71	2.789E-04	1.05	
p=1	40		fixing s	trategy		8.589E-04	0.88	1.374E-04	1.02	
	80					4.462E-04	0.94	6.807E-05	1.01	
	160					2.271E-04	0.97	3.387E-05	1.01	
	10	1.144E-03	-	8.299E-04	-	1.049E-03	-	8.372E-04	-	
	20	2.815E-04	2.02	1.884E-04	2.14	2.474E-04	2.08	1.657E-04	2.34	
p=2	40	7.024E-04	2.00	4.687E-05	2.01	6.154E-05	2.01	4.108E-05	2.01	
	80	1.755E-05	2.00	1.170E-05	2.00	1.536E-05	2.00	1.025E-05	2.00	
	160	4.387E-06	2.00	2.925E-06	2.00	3.840E-06	2.00	2.560E-06	2.00	
	10	8.381E-05	-	5.375E-05	-	7.864E-05	-	5.367E-05	-	
	20	1.035E-05	3.02	6.896E-06	2.96	1.046E-05	2.92	6.965E-06	2.95	
p=3	40	1.290E-06	3.00	8.601E-07	3.00	1.332E-06	2.97	8.877E-07	2.97	
	80	1.612E-07	3.00	1.074E-07	3.00	1.681E-07	2.99	1.121E-07	2.99	
	160	2.014E-08	3.00	1.343E-08	3.00	1.955E-08	3.10	1.522E-08	2.88	

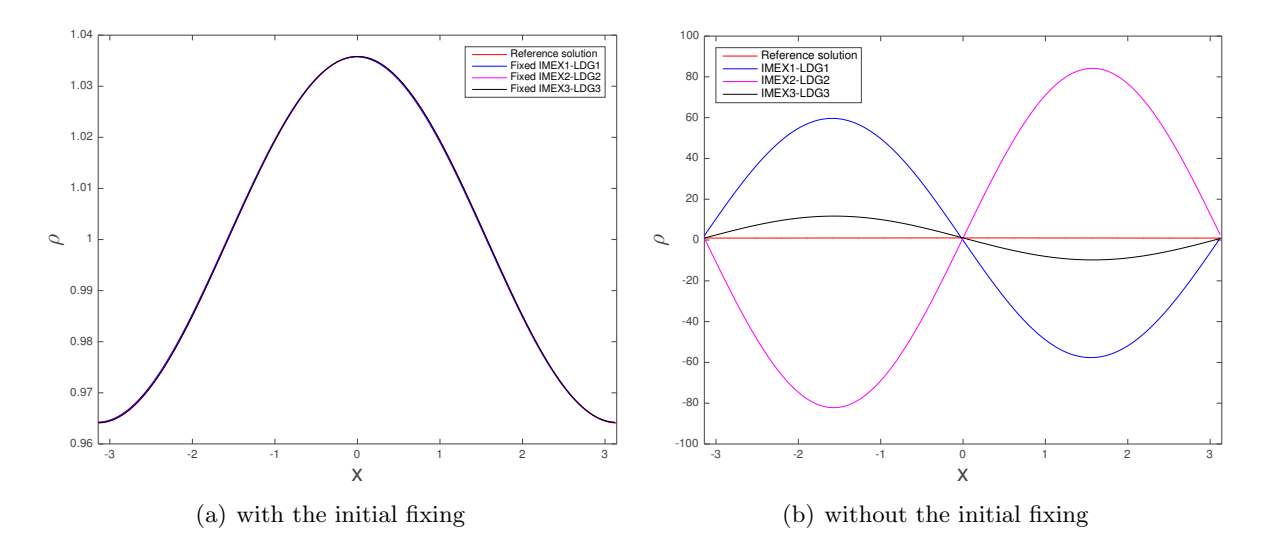


Figure 6.10: The numerical density ρ computed by the IMEXp-LDGp- \mathcal{M} methods with (left) and without (right) the initial fixing strategy for Example 2 in Section 6.3. Here $\varepsilon=10^{-6},\,T=1.0,\,N=320$. Reference solutions are computed by the forward Euler central difference scheme solving the limiting diffusion equation with N=2000.

Appendix A AP methods with a different implicit-explicit strategy: accuracy reduction

In order for us to achieve AP methods with high order accuracy for a broad range of ε , it seems important that the numerical solutions stay sufficiently close to the local equilibrium in the diffusive regime, namely, $g^n + v\partial_x \rho^n = O(\varepsilon)$. This property is guaranteed by our proposed implicit-explicit strategy (at least for $n \geq 2$, also see Section 5). To help with the understanding, we here take a closer look at a family of AP methods, that is closely related to our proposed methods except using a different implicit-explicit strategy as in (3.2) [23]. Our study here show that with an insufficient approximation of the local equilibrium at the discrete level, formally high order AP methods can reduce to first order temporal accuracy in g (at least) in the diffusive regime with $\varepsilon \ll 1$, and this reduction may further affect the accuracy in $f = \rho + \varepsilon g$.

Since the root of the issue lies in the temporal discretization, particularly in the implicit-explicit strategy, we will start with a first order in time discretization based on an implicit-explicit strategy as in (3.2), and consider

$$\frac{\rho^{n+1} - \rho^n}{\Delta t} + \partial_x \langle vg^{n+1} \rangle + \omega \langle v^2 \rangle \partial_{xx} \rho^n = \omega \langle v^2 \rangle \partial_{xx} \rho^{n+1}, \tag{A.1a}$$

$$\frac{g^{n+1} - g^n}{\Delta t} + \frac{1}{\varepsilon} (\mathbf{I} - \Pi)(v\partial_x g^n) + \frac{1}{\varepsilon^2} v\partial_x \rho^n = -\frac{1}{\varepsilon^2} g^{n+1}. \tag{A.1b}$$

By combining this new implicit-explicit strategy with the second order ARS(2,2,2) method and the third order ARS(4,4,3) method, we will have the *formally* second and third order in time method, referred to as the IMEX2-LM scheme and the IMEX3-LM scheme, respectively.

A.1 Formal analysis in the limit of $\varepsilon \to 0$

Without loss of generality, we next will focus on the IMEX2-LM scheme in our analysis. We consider the diffusive regime with $\varepsilon \ll 1$, and assume $\omega = 1$ (see the property in (2.6)). Given the numerical solution ρ^n, g^n at t^n , we update ρ^{n+1}, g^{n+1} at t^{n+1} by the IMEX2-LM scheme as follows.

$$\rho^{n,(0)} = \rho^n, \ g^{n,(0)} = g^n, \tag{A.2a}$$

$$\rho^{n,(1)} = \rho^n - \gamma \Delta t \left(\langle v^2 \rangle \partial_{xx} \rho^{n,(0)} + \partial_x \langle v g^{n,(1)} \rangle - \langle v^2 \rangle \partial_{xx} \rho^{n,(1)} \right), \tag{A.2b}$$

$$g^{n,(1)} = g^n - \gamma \Delta t \left(\frac{1}{\varepsilon} (\mathbf{I} - \Pi)(v \partial_x g^{n,(0)}) + \frac{1}{\varepsilon^2} v \partial_x \rho^{n,(0)} + \frac{1}{\varepsilon^2} g^{n,(1)} \right), \tag{A.2c}$$

$$\rho^{n+1} = \rho^n - \Delta t \langle v^2 \rangle (\delta \partial_{xx} \rho^{n,(0)} + (1 - \delta) \partial_{xx} \rho^{n,(1)})$$
(A.2d)

$$-(1-\gamma)\Delta t \left(\partial_x \langle vg^{n,(1)} \rangle - \langle v^2 \rangle \partial_{xx} \rho^{n,(1)}\right) - \gamma \Delta t \left(\partial_x \langle vg^{n+1} \rangle - \langle v^2 \rangle \partial_{xx} \rho^{n+1}\right),$$

$$g^{n+1} = g^n - \delta \Delta t \left(\frac{1}{\varepsilon} (\mathbf{I} - \Pi) (v \partial_x g^{n,(0)}) + \frac{1}{\varepsilon^2} v \partial_x \rho^{n,(0)} \right)$$
(A.2e)

$$-(1-\delta)\Delta t \left(\frac{1}{\varepsilon}(\mathbf{I}-\Pi)(v\partial_x g^{n,(1)}) + \frac{1}{\varepsilon^2}v\partial_x \rho^{n,(1)}\right) - \frac{\Delta t}{\varepsilon^2}\left((1-\gamma)g^{n,(1)} + \gamma g^{n+1}\right).$$

As $\varepsilon \to 0$, we formally obtain

$$\rho^{n,(0)} = \rho^n, \quad \rho^{n,(1)} = \rho^n + \gamma \Delta t \langle v^2 \rangle \partial_{xx} \rho^{n,(1)}, \tag{A.3a}$$

$$\rho^{n+1} = \rho^n + \Delta t \langle v^2 \rangle \left((1 - \gamma) \partial_{xx} \rho^{n,(1)} + \gamma \partial_{xx} \rho^{n+1} \right), \tag{A.3b}$$

an implicit discretization of the limiting diffusive equation (2.4) to solve ρ , with its second order accuracy directly inherited from the IMEX-RK ARS(2,2,2) method. This implies the AP

property of the IMEX2-LM scheme. On the other hand, the variable g is approximated by

$$g^{n,(0)} = g^n, \quad g^{n,(1)} = -v\partial_x \rho^{n,(0)},$$
 (A.4a)

$$(1 - \gamma)g^{n,(1)} + \gamma g^{n+1} = -\delta v \partial_x \rho^{n,(0)} - (1 - \delta)v \partial_x \rho^{n,(1)}$$
(A.4b)

as $\varepsilon \to 0$, and this further gives

$$g^{n+1} = \frac{1 - \delta - \gamma}{\gamma} v \partial_x \rho^{n,(0)} - \frac{1 - \delta}{\gamma} v \partial_x \rho^{n,(1)}. \tag{A.5}$$

Next we will argue that the scheme for g in (A.4) is only of first order accuracy. By taking a spatial derivative over the IMEX2-LM scheme (A.2), it is not hard to see that in the limit of $\varepsilon \to 0$, $\partial_x \rho$ is approximated by the same second order scheme as (A.3). Hence to show g^{n+1} being first order accurate boils down showing $g^{n+1} + v\partial_x \rho^{n+1}$ being first order accurate. Based on the limiting scheme (A.4)-(A.5),

$$g^{n+1} + v\partial_x \rho^{n+1} = \frac{1 - \delta - \gamma}{\gamma} v\partial_x \rho^n - \frac{1 - \delta}{\gamma} (v\partial_x \rho^n + \gamma \Delta t \langle v^2 \rangle v \partial_{xxx} \rho^{n,(1)})$$

$$+ \left(v\partial_x \rho^n + \Delta t \langle v^2 \rangle v \left((1 - \gamma)\partial_{xxx} \rho^{n,(1)} + \gamma \partial_{xxx} \rho^{n+1} \right) \right)$$

$$= \Delta t \langle v^2 \rangle v \left((\delta - \gamma)\partial_{xxx} \rho^{n,(1)} + \gamma \partial_{xxx} \rho^{n+1} \right)$$

$$= \delta \Delta t \langle v^2 \rangle v \partial_{xxx} \rho^n + O(\Delta t^2).$$
(A.6)

Recall that in the limit of $\varepsilon \to 0$, the exact solution satisfies $g + v\partial_x \rho = 0$. This, combined with (A.6), indicates the local truncation error to preserve this local equilibrium is first order in Δt , so is that for g in the limit of $\varepsilon \to 0$. This reduced order of accuracy will be subsequently carried over to the IMEX2-LM scheme with $\varepsilon \ll 1$ in the diffusive regime (say, under some uniform boundedness assumptions for the continuous and discrete solutions as at the beginning of Section 5). With similar analysis, one can formally shown that the IMEX3-LM scheme is first order accurate when approximating g in the diffusive regime. Given that $f = \rho + \varepsilon g$, the accuracy reduction in g can further affect the accuracy for f.

A.2 Numerical study

We here will report some numerical tests to support and complement our formal analysis. For the IMEXp-LM scheme (p=2,3), we combine it with the LDG spatial discretization in Section 3.2 with the discrete space U_h^{p-1} , and the weight function is taken to be $\omega = \exp(-\varepsilon/h)$. The resulting method is referred to as the IMEXp-LDGp- \mathcal{M} -LM scheme, with the time step set as $\Delta t = \Delta t_{CFLp\mathcal{M}}$ as defined in (6.2e) and (6.2f) for p=2,3, respectively. The choice of the time steps by no means is optimal.

We consider the example in Section 6.1.1 from the telegraph equation. In Table A.10, we report the L^1 errors and orders for $j=\langle vg\rangle$ when $\varepsilon=10^{-6}$ on spatial meshes of $N=10,20,\cdots,320$ elements, and the first order accuracy in g is observed. As a comparison, our proposed methods with the same weight function approximate j with the designed p-th order accuracy (p=2,3), see Tables 6.3-6.4. Note that with this ε , the errors in εg are rather small, hence the order reduction in g does not affect the accuracy order of $f=\rho+\varepsilon g$ on the meshes we used. We further test the IMEXp-LDGp- \mathcal{M} -LM scheme (p=2,3) in relatively more kinetic regimes with $\varepsilon=10^{-2},0.5$, and the full p-th order accuracy is observed for j as designed. The results are omitted.

Finally we consider a more interesting case with $\varepsilon=10^{-3}$ when the problem is in a relatively intermediate regime. In Table A.11, the L^1 errors and orders of both ρ and j as well as the L^1_* errors and orders of f are reported for the IMEX3-LDG3- \mathcal{M} -LM and IMEX3-LDG3- \mathcal{M} schemes on spatial meshes of $N=10,20,\cdots,640$. Here $||\phi||_{L^1_*}:=\langle ||\phi||_{L^1(\Omega_x)}\rangle$. A few observations can be made.

• First of all, the accuracy for ρ is third order as designed for both schemes, with errors of two methods being comparable.

- Secondly, while the computed g by our proposed IMEX3-LDG3- \mathcal{M} scheme is of full third order accuracy, that by the IMEX3-LDG3- \mathcal{M} -LM scheme is only of first order accuracy on relatively coarser meshes with $N=10,\cdots,160$. When N=320,640, the problem is now in a more kinetic regime with respect to the discretization parameter Δt and h, and the convergence order for g by the IMEX3-LDG3- \mathcal{M} -LM scheme improves. One should note that with the time step taken according to (6.2f), we have used $\Delta t=0.982\times 10^{-2}$ for N=160, and $\Delta t=0.559\times 10^{-5}$ for N=320. The drastic change in the time step size may also contribute to the significant error drop when N=320,640. On all meshes we examined, the errors in g by the IMEX3-LDG3- \mathcal{M} -LM scheme are always larger.
- Finally if we examine the errors and orders in $f = \rho + \varepsilon g$, the order reduction is most pronounced when N = 80,160. Note that with a fixed ε , smaller N corresponds to a relatively more diffusive regime, and larger N corresponds to a relatively more kinetic regime.

Based on the tests above, one can see that the AP methods based on the implicit-explicit strategy as in (A.1) result in order reduction in g in relative diffusive regimes, and this reduction can further affect the accuracy in f. A mathematically more rigorous analysis would be needed to fully understand our observations.

Table A.10: L^1 errors and orders of $j = \langle vg \rangle$ for the example in Section 6.1.1 with $\varepsilon = 10^{-6}$: IMEXp-LDGp- \mathcal{M} -LM with p = 2, 3, and $\omega = \exp(-\varepsilon/h)$

ε	N	IMEX2-LDG2	2 - \mathcal{M} - LM	$IMEX3-LDG3-\mathcal{M}-LM$			
		L^1 error of j	order	L^1 error of j	order		
	10	1.303E-02	-	2.952E-02	-		
	20	6.652 E-03	0.97	1.518E-02	0.96		
10^{-6}	40	3.254 E-03	1.03	7.629E-03	0.99		
	80	1.642 E-03	0.99	3.658E-03	1.06		
	160	8.164E-04	1.01	1.826E-03	1.00		
	320	4.071E-04	1.00	9.029E-04	1.02		

Table A.11: L^1 errors of ρ , $j=\langle vg\rangle$ and L^1_* errors of f as well as the respective convergence orders, for the example in Section 6.1.1 with $\varepsilon=10^{-3}$: IMEX3-LDG3- \mathcal{M} -LM and IMEX3-LDG3- \mathcal{M} , and $\omega=\exp(-\varepsilon/h)$. Here $||\phi||_{L^1_*}:=\langle ||\phi||_{L^1(\Omega_x)}\rangle$.

	N	L^1 error of ρ	order	L^1 error of j	order	L^1_* error of f	order
	10	1.867E-04	-	1.515E-02	-	1.868E-04	-
	20	2.366E-05	2.98	7.642E-03	0.99	2.403E-05	2.96
	40	2.951E-06	3.00	3.658E-03	1.06	4.254E-06	2.50
IMEX3-LDG3- <i>M</i> -LM	80	3.694 E-07	3.00	1.825E-03	1.00	1.826E-06	1.22
	160	4.627E-08	3.00	9.022E-04	1.02	9.022 E-07	1.02
	320	5.720E-09	3.02	1.630E-07	12.4	5.720 E-09	7.30
	640	7.157E-10	3.00	1.390E-08	3.55	7.156E-10	3.00
	10	1.867E-04	-	2.233E-04	-	1.867E-04	-
	20	2.366E-05	2.98	2.749E-05	3.02	2.366E-05	2.98
	40	2.951E-06	3.00	3.452E-06	2.99	2.951E-06	3.00
IMEX3-LDG3- \mathcal{M}	80	3.691E-07	3.00	4.284E-07	3.01	3.691E-07	3.00
	160	4.611E-08	3.00	5.354E-08	3.00	4.611E-08	3.00
	320	5.720E-09	3.01	6.668E-09	3.01	5.720 E-09	3.01
	640	7.155E-10	3.00	8.338E-10	3.00	7.155E-10	3.00

Acknowledgement. The authors want to thank the reviewers for their valuable comments and specific suggestions to improve the presentation of the findings.

References

- [1] Marvin L Adams. Discontinuous finite element transport solutions in thick diffusive problems. *Nuclear Science and Engineering*, 137(3):298–333, 2001.
- [2] Marvin L Adams and Edward W Larsen. Fast iterative methods for discrete-ordinates particle transport calculations. *Progress in Nuclear Energy*, 40(1):3–159, 2002.
- [3] U.M. Ascher, S.J. Ruuth, and R.J. Spiteri. Implicit-explicit Runge-Kutta methods for timedependent partial differential equations. Applied Numerical Mathematics, 25(2):151–167, 1997.
- [4] Sebastiano Boscarino, Philippe G LeFloch, and Giovanni Russo. High-order asymptotic-preserving methods for fully nonlinear relaxation problems. *SIAM Journal on Scientific Computing*, 36(2):A377–A395, 2014.
- [5] Sebastiano Boscarino, Lorenzo Pareschi, and Giovanni Russo. Implicit-explicit Runge-Kutta schemes for hyperbolic systems and kinetic equations in the diffusion limit. SIAM Journal on Scientific Computing, 35(1):A22-A51, 2013.
- [6] Sebastiano Boscarino and Giovanni Russo. Flux-explicit IMEX Runge-Kutta schemes for hyperbolic to parabolic relaxation problems. SIAM Journal on Numerical Analysis, 51(1):163-190, 2013.
- [7] Russel E Caffisch, Shi Jin, and Giovanni Russo. Uniformly accurate schemes for hyperbolic systems with relaxation. SIAM Journal on Numerical Analysis, 34(1):246–281, 1997.
- [8] Paul Castillo, Bernardo Cockburn, Dominik Schötzau, and Christoph Schwab. Optimal a priori error estimates for the hp-version of the local discontinuous Galerkin method for convection-diffusion problems. *Mathematics of Computation*, 71(238):455–478, 2002.
- [9] Bernardo Cockburn and Chi-Wang Shu. TVB Runge-Kutta local projection discontinuous galerkin finite element method for conservation laws. ii. general framework. *Mathematics* of Computation, 52(186):411–435, 1989.
- [10] Bernardo Cockburn and Chi-Wang Shu. The local discontinuous Galerkin method for timedependent convection-diffusion systems. SIAM Journal on Numerical Analysis, 35(6):2440– 2463, 1998.
- [11] Pierre Degond. Asymptotic-preserving schemes for fluid models of plasmas. arXiv preprint arXiv:1104.1869, 2011.
- [12] Jean-Luc Guermond and Guido Kanschat. Asymptotic analysis of upwind discontinuous Galerkin approximation of the radiative transport equation in the diffusive limit. SIAM Journal on Numerical Analysis, 48(1):53–78, 2010.
- [13] Mark H Holmes. Introduction to Perturbation Methods (2nd Edition), volume 20. Springer Science & Business Media, 2012.
- [14] Juhi Jang, Fengyan Li, Jing-Mei Qiu, and Tao Xiong. Analysis of asymptotic preserving DG-IMEX schemes for linear kinetic transport equations in a diffusive scaling. SIAM Journal on Numerical Analysis, 52(4):2048–2072, 2014.
- [15] Juhi Jang, Fengyan Li, Jing-Mei Qiu, and Tao Xiong. High order asymptotic preserving DG-IMEX schemes for discrete-velocity kinetic equations in a diffusive scaling. *Journal of Computational Physics*, 281:199–224, 2015.
- [16] Shi Jin. Asymptotic preserving (AP) schemes for multiscale kinetic and hyperbolic equations: a review. Lecture Notes for Summer School on Methods and Models of Kinetic Theory, Porto Ercole (Grosseto, Italy), 2010.
- [17] Shi Jin, Lorenzo Pareschi, and Giuseppe Toscani. Uniformly accurate diffusive relaxation schemes for multiscale transport equations. SIAM Journal on Numerical Analysis, 38(3):913–936, 2000.

- [18] Guido Kanschat and J-C Ragusa. A robust multigrid preconditioner for S_n DG approximation of monochromatic, isotropic radiation transport problems. SIAM Journal on Scientific Computing, 36(5):A2326-A2345, 2014.
- [19] Axel Klar and Andreas Unterreiter. Uniform stability of a finite difference scheme for transport equations in diffusive regimes. SIAM Journal on Numerical Analysis, 40(3):891–913, 2002.
- [20] Edward W Larsen. On numerical solutions of transport problems in the diffusion limit. Nuclear Science and Engineering, 83(1):90–99, 1983.
- [21] Edward W. Larsen and Jim E. Morel. Asymptotic solutions of numerical transport problems in optically thick, diffusive regimes ii. *Journal of Computational Physics;(USA)*, 83(1), 1989.
- [22] Mohammed Lemou and Florian Méhats. Micro-macro schemes for kinetic equations including boundary layers. SIAM Journal on Scientific Computing, 34(6):B734–B760, 2012.
- [23] Mohammed Lemou and Luc Mieussens. A new asymptotic preserving scheme based on micro-macro formulation for linear kinetic equations in the diffusion limit. SIAM Journal on Scientific Computing, 31(1):334–368, 2008.
- [24] Jichun Li, Cengke Shi, and Chi-Wang Shu. Optimal non-dissipative discontinuous Galerkin methods for Maxwells equations in Drude metamaterials. *Computers & Mathematics with Applications*, 73(8):1760–1780, 2017.
- [25] Jian-Guo Liu and Luc Mieussens. Analysis of an asymptotic preserving scheme for linear kinetic equations in the diffusion limit. SIAM Journal on Numerical Analysis, 48(4):1474–1491, 2010.
- [26] Tai-Ping Liu and Shih-Hsien Yu. Boltzmann equation: micro-macro decompositions and positivity of shock profiles. Communications in Mathematical Physics, 246(1):133–179, 2004.
- [27] F. Malvagi and G.C. Pomraning. Initial and boundary conditions for diffusive linear transport problems. *Journal of Mathematical Physics*, 32(3):805–820, 1991.
- [28] William H. Reed and T.R. Hill. Triangular mesh methods for the neutron transport equation. Technical report, Los Alamos Scientific Lab., 1973.